Fracture of Nanoporous Gold

by

Nilesh Badwe

A Dissertation Presented in Partial Fulfillment
of the Requirements for the Degree
Doctor of Philosophy

Approved November 2014 by the
Graduate Supervisory Committee:

Karl Sieradzki, Chair
Pedro Peralta
Ravi Mahajan
Jay Oswald

ARIZONA STATE UNIVERSITY

December 2014

ABSTRACT

This research examines several critical aspects of the so-called “film induced cleavage” model of stress corrosion cracking using silver-gold alloys as the parent-phase material. The model hypothesizes that the corrosion generates a brittle nanoporous film, which subsequently fractures forming a high-speed crack that is injected into the uncorroded parent-phase alloy. This high speed crack owing to its kinetic energy can penetrate beyond the corroded layer into the parent phase and thus effectively reducing strength of the parent phase. Silver-gold alloys provide an ideal system to study this effect, as hydrogen effect can be ruled out on thermodynamic basis. During corrosion of the silver-gold alloy, the less noble metal i.e. silver is removed from the system leaving behind a nanoporous gold (NPG) layer. In the case of polycrystalline material, this corrosion process proceeds deeper along the grain boundary than the matrix grain. All of the cracks with apparent penetration beyond the corroded (dealloyed) layer are intergranular. Our aim was to study the crack penetration depth along the grain boundary to ascertain whether the penetration occurs past the grain-boundary dealloyed depth. EDS and imaging in high-resolution aberration corrected scanning transmission electron microscope (STEM) and atom probe tomography (APT) have been used to evaluate the grain boundary corrosion depth.

The mechanical properties of monolithic NPG are also studied. The motivation behind this is two-fold. The crack injection depth depends on the speed of the crack formed in the nanoporous layer, which in turn depends on the mechanical properties of the NPG. Also NPG has potential applications in actuation, sensing and catalysis. The measured value of the Young’s modulus of NPG with 40 nm ligament size and 28% density was ~ 2.5 GPa and the Poisson’s ratio was ~ 0.20. The fracture stress was observed to be ~ 11-13 MPa. There was no significant change observed between these mechanical properties on oxidation of NPG at 1.4 V. The fracture toughness value for the NPG was ~ 10 J/m^2. Also dynamic fracture tests showed that the NPG is capable of supporting crack velocities ~ 100 – 180 m/s.

ACKNOWLEDGMENTS

I would like to thank Prof. Karl Sieradzki for his continuous guidance in my whole research without which this research wouldn't have been possible. I would also like to thank my committee members Prof. Pedra Peralta, Prof. Jay Oswald, and Dr. Ravi Mahajan. I am greatly indebted to Dr. Shaofeng Sun and Dr. Fritz Friedersdorf whose prior work provided base for my entire research. I would also like to thank Xiying Chen for preparing all the nanoporous gold samples for my mechanical tests. I also appreciate support of all my previous and current lab mates for keeping the lab environment enjoyable and stress-free. I am grateful to Dr. Daniel Schreiber for help with preparing the TEM samples, APT samples and analysis of the APT samples at the Pacific Northwest National Lab (PNNL) facilities. I gratefully acknowledge the use of facilities within the Center for Solid State Science at Arizona State University. I must mention the help provided by Dr. Toshihiro Aoki, Dr. John Mardinley, Dr. Jiangtao Zhu and Prof. Peter Crozier for their help with the high resolution TEM work and analysis.

I am grateful to the financial support from Department of Energy (DOE) to carry out this research. I would also like to thank Intel Corporation to provide me an opportunity to conduct my adhesion research at the mechanical core comp labs during my internships.

Finally I would like to thank my wife - Priyanka, my parents, in-laws, and dear friend Sudhanshu Singh for continuous moral support during the whole journey of my graduate studies.

TABLE OF CONTENTS

Page

LIST OF TABLES

LIST OF FIGURES

Figure Page

Figure Page

Figure Page

Figure Page

Figure Page

CHAPTER 1

INTRODUCTION

In recent years, nanoporous materials have attracted attention of researchers due to their very high surface to volume ratio, chemical stability, biocompatibility, and high conductivity. Combining that with special chemical properties of gold (Au), nanoporous gold (NPG) has wide application range. One of the most widely explored area of NPG application is catalysis. The NPG have extremely high surface area to mass ratio. Biener et al. [1] measured surface area for NPG as high as ~ 10 – 15 m^2/g. Several researchers [2, 3, 4, 5, 6] have shown that the NPG can be used as a catalyst for carbon monoxide oxidation. Zeis et al. [7] used NPG for reduction of oxygen and hydrogen peroxide. McCurry et al. [8] demonstrated catalytic use of platinized NPG thin films for formic acid oxidation. Wittsock et al. [9] claimed that in the catalytic applications of the NPG, it is actually the residual silver (Ag) that regulates the availability of the reactive oxygen. Biener et al. [1] showed that NPG can also be used as a mechanical actuator by converting chemical energy to mechanical energy. They were able to achieve reversible strain of the order of few tenths of a percent by alternatingly exposing NPG to ozone and carbon monoxide. They attributed this behavior to the changes in the surface stress with different adsorbate species. Weissmuller and co-workers [10, 11] showed that a similar effect can be achieved by electrochemical methods. They were able to achieve strains of ~ 1.3% on nanoporous Au-Pt alloy. They also showed that even flow stress of NPG can be modified by simply changing applied voltage [11] in electrolyte. Hu et al. [12] used the NPG for a biosensing application. They showed that a DNA sensor based on NPG and multifunctional encoded Au nanoparticles has detection limit as low as 28 aM (28×10^{-18} M) and exhibit selectivity even for a single-mismatched DNA detection.

According to recent news in the New York Times [13], current nuclear reactors in Pennsylvania, Virginia and South Carolina are planning to ask permission to extend the life of the reactors from 40 year to 80 year. This makes maintenance of these reactors particularly an important issue. These nuclear reactors and fossil fuel reactors use austenitic stainless steel and

nickel based alloys. Most of the failures observed in these alloys occur due to dealloying induced stress corrosion cracking (SCC). One of the possible mechanism for this type of SCC is film induced cleavage and AgAu, CuAu alloys are ideal system to study this mechanism. These alloys on dealloying produce a layer of NPG on the surface which on loading is claimed to be injecting cracks in the parent phase alloy. All these applications make the study of mechanical properties and fracture of NPG extremely important.

1.1 Synthesis of NPG:

A most common way to produce NPG is through dealloying. Dealloying is the process to chemically or electrochemically dissolve less noble metal from an alloy of two or more metals. This process generally leaves behind the more noble metal in the form of a porous structure [14].

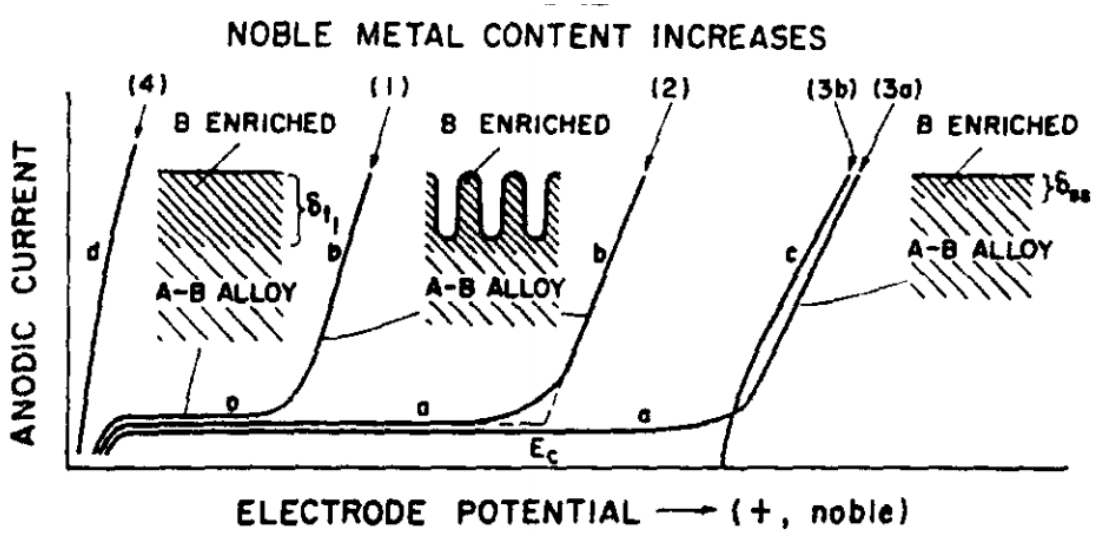

Figure 1: Polarization curve of binary alloy A-B where A is the more reactive metal, shows that as the content of the nobler metal B increases, the polarization curve shifts towards right on the current – voltage graph. [15]

Pickering [15] studied polarization behavior of A_pB_{1-p} type binary alloy systems. Figure 1 shows the polarization curves for A-B system (metal A – more reactive) with different compositions. The region “d” corresponds to potential dependent dissolution of an alloy with a very high value of p (i.e. A > 97%). The polarization curve for such system – curve (4) – is somewhat positive ($\lesssim$ 100 mV) than that for pure metal A. As the content of B increases, the curve shifts towards right and we start observing behavior more like the curves (1) and (2). The

region “a” corresponds to a very small current value (10^{-4} – 10^{-2} mA/cm^2), where a protective layer of B rich alloy is formed on the surface of the sample which limits the dissolution of A. The passivation is controlled by surface and volume diffusion rate of B. Once a specific potential called critical potential (E_c) is crossed, the dissolution rate of A increases to a point where the passivation cannot occur. This starts pitting on the sample surface, leading to porosity formation. The curve 3(b) represents dissolution of metal B. Both the metals are getting dissolved in the region (c) and the degree of selective dissolution goes down.

Later, Sieradzki and co-workers studied the concept of critical potential and percolation threshold in more detail for AgAu alloy system. Sieradzki and Newman [16] showed that for a binary alloy A_pB_{1-p} system, a continuous structure for both the metals is necessary for complete dealloying to occur. Earlier it was shown by Scher and Zallen [17] that for FCC metals, the percolation threshold is ~20%. In other words, when at least 20% of element A is present, all A atoms have at least 2 near neighbor A atoms. Sieradzki and co-workers [18, 19, 20] also studied the concept of E_C described by Pickering for AgAu and CuAu systems. They claimed that the process of electrochemical dissolution of element A from A_pB_{1-p} is accompanied by capillary driven surface diffusion of B atoms which passivates the surface. For potentials > E_C, the rate of A atom dissolution increases beyond a point that the B atoms cannot passivate the surface and a sudden rise in the current is observed.

Formation of the NPG is carried out through dealloying using mainly two different starting alloy materials: 1. AgAu 2. CuAu. Ag and Au form a complete solid solution, whereas in the case of CuAu, it forms intermetallic compounds at different compositions (Figure 2 and Figure 3). Figure 4 shows typical NPG morphology obtained through dealloying of AgAu alloy.

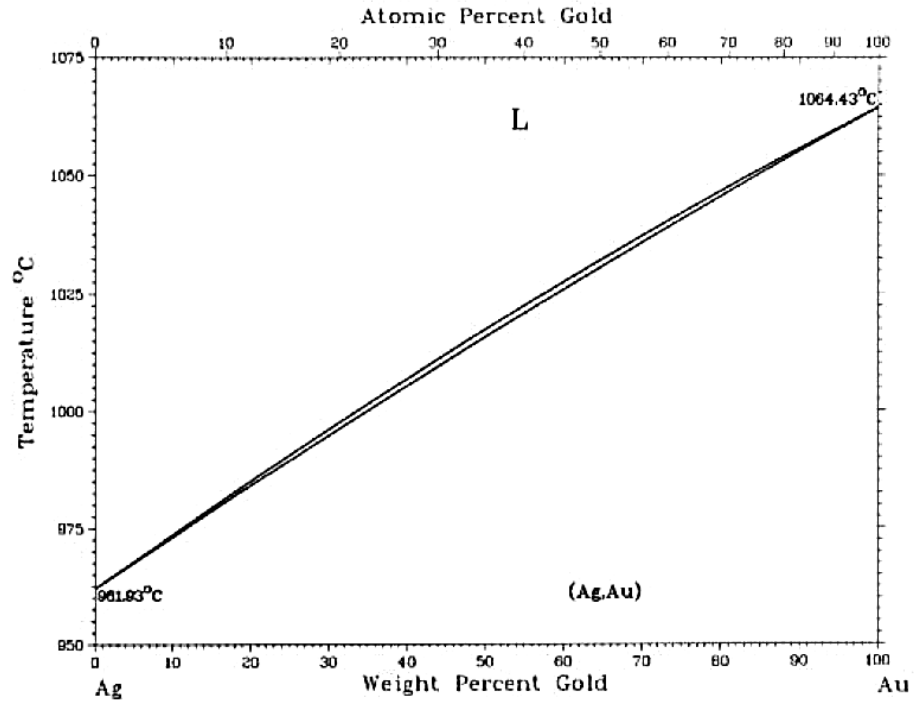

Figure 2: Phase diagram for silver - gold system above 900°C [21].

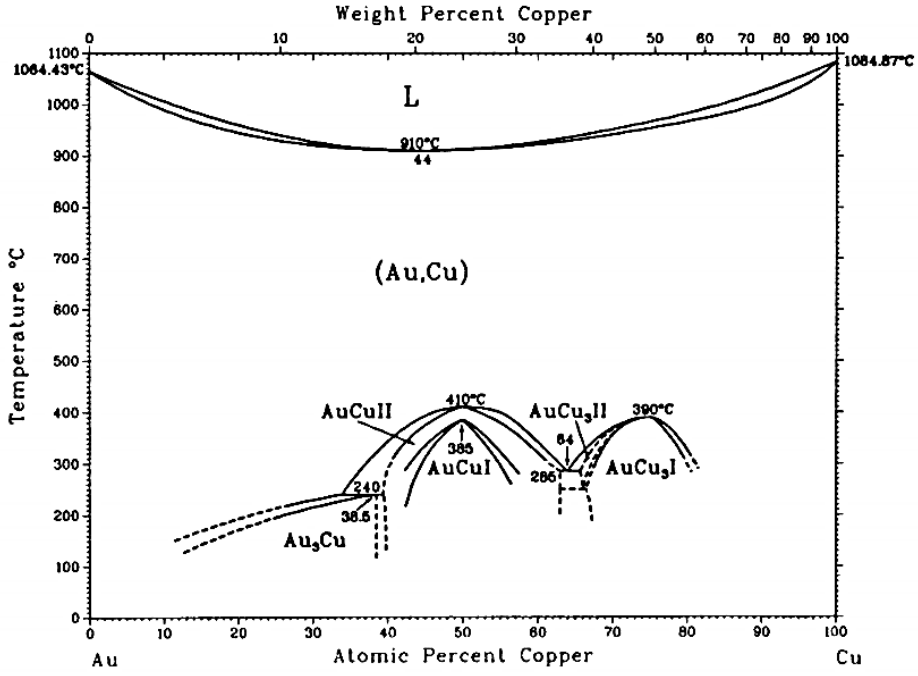

Figure 3: The copper – gold phase diagram shows different intermetallic compounds that form between Cu and Au at different compositions [21].

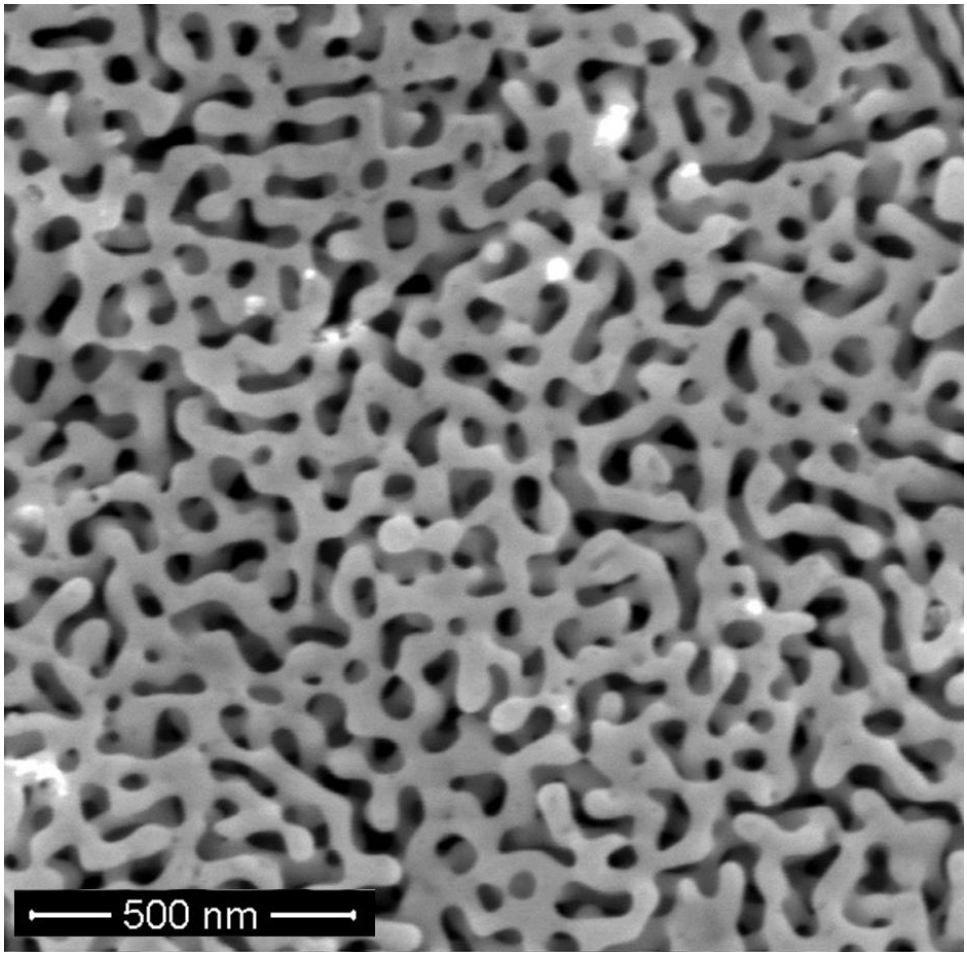

Figure 4: NPG sample fully dealloyed at ~ 1.17 V vs SHE in 1 M HNO_3 has ~ 30 – 60 nm ligament size. This dealloying voltage corresponds to a current density of ~ 1 mA/cm2 for $Ag_{72}Au_{28}$ alloy. This slow rate of dealloying helps prevent grain boundary cracking during the dealloying process.

Erlebacher et al. [14] used kinetic Monte Carlo simulations to study the evolution of porosity in the Ag-Au system which involved diffusion of Ag and Au atoms along with silver dissolution. They proposed that spinodal decomposition drives the Au atoms to form a two-dimensional structure at the solid – electrolyte interface. Most of the NPG formation has been carried out by dealloying AgAu in nitric acid (HNO_3). Hodge et al. [22] prepared NPG samples for mechanical testing using nanoindentor through free corrosion of AgAu alloy in concentrated HNO_3. In another study, Hodge et al. [23] used two step process which involved a potentiostatic corrosion in 1 M HNO_3 + 10^{-3} M Ag^+ solution followed by free corrosion in concentrated HNO_3. They used heat treatment on the samples to obtain grain coarsening to study yielding of the NPG using nanoindentation. Snyder et al. [24] also showed that NPG can be formed by dealloying

AgAu alloy in a neutral electrolyte $AgNO_3$. Later Sun and Balk [25] proposed a multi-step dealloying method where they used different voltages and different concentrations of HNO_3 to dealloy the AgAu alloy to form NPG. They claimed to form NPG with no volume change and little cracking. Some researchers have also used perchloric acid ($HClO_4$). Jin et al. [26] dealloyed AgAu alloy potentiostatically in 1 M $HClO_4$ at 330K to obtain NPG with ligament size of ~ 55 nm. They observed that ligament size obtained for NPG reduced to 15 nm under identical conditions with larger electrolyte volume. Recently Zhong et al. [27] were able to obtain NPG with ligament size of 11 nm on potentiostatic dealloying of CuAu alloy in 1 M $HClO_4$. Snyder et al. [28] found that on addition of ~ 6 atomic % of Pt to AgAu alloy, the NPG structure formed on dealloying exhibits much finer pore size (~ 5 nm) compared to the NPG formed from dealloying of AgAu alloys. They claimed that the Pt which has much lower diffusion rates than Au atoms, occupies the kink and step – edge sites and inhibits the Au surface diffusion and hence the coarsening of the ligaments.

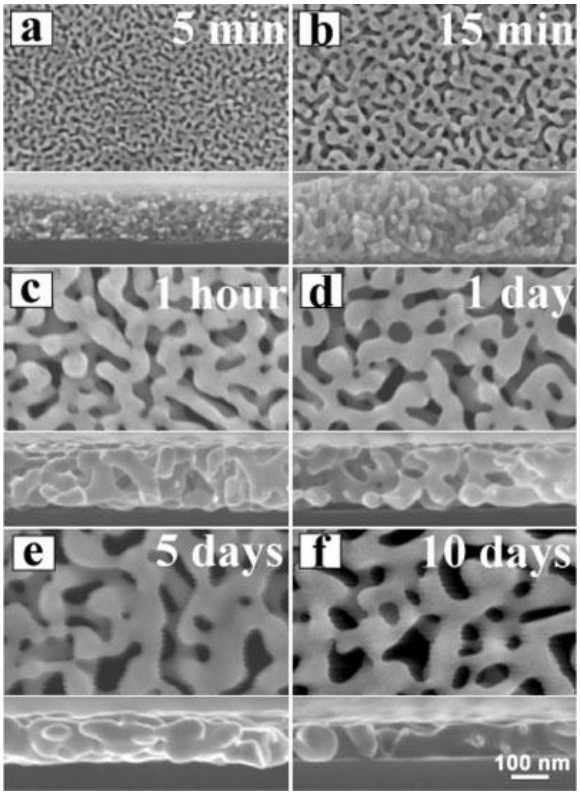

Figure 5: Coarsening of the ligaments was observed by Ding et al. [29] when the NPG was left inside HNO_3.

Ding et al. [29] studied NPG morphology on dealloying 100 nm thick Au leaf containing 37 – 50 % Au in concentrated HNO_3. The dealloying process finished within 5 minutes and they obtained a ligament size of ~ 6 nm. However, they observed that if the NPG is kept inside the concentrated HNO_3 for extended amount of time, the ligaments coarsen as seen in the Figure 5. However, they observed that the porous structure remains stable for at least 6 months if removed from the electrolyte and immersed in water. These structures were also reported to be stable if air – dried and left outside the electrolyte. Later Qian and Chen [30] showed that, if the NPG formed through the similar technique is left in concentrated HNO_3 for extended amount of time at low temperatures (-20^{o}C – below which the solution freezes), the surface diffusion of Au atoms is inhibited. They observed that the pore size was < 10 nm after 4 days for –20^{o}C sample whereas it was ~ 35 nm for a sample at room temperature.

1.2 Stress Corrosion Cracking:

Stress corrosion cracking (SCC) is the process of brittle like fracture of a ductile material under the influence of a tensile load and a chemical environment. Some of the different models proposed for the SCC are hydrogen (H) embrittlement, adsorption induced fracture, slip dissolution, and film induced cleavage.

There are different models of the hydrogen embrittlement. The hydrogen enhanced decohesion (HEDE) or hydrogen assisted cracking (HAC) as proposed by Oriani [31] assumes that the hydrogen atoms are adsorbed on the crack tip surface and diffuse to certain microstructural sites. Once the concentration of the hydrogen atoms reaches certain threshold value, their interaction with the charge density can lower the atomic bond strength between metal atoms. This lowers the cohesion strength of the metal leading to fracture. Beachem [32] first introduced the concept of hydrogen enhanced localized plasticity (HELP). He proposed that H atoms that diffuse inside the material through the crack tip can reduce local stress required for dislocation motion. This will result into local softening of the material. Another model for the H embrittlement is the hydrogen related phase change such as hydride formation. The crack propagation occurs by repetition of the process of metal hydride formation at the region near the crack tip and brittle cracking of the hydride film [33]. The hydrogen adsorption theory proposed by

Petch and Stables [34] is based on reduction in the surface free energy of crack by adsorption of H atoms. This surface free energy change is sufficient to cause cracking at lower stress value based on the Griffith criterion [35]. Uhlig [36] extended this concept and proposed a model for adsorption induced brittle or ductile fracture. This model explains the brittle failure of metals due to reduction in the metallic bond strength at the crack tip on adsorption of aggressive species at the crack tip. Lynch [37] proposed that the aggressive species adsorption at the crack tip weakens the bonding and eases the localized slip process in case of liquid metal embrittlement (LME), causing the fracture by ductile failure similar to the HELP mechanism.

A surface mobility model was presented by Galvele [38, 39, 40] to universally explain the SCC mechanisms like H embrittlement, liquid and solid metal embrittlement, and brittle SCC. This model assumes that, under an action of the reactive environment, the surface mobility of the atoms at the crack tip increases. These atoms diffuse away from the highly stressed crack tip to the stress-free crack walls and the crack growth occurs with in-flow of the vacancies in the opposite direction i.e. from the crack walls to the crack tip. He used Nabarro [41] and Herring [42] creep theory, which gives vacancy concentration for a stress surface (C) as

$$C = C^0 exp\left(\frac{\sigma a^3}{kT}\right) \quad 1$$

Here C^0 = equilibrium vacancy concentration for an unstressed surface, σ = normal elastic surface stress at the crack tip, a = size of an atom, k = Boltzmann's constant, and T = absolute temperature. Using this, he derived an expression of the crack velocity (V_p):

$$V_p = \frac{D_s}{L}\left[exp\left(\frac{\sigma a^3}{kT}\right) - 1\right] \quad 2$$

where D_s = the surface self-diffusion coefficient, L = the diffusion distance of the vacancies. However, Sieradzki and Friedersdorf [43] pointed out some major flaws in the argument. The surface of the crack tip is a free surface and unable to carry any stresses normal to the surface. Also they showed that Galvele failed to account for the capillary forces. The energetics of movement of an atom from a highly curved surface (crack tip) to a flat surface (crack walls) need to be considered. Another source of error pointed out was use of concentration gradients rather

than chemical potentials which includes the curvature and stress effect, to obtain the diffusion equations. Sieradzki and Friedersdorf assumed a hemi-cylindrical crack tip profile and used chemical potentials to derive the equilibrium vacancy concentration on the crack as:

$$kTln\left(\frac{C}{C^0}\right) = \Delta\mu = -\frac{\sigma_{yy}^2}{2E}a^3 + \gamma\kappa a^3 \quad (3)$$

Here $\Delta\mu$ = vacancy chemical potential difference in the stressed and unstressed surface, σ_{yy} = resolved stress at the surface, γ = interfacial free energy, κ = crack tip curvature, and E = Young's modulus. Using this analysis, they derived the crack velocity as

$$V = \frac{D_s N_s a^6}{kT}\frac{2}{\pi}\frac{1}{\rho^2}\left(\frac{\sigma_{yy}^2}{2E} - \gamma\kappa\right) \quad (4)$$

where N_s = number of lattice sites per unit area.

The crack velocities obtained for ductile noble metals using this equation was 14 orders of magnitude less than that obtained using Equation 2. Hence Sieradzki and Friedersdorf concluded that the ideas by Galvele may be applicable to SCC in relatively brittle materials where the σ_{yy} can take high value (~$E/20$), but cannot be applied to ductile metals.

The slip dissolution model [44] is based on localized dissolution of an alloy. It assumes that a protective film is formed at the crack tip in the presence of a reactive environment. The stress provides a localized plastic strain which breaks the film, exposing fresh metal to the reactive environment. This freshly exposed metal again undergoes localized anodic dissolution forming another layer of the protective film. Once this film reaches certain thickness, the stress again breaks the film continuing the process and effectively the crack propagation. The maximum crack velocity through this mechanism can be obtained from Equation 5 [45].

$$i_{ct} = \frac{vn\rho F}{m\beta} \quad (5)$$

Here i_{ct} = the current density corresponding to the crack tip dissolution rate, v = crack velocity, n = number of electrons transferred, ρ = density of the dissolving material, F = Faraday's constant, m = mean atomic weight, and β = atomic fraction of the dissolving material. However, this model cannot explain the interlocking fracture surfaces, cleavage-like morphology, and crack arrest markings which can be explained by the film induced cleavage model.

The film induced cracking model, as proposed by Sieradzki and Newman [46, 16], does not require the continuous dissolution of the material as in case of the film rupture or slip dissolution model. They developed the concept based on some of the early work by Edeleanu and Forty [47] on α–brass. They described the failure process in the α–brass as a two-step process: a local embrittlement i.e. brittle layer formation through dezincification followed by a cleavage – like fracture. This model proposed by Sieradzki and Newman [46] suggests that the reactive environment produces a film on the surface of the material with different mechanical properties from the parent phase which could be a compound like halide, oxide, nitride etc. or a nanoporous layer. The brittle cracks produced in this film are capable of dynamically penetrating the un-attacked ductile bulk material. They propose that the crack generated in this brittle layer can travel at very high velocity (of the order of 100 m/s). When such a crack hit the interface of the brittle film and the ductile parent phase, it penetrates into the parent phase. This crack can get arrested on encountering a defect (grain boundary, second phase material) in the parent phase material, crack branching, or exhaustion due to dislocation emission during crack advance. Sieradzki and Newman derive a mathematical formulation for this model where the crack loses its energy due to dislocation emission. Kinetic energy of the moving crack U_k is given by Mott [48],

$$U_k = \left(\frac{\kappa\rho\sigma_G^2}{2E}\right) l^2 v_c^2 \qquad 6$$

Here ρ = density of the bulk material, l = crack length, v_c = crack velocity, σ_G = Stress value corresponding to the Griffith failure, and E = Young's modulus. κ is an unknown constant which determines the terminal crack velocity. Sieradzki and Newman assumed this terminal crack velocity to be Rayleigh wave velocity v_R. This gives relation between κ and v_R as

$$v_R = \left(\frac{2\pi E}{\kappa\rho}\right)^{1/2} \qquad 7$$

As the crack starts propagating into the ductile bulk material, it emits dislocations. With every dislocation emitted, the crack loses some of its kinetic energy equal to the energy of a moving dislocation ΔU given by Nabarro [49] as,

$$\Delta U = \frac{Eb^2}{8\pi(1+v)}\frac{1}{\beta_2} ln\left(\frac{r}{r_0}\right) \quad 8$$

where

$$\beta_2 = \left(1 - \frac{v_d^2}{v_R^2}\right)^{1/2} \quad 9$$

Here v_d = dislocation velocity, v = Poisson's ratio, r_0 = dislocation core radius, and r = radius of elastic cylinder containing the dislocation (here assumed to be of the order of the grain size). Sieradzki and Newman assumed that a single dislocation is emitted per characteristic crack advance distance of the order of a burger's vector (~ b). However, let us assume that n dislocations are emitted per burger's vector advance of the crack tip. Combining Equation 8 and 9 and assuming total energy conservation i.e. $\delta U_{total} = 0$, gives us an equation for change in crack velocity δv per characteristic crack advance δl as:

$$\delta v = n\frac{v_R^2}{v_c}\frac{E^2 b^2}{32\pi l k_G^2}\frac{1}{\beta_2(1+v)} ln\left(\frac{r}{r_0}\right) - \frac{v_c}{l}\delta l \quad 10$$

where

$$k_G = \sigma_G\sqrt{\pi l} = \sqrt{2E\Gamma} \quad 11$$

Here Γ is the surface energy. This argument is mainly applicable to a transgranular film induced cracking as the physical properties like Young's modulus, Poisson's ratio, density etc. cannot be determined for an grain boundary due to physical constraints. Sieradzki and Newman [46] observed that the cracking event in α–brass characterized by an acoustic transducer was simultaneous with sudden jump in the current while maintaining a constant voltage. The sudden jump in the current is indicative of a fresh surface being exposed to the electrolyte.

Although most of the initial work related to the film induced cleavage was performed on α–brass, most of the researchers later used Cu-Au and Ag-Au alloys to study this mechanism. Major advantage with these systems is the control of dealloyed layer thickness through electrochemical dealloying, absence of any side reaction, and stability of the dealloyed layer out of the electrolyte. Hydrogen embrittlement effect can be ignored in the AgAu and the CuAu alloys on the basis of thermodynamic calculations by Bertocci [50].

Cassagne et al. [51, 52] used $Cu_{75}Au_{25}$ single crystal samples to study the film induced cleavage. They immersed their samples in aqueous 2% ferric chloride solution for 10 and 30 days. The samples were then cleaned with water, ethanol, dried and loaded in three point bending. The samples were mounted in epoxy and mechanically cross-sectioned. These samples showed number of cracks formed in the porous layer. Most of these cracks stopped at the interface of the porous layer and the bulk material whereas some of the cracks (as shown in the Figure 6) extended well beyond the porous layer and penetrated in to the parent phase. However, it was not conclusively determined whether these cracks occurred as a single cleavage event in air or multiple events in the corrosive solution.

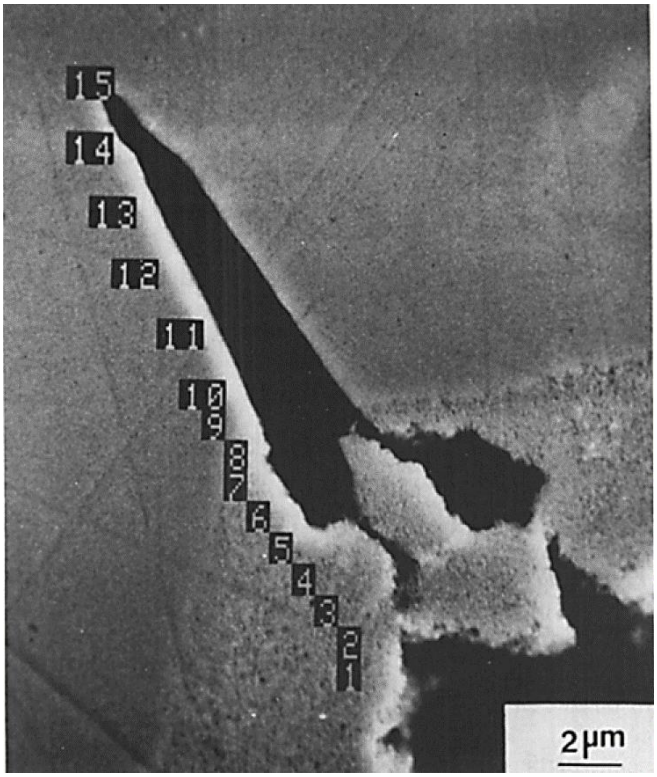

Figure 6: A deep transgranular crack observed by Cassagne et al. [51] in three-point bending of partially dealloyed Cu_3Au samples. The numbers indicate the points where EDS was performed in the SEM. The EDS analysis showed dealloying only for points 1 – 9. The composition obtained for points 10 – 15 was same as the bulk composition.

Newman and co-workers [53, 54] tried to decouple the corrosion and fracture processes by immersing α–brass and Ag-Au alloy samples in liquid nitrogen (LN_2) to inhibit the corrosion before fracture of the sample. It is well know that the FCC metals are ductile at liquid nitrogen

temperature [55]. They concluded that simple room temperature rinsing and air drying can cause coarsening of the porous layer making it ductile and unable to cause brittle fracture. All of these tests were rapid straining of the samples till failure. The failure observed in case of α–brass was mainly transgranular, whereas; the AgAu alloys showed intergranular cracking. However, in case of AgAu polycrystalline samples, they used 50 – 100 um thick foils and put a 20 um thick dealloyed layer. Friedersdorf [56] showed that the GB dealloying is at least 3 – 5 times that of the bulk dealloying for some GBs. This indicates that there is good possibility that the GBs were completely dealloyed through thickness. Saito et al. [57] measured double layer capacitance to verify the coarsening of the porous layer and demonstrated that a coarsened NPG is incapable of injecting intergranular cracks. They observed that presence of chloride ion accelerates the coarsening rate of the NPG, whereas, the pyridine ion suppresses the coarsening. Li and Sieradzki [58] studied the ductile – brittle transition in the NPG as a function of ligament size in the NPG with 24% Au content. They argued that the coarsening of the ligaments in the NPG increases probability of dislocation presence in the ligaments which in turn makes the sample fail in ductile manner. Chen and co-workers [59, 60] studied the brittle fracture induced by a dealloyed layer in CuAu alloys. They showed that such a layer is capable of producing both intergranular and transgranular brittle fracture, and the mode of fracture is controlled by the magnitude of the applied stress. Friedersdorf and Sieradzki [61] studied the crack penetration depth as a function of dealloyed layer thickness and dealloying potential. They observed that keeping the thickness constant, the crack penetration depth decreases as the dealloying potential increases. This can be attributed to the possible grain boundary cracking during dealloying at high potentials due to volume change [62]. If the grain boundary stays intact inside the dealloyed region, the crack can achieve high velocity as it reaches the interface between the dealloyed layer and the un-dealloyed parent phase. Barnes et al. [63] used bamboo structured wires and performed localized dealloying to promote transgranular fracture in $Ag_{80}Au_{20}$ alloys. They observed crack injection at extremely low stress levels while the applied voltage was dropped down to stop any Faradaic reaction. They also showed that intergranular fracture is possible even

after coarsening the ligaments in the samples in deionized water for 5 minutes after dealloying of $Ag_{77.3}Au_{22.7}$.

To understand the crack injection process, it is necessary to understand the velocities of the cracks that are generated in these porous layers formed on top of the metallic samples. The crack velocity in an isotropic solid depends on its Young's modulus, Poisson's ratio and density. Hence it is important to measure mechanical properties of the NPG.

1.3 Mechanical Properties of NPG:

Gibson and Ashby [64] have performed detailed theoretical analysis of porous material with length scales of the order of micrometers. They derived equations for the Young's modulus (Equation 12) and the yield stress (Equation 13) of the porous material as a function of the modulus and yield stress of the bulk solid $(E_s \,\&\, \sigma_s)$ and the relative density of the porous material $\left(\frac{\rho^*}{\rho_s}\right)$.

$$E = E_s \left(\frac{\rho^*}{\rho_s}\right)^2 \qquad 12$$

$$\sigma = 0.3\, \sigma_s \left(\frac{\rho^*}{\rho_s}\right)^{1.5} \qquad 13$$

Hodge et al. [23] suggested a modification to the yield stress equation after studying several different ligament size NPG samples in nanoindentor. They claimed that as Au ligament size decreases, yield stress of the individual ligament increases and suggested that the σ_s term should be replaced by a Hall - Petch type relation: $\sigma_s = \sigma_s + k_{Au} L^{-1/2}$.

Many other researchers have also studied different mechanical properties of the NPG using different techniques. Table 1 compiles most of these results. Some of the significant results are discussed later.

Table 1: Mechanical properties of NPG reported in the literature

Reference	Starting material	Measurement Technique	L (nm)	E (GPa)	ν	σ_y (MPa)	σ_f (MPa)
[65]	$Ag_{58}Au_{42}$ 0.5 mm thick disk	Nanoindentation	100	11.1	-	145	-
[66]	$Ag_{70}Au_{30}$ 1 mm X 400 um X 50-500 um dog-bone	Tensile and compression test	20-35	3.0	0.16	11	11
[67]	$Ag_{65}Au_{35}$ 1.5 mm X 260-500 um X 450-700 um	Tensile test	105	4.1 – 7.3 (ave 4.5)	0.225	5.2 - 12.1 (ave 7.9)	5.2 - 12.1 (ave 7.9)
[67]	$Ag_{67}Au_{33}$ single crystal 1.9 mm X 475 um X 220 um dog-bone	Tensile test	35-60	3.8 – 5.4 (ave 4.5)	0.22	21.2 – 28.4 (ave 25.2)	21.2 – 28.4 (ave 25.2)
[68]	$Ag_{65}Au_{35}$ 100 nm leaf	Thin film buckling	3	32 – 48	-	-	-
[68]	$Ag_{65}Au_{35}$ 100 nm leaf	Thin film buckling	6	23 – 29	-	-	-
[68]	$Ag_{65}Au_{35}$ 100 nm leaf	Thin film buckling	12	8 – 18	-	-	-
[68]	$Ag_{65}Au_{35}$ 100 nm leaf	Thin film buckling	20	7 – 12	-	-	-
[68]	$Ag_{65}Au_{35}$ 100 nm leaf	Thin film buckling	40	5 – 7.5	-	-	-
[69]	$Ag_{75}Au_{25}$ 21 nm X 21 nm X 107 nm	MD simulations	1.8	3.7	0.33	25-175	-
[70]	$Ag_{72}Au_{28}$ Au leaf 1 mm X 200 um X 20 um	Tensile test	10	12.5	-	60	90
[71]	$Ag_{63}Au_{37}$ Au leaf dog-bone 7 um X 300 nm X 100 nm	Deflective tensile test using nanoindentor	20-40	9	-	110	-
[62]	$Ag_{75}Au_{25}$ 1-8 um dia. pillars	Micro-pillar compression	15	7	-	-	-
[72]	$Ag_{75}Au_{25}$ cylinders 1.2 mm dia. 2 mm length	Compression	40	0.3	-	-	-
[73]	$Ag_{64\text{-}76}Au_{36\text{-}24}$	MD simulations	2.5 – 4	2.8 – 4.8	-	130-230	155-265
[74]	$Ag_{65\text{-}75}Au_{35\text{-}25}$	Laser ultrasonic wave speed measurement	30-50	2.57 – 2.88	0.20 – 0.24	-	-

Symbols used in the table: L = Ligament size, E = Young's modulus, ν = Poisson's ratio, σ_y = Yield stress, σ_f = Fracture stress

As we can see from the Table 1 many researchers have used nanoindentation, pillar compression, and other indirect methods to study the mechanical properties of the NPG. A very few studies have used direct tensile testing of the NPG to obtain the mechanical properties of NPG. Some of the most significant results of mechanical properties of the NPG were published by Balk and co-workers [67, 66]. They used millimeter-scale dog-bone single and polycrystalline samples to study the mechanical properties of the NPG. They performed tensile and compressive tests of the NPG samples and measured strain using digital image correlation (DIC). They obtained Young's modulus and Poisson's ratio values of 3 – 4.5 GPa and 0.16 – 0.24, respectively, for 30 – 35 % dense NPG. The measured values of the yield stress were 10 – 25 MPa. Another tensile test result published by Xia et al. [70], where they used Au leaf as starting material to produce NPG with length scale of 10 nm, obtained a Young's modulus value of 12.5 GPa. They tracked fiducial marks on the sample surface to measure strain during the tensile loading of the sample. They observed macroscopic yielding in the sample which was absent in Balk's results. Although Balk and co-workers did not see any macroscopic yielding in the stress-strain curves, the fracture surfaces showed Au ligaments broken in ductile manner. Biener et al. [75] studied microscopic failure of NPG with different ligament size. They observed failure by plastic flow and necking in NPG of ligament size ~ 100 nm and failure by slip in the porous gold with ligament size ~ 1000 nm. They concluded this to be a size effect where the smaller ligament size suppresses the dislocation activity. Jin and Weissmuller [11] studied effect of potential on the strength of NPG in compression. They observed ~ 30% increase in the flow stress for oxidized NPG sample as compared to a non-oxidized NPG sample.

1.4 Fracture Mechanics and Dynamic fracture:

(All the equations in this section correspond to a plane stress condition, as all of the NPG samples tested are "thin". In plane strain conditions, the Young's modulus (E) in the stress intensity equations can be replaced by an effective Young's modulus given by $E/(1-\nu^2)$ where v is the Poisson's ratio.)

The theoretical strength of the material, estimated from the amount of energy needed to break bonds between atoms, is ~ E/π, where E is the Young's modulus of the material. However,

practically, the measured strength of the materials is few orders of magnitude smaller than this number. This huge discrepancy is the effect of presence of “cracks”. Inglis [76] was the first to show that the existence of an elliptical shaped crack in a linear elastic sheet amplifies the stress near the vicinity of the crack. Griffith [77] later used energy balance to calculate the relation between applied stress (σ_c) and size of a crack (a) in equilibrium, in terms of Young’s modulus (E), surface free energy (γ) as

$$\sigma_c = \sqrt{\frac{2E\gamma}{\pi a}} \qquad 14$$

Although this equation could predict fracture stress values for brittle materials like glass, it failed for ductile materials such as steel, aluminum. Irwin [78] proposed the significance of plasticity at the crack tip in fracture. The stress field at the crack tip goes as $\sigma \sim 1/\sqrt{r}$, where r is the distance from the crack tip. This creates a singularity at the crack tip, as $r \to 0$, $\sigma \to \infty$ according to the relation. However this is practically impossible as even for a perfectly brittle material, r cannot get any smaller than interatomic spacing at the atomic level. For ductile materials, a concept of “process zone” is used where the continuum theory (the $1/\sqrt{r}$ singularity) breaks down. Size of this process zone or plastic zone in ductile materials is approximated by equating the stress obtained through the $1/\sqrt{r}$ relation to the yield stress (σ_y). Irwin used the concept of the “stress intensity factor” (K) which is given as $K \sim \sigma\sqrt{r}$. This K can be used to measure the fracture toughness of the sample which is calculated as $\mathcal{G} \sim K^2/E$. Hence it can be safely concluded that typically, knowing K for a brittle sample with a crack is sufficient to predict the behavior of the crack. This $\mathcal{G}$ is also called the strain energy release rate which gives the amount of energy flowing in the crack tip. Fracture energy for a material, Γ, is defined as the amount of energy required to create a fresh surface per unit crack extension per unit thickness. This Γ, although independent of loading conditions, is a rate-dependent function and depends on the instantaneous crack velocity. The Γ encompasses all the energy required to create a crack including the free energy (2γ) and any other excess energy that is dissipated in the “process zone”.

For a crack moving with a velocity V, the dynamic stress intensity $\left(K_I^{dyn}\right)$ can be separated into a static component (which is the static stress intensity) and a dynamic component, k(V) which depends only on the velocity of the crack and other material properties as given by Equation 15 and 16 [79].

$$K_I^{dyn} = K_I^{stat} k(V) \tag{15}$$

where,

$$k(V) \approx \left(1 - \frac{V}{V_R}\right) \Big/ \sqrt{1 - \frac{V}{V_L}} \tag{16}$$

Here V = the crack velocity, V_R = the Rayleigh wave velocity given by Equation 17,

$$V_R = \left(\frac{0.862 + 1.14\nu}{1 + \nu}\right) V_S \tag{17}$$

where ν = Poisson's ratio and

$$V_S = \sqrt{\frac{G}{\rho}} \tag{18}$$

G = Shear modulus and ρ = Density.

The longitudinal wave velocity V_L is given by [80]

$$V_L = \sqrt{\frac{2G(1-\nu)}{\rho(1-2\nu)}} \tag{19}$$

The K_I^{dyn} can also be obtained from the displacement field on the sample surface during dynamic fracture using Equation 20.

$$\dot{u} \sim -\frac{V\alpha_s K_I^{dyn}}{GD\sqrt{2\pi r}} \left\{ (1+\alpha_s^2) \frac{\sin\frac{1}{2}\theta_d}{\sqrt{\gamma_d}} - 2\frac{\sin\frac{1}{2}\theta_s}{\sqrt{\gamma_s}} \right\} \tag{20}$$

Where $\gamma_d = \sqrt{1 - (V\sin\theta/c_d)^2}$, $\gamma_s = \sqrt{1 - (V\sin\theta/c_s)^2}$, $\tan\theta_d = \alpha_d \tan\theta$, $\tan\theta_s = \alpha_s \tan\theta$, $D = 4\alpha_d\alpha_s - (1+\alpha_S^2)^2$, $\alpha_d = \sqrt{1 - \frac{V^2}{V_L^2}}$, and $\alpha_S = \sqrt{1 - \frac{V^2}{V_s^2}}$. Here r and θ are co-ordinates of the point with respect to the crack tip and $\dot{u}$ is the displacement rate.

The corresponding dynamic fracture toughness is given by Equation 21

$$\mathcal{G}^{dyn} = \frac{{K_I^{dyn}}^2}{E} A \quad (21)$$

Where

$$A = \frac{V^2 \alpha_d}{(1-v) V_s^2 D} \quad (22)$$

Freund [79] used a simple energy balance $\Gamma(\mathrm{V}) = \mathcal{G}^{dyn}$ to obtain an equation of crack tip motion,

$$V \approx V_R \left[1 - \frac{\Gamma(\mathrm{V})}{\mathcal{G}}\right] = V_R \left[1 - \frac{\Gamma(\mathrm{V})\ \mathrm{E}}{(K_I^{stat})^2}\right] \quad (23)$$

This equation as interpreted by Bouchbinder et al. [81], provides important insights into the crack tip motion. Here the velocity independent and load dependent value $\mathcal{G}$ determines the crack propagation. The crack cannot proceed when $\mathcal{G} < \Gamma(\mathrm{V})$. Also for $\Gamma(\mathrm{V}) \rightarrow 0$ (i.e. no resistance for crack motion) or $\mathcal{G} \rightarrow \infty$ (i.e. infinite driving force), the crack would achieve maximum velocity equal to the Rayleigh wave velocity. Also the equation depends upon the crack tip location and instantaneous velocity of the crack. However, it does not contain any term related to acceleration of the crack. The instantaneous crack velocity is determined only by the $\mathcal{G}$ and $\Gamma(\mathrm{V})$ values. In other words, any change in these values would instantaneously change the crack velocity and hence the crack can be treated as inertia-less entity. Also the dynamic contribution to the energy release rate reduces its value relative the static $\mathcal{G}$. This is effect from the excess kinetic energy needed for the crack to move the surrounding material away from the crack face. This kinetic energy increases with increase in the velocity which in turn limits the velocity to V_R. Another form of this equation as given by Berry [82]

$$V \approx V_R \left(1 - \frac{a_0}{a}\right) \quad (24)$$

where a_0 is the initial crack length, and a is the instantaneous crack length of the moving crack.

Ahn and Balogun [74] used laser ultrasonic measurements to measure shear and longitudinal wave velocities in the NPG to obtain the Young's modulus of ~ 30% dense NPG. Those were ~ 737 m/s and 438 m/s respectively.

Ravi-chandar [83] has discussed different dynamic fracture models in his review article. Discrete models of dynamic fracture involve breaking of individual atomic bond for crack propagation. MD simulations [84] of this model involves assumption of atomic interaction potential to simulate the crack propagation over nanometer length scale for picoseconds. Lattice dynamics [85] and finite elemental models [86] were also used to study the discrete model of dynamic fracture. These involve a spring mass lattice and triangular elemental analysis to simulate the dynamic fracture. Nucleation and growth model [87] of dynamic fracture assumes nucleation of micro-cracks ahead of the main crack due to stress waves which coalesce to extend the main crack in the material. This model could explain the crack surface roughness, periodicity in the roughness, and crack branching at crack speeds well below the Rayleigh wave velocity. A continuum level model [88] assumed elastic softening of material near the crack tip region and damage triggered by dilatational strain. However this model failed to explain the high crack velocities close to the Rayleigh wave velocity. Ravi-chandar [83] also compared practical techniques for crack tip determination in dynamic fracture viz. high speed camera, electrical resistance method, and Wallner line. High speed camera is an optical imaging method where images of the fracture process are captured at very high speed (few thousand to million frames per second). The electrical resistance method [89] involves attaching a thin film of metal on the sample surface and passing a constant current thorough it. As the crack propagates through the sample, the film also gets cracked which increases its resistance and therefore, the voltage. With careful calibration, this method can also be used to measure crack velocities during dynamic fracture. The Wallner lines [90] method involves imposing a small amplitude high frequency stress waves on the sample. These waves generate ripple marks on the fracture surface which can be analyzed post-mortem to obtain crack velocities. Goldman et al. [91] studied the dynamic fracture in polyacrylamide to study effect of boundaries on the crack velocity. They verified that the crack acts inertia-less until it interacts with its past history i.e. shear waves emitted by the crack which reflect from the boundary of the sample. In other words, it is the applied stress intensity that defines the crack velocity by simple energy balance where applied energy is converted into kinetic energy of the crack. Sharon and Fineberg [92] observed instability in the

crack velocity in PMMA and glass. They explained this on the basis of micro-branching of the crack that is observed at certain critical velocity $V_c \sim 0.4V_R$. They argued that above V_c a single crack is not stable and a micro-branch is formed. The energy supplied at the crack tip is divided in two cracks which leads to lower crack velocity. However, as soon as the branched crack stops propagating, all the energy is again concentrated back to the crack tip. The crack being inertia-less, jumps instantaneously to a high velocity leading to another micro-branch formation. Although the Rayleigh wave velocity sets limit to the crack velocity in mode I fracture, Rosakis et al. [93] were able to achieve crack speeds larger than the shear wave velocity in Homalite in mode II dynamic fracture.

Digital image correlation:

The digital image correlation (DIC) is a full field non-contact technique to extract displacement, strain data from images of a sample under load. It provides a good tool to measure strain field over entire surface of the sample as well as obtaining strains for mechanical tests where use of extensometer is not feasible, which include tests involving micro/nano scale samples as well as delicate samples. Typically this technique involves sample preparation, capturing digital images of a sample that is undergoing loading at different load values using a camera, and analyzing the images using software. The basic principle of the DIC technique is based on tracking different patterns on the surface to obtain displacements using image analysis [94].

Currently DIC considers images in gray-scale (monochrome) only. These images typically have 8-bit depth (0 – 255 gray levels) captured using a CCD or a CMOS sensor camera. This requires a random speckle pattern on the sample surface. Generally an airbrush is used to paint sample surface using white and black paint. In general, a DIC software products recommend speckle pattern with a feature size ~ 5 pixels with 50% black and 50% white region on the sample surface. Hence the samples are painted with white color and the black color is sprayed on it to create a speckle pattern or vice versa. The air pressure in the airbrush, the nozzle opening of the spray, and the viscosity of the paint are adjusted in order to get a good speckle pattern (5 pixel size features with 50% black and 50% white) on the sample surface. In

order to get accurate displacement field for the sample surface, surface must be flat and the sensor of the camera should be parallel to the sample surface. Another requirement is to minimize out of plane deformation of the sample so that it can be neglected in the calculations.

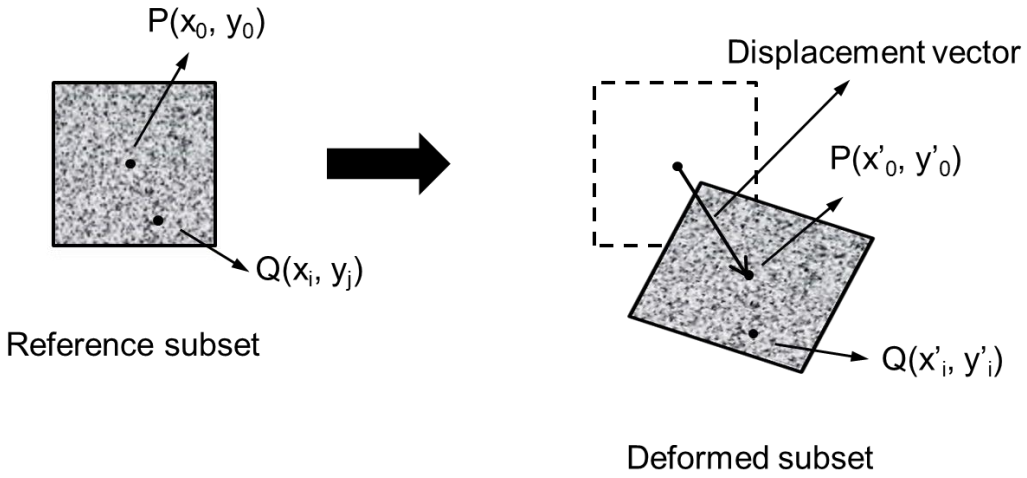

Figure 7: Schematic of a subset with a random speckle pattern before and after deformation. The gray scale intensities are compared to obtain displacement field for the deformed image.

The analysis involves defining a square subset of size (2M+1) X (2M+1) pixels, where M is an integer. As a subset contains a distribution of gray values of pixels, it is easier to track a subset than tracking a single pixel. The displacement vector can be obtained from the difference between positions of the centers of the deformed $P(x_0', y_0')$ and non-deformed $P(x_0, y_0)$ subsets (Figure 7). The deformation also causes shape change of the subset. Based on the assumption of continuity of deformation, the positions of the neighboring points in the deformed subset can be determined. E.g. a point $Q(x_i, y_j)$ in the non-deformed image can be mapped to the point $Q(x_i', y_j')$ in the deformed image. The new co-ordinates of the point Q in the deformed image can be expressed as,

$$x_i' = x_i + \xi(x_i, y_j) \quad 25$$

$$y_j' = y_j + \eta(x_i, y_j) \quad 26$$

where $(i, j = -M : M)$

$$\xi(x_i, y_j) = u + u_x \Delta x + u_y \Delta y + \frac{1}{2} u_{xx} \Delta x^2 + \frac{1}{2} u_{yy} \Delta y^2 + u_{xy} \Delta x \Delta y \quad 27$$

$$\eta(x_i, y_j) = v + v_x \Delta x + v_y \Delta y + \frac{1}{2} v_{xx} \Delta x^2 + \frac{1}{2} v_{yy} \Delta y^2 + v_{xy} \Delta x \Delta y \quad (28)$$

Here, $\Delta x = x_i - x_0$, $\Delta y = y_i - y_0$,

u, v are the x and y directional displacement components of the center of the reference subset. u_x, u_y, v_x, v_y are the first order displacement gradients of the reference subset and $u_{xx}, u_{yy}, u_{xy}, v_{xx}, v_{yy}, v_{xy}$ are the second order displacement gradients of the reference subset.

This point Q can be at a sub-pixel position in the deformed image. Hence before applying any cross-correlation criterion, some interpolation schemes are applied to find sub-pixel location of point Q [95, 96, 97]. The gray scale pattern around the center pixel is analyzed and similar pattern is searched over certain range to identify location of the deformed subset in the deformed image. A cross-correlation (CC) function or sum-squared difference (SSD) correlation criterions are defined in order to evaluate the degree of similarity between the reference subset and the deformed subset [94].

A zero-normalized cross-correlation criterion (ZNCC) is most commonly used as it is insensitive to offset and linear scale in illumination lighting. Hence it provides robust noise-proof performance. Its coefficient is given by Equation 29. [94]

$$C_{ZNCC} = \sum_{i=-M}^{M} \sum_{j=-M}^{M} \left\{ \frac{[f(x_i, y_j) - f_m] \times [g(x_i', y_j') - g_m]}{\Delta f \Delta g} \right\} \quad (29)$$

Where,

$$f_m = \frac{1}{(2M+1)^2} \sum_{i=-M}^{M} \sum_{j=-M}^{M} f(x_i, y_j) \quad (30)$$

$$g_m = \frac{1}{(2M+1)^2} \sum_{i=-M}^{M} \sum_{j=-M}^{M} g(x_i', y_j') \quad (31)$$

$$\Delta f = \sqrt{\sum_{i=-M}^{M} \sum_{j=-M}^{M} [f(x_i, y_j) - f_m]^2} \quad (32)$$

$$\Delta g = \sqrt{\sum_{i=-M}^{M} \sum_{j=-M}^{M} \left[g\left(x_i', y_j'\right) - g_m \right]^2} \quad 33$$

$f\left(x_i, y_j\right)$ and $g\left(x_i', y_j'\right)$ are intensity distributions in a non-deformed and target deformed subset.

The C_{ZNCC} is calculated as a function of $u, v, u_x, u_y, v_x, v_y, u_{xx}, u_{yy}, u_{xy}, v_{xx}, v_{yy}$, and v_{xy} and its maxima gives displacement values of the points in the deformed subset. The SSD criterion is related to the CC criterion [98]. In case of the ZNCC,

$$C_{ZNCC}(p) = 2[1 - C_{ZNSSD}(p)] \quad 34$$

The position of the deformed subset can be determined by detecting maxima of the CC function or minima of the SSD function. Differentiating the displacements gives strain field on the sample surface.

3-D and volume DIC are also part of commercial software products. The 3-D DIC uses 2 cameras to capture image of the sample surface at certain angles. This technique also measures out of plane displacements of the sample surface [99, 100, 101, 102]. X-ray tomography is used to capture volume images of the sample for the volume DIC which can give strain distribution inside volume of a material [103, 104].

Kirugulige et al. [105] used high speed digital photography to study the dynamic fracture in epoxy resin. They put a random speckle pattern on the sample surface. These samples were then impact loaded to achieve mode I fracture. They used a high speed camera which captured a total of 32 one-megapixel images at 225,000 frames per second of the sample during the fracture process. These images were later analyzed using digital image correlation to obtain displacement field on the sample surface. These displacement fields were used to measure the stress intensity of the sample during the fracture process. They claimed displacement resolutions of 2 – 6 % of a pixel size. Abanto-Bueno and Lambros [106] studied dynamic fracture in homogeneous and functionally graded polymer using digital image correlation. They calculated the dynamic stress intensity from the displacement field on the sample surface and verified these near tip methods

with far field measurements. Roux et al. [107] also showed that crack tips which would be invisible to the bare eyes, can be observed with sub pixel resolution using the DIC techniques. Roux and Hild [108] claimed displacement resolution of 75 nm using DIC even though the images were captured using optical methods. They also measured stress intensity factors in three point bend test of SiC with 7% error. Tarigopula et al. [109] used DIC along with high speed imaging to study dynamic tensile behavior of high strength steel. They observed that using different mesh densities while performing the DIC analysis affects the accuracy of the results.

CHAPTER 2

EXPERIMENTS

During dealloying a silver-gold (Ag-Au) alloy sample, we selectively leach out silver from the sample and a porous layer depleted in silver is generated on the surface. For a polycrystalline sample, we observe deeper dealloying along the grain boundary. Applying stress on a sample with a dealloyed porous layer on the surface generates cracks in the porous layer. For polycrystalline samples, some of these cracks which are generated at the grain boundary penetrate beyond visible (in the SEM) corroded layer along the grain boundary. Our aim is to find whether the crack penetrates past the corroded region along the grain boundary. Crack injection experiments were performed for this purpose. These are explained in detail later. Another set of experiments were performed to study mechanical properties of the NPG. These involve tensile test to measure Young's modulus, fracture stress, Poisson's ratio, fracture toughness test to measure critical stress intensity and fracture toughness, and dynamic fracture test to measure crack velocity, and stress intensity factors during the dynamic fracture.

All the Ag-Au alloy material was polycrystalline supplied by Goodfellow Corporation, USA. It was prepared using 99.999% pure elemental raw metals.

Table 2 Alloy materials used in the experiments

Alloy (atomic comp. %)	Thickness	Treatment	Experiment
$Ag_{72}Au_{28}$	125 um	a	Tensile test, CTOD test, Dynamic fracture test
$Ag_{70}Au_{30}$	125 um	b	Crack injection, Atom probe tomography, SCC
$Ag_{80}Au_{20}$	125 um	b	Crack injection
$Ag_{70}Au_{30}$	50 um	b	Crack injection

a. Polished with grit 800, 1200 silicon carbide paper, and then 1 um, 0.3 um, and 0.05 um alumina followed by heat treatment in atmospheric furnace at 900^{o}C for 2 hours and air cooled to relieve internal stresses
b. Polished with grit 800, 1200 silicon carbide paper, and then 1 um alumina followed by heat treatment in atmospheric furnace at 800^{o}C for 12 hours and air cooled to relieve internal stresses

Two $Ag_{70}Au_{30}$ samples (3 mm X 15 mm X 125 um) were tested to verify the intergranular SCC. A specially designed Teflon cell was used to perform these tests. The samples were held in specially designed grips made of PEEK and immersed in the electrolyte (1M $HClO_4$ + 10^{-3}M Ag^+) and pulled in tension at constant displacement rate. The test was performed using Gamry potentiostat. A platinum wire was used as a counter electrode and mercury / mercurous sulfate (MSE) was reference electrode (640 mV vs standard hydrogen electrode - SHE). The critical potential for $Ag_{70}Au_{30}$ sample is 0.99 – 1.02 V [110]. The potential used for both of the tests was set higher than the critical potential to ensure the porous structure formation. Table 3 lists the experimental details for these tests.

Table 3: SCC tests details

Sample	Voltage	Displacement rate
SCC1	1.05 V	0.25 um/s
SCC2	1.15 V	1.0 um/s

2.1 Crack Injection Experiments:

These experiments were performed on different AgAu alloy sheet samples (table 2). The dimensions of the AgAu alloy thin sheet samples were typically 2 mm X 15 mm. These samples, after polishing and heat treatment, were connected to a copper tape for connection to a Gamry potentiostat. The samples were then placed in a three electrode cell, the sample being the working electrode, with a platinum wire counter electrode and MSE reference electrode. The Pt wire was cleaned using concentrated nitric and sulfuric acid followed by rinsing with de-ionized (DI) water and H_2 flame annealing. The reference electrode was used with a salt bridge to avoid any ionic contamination which could affect the electrolyte concentration as well as cause fluctuations in the reference electrode voltage. The tip of the salt bridge was also cleaned with DI water before immersing it into the electrolyte. Two different electrolytes were used for these tests. Some tests were performed in a neutral electrolyte 0.1M $AgNO_3$ whereas 1M $HClO_4$ was used for rest of the tests. The electrolytes were prepared using reagent grade $AgNO_3$ and $HClO_4$ respectively along with ultra-high purity water. One test was performed on a sample from $Ag_{80}Au_{20}$ sheet which was dealloyed at very high current density and bent. The motivation for this

specific test came from the previous work by Dr. Fritz Friedersdorf [56]. During his tests, he obtained brittle cracks 50 – 60 times deeper than the bulk dealloyed layer thickness. However, the samples were loaded in uniaxial tension inside the electrolyte at a potential below the critical potential for dealloying.

These samples were dealloyed at different potentials to generate a thin porous layer on the sample surface. Thickness of this layer varied from ~ 300 nm – 1000 nm. As soon as the dealloying was over, the samples were taken out of the electrolyte and immersed in ultra-high purity water for 10 s to inhibit any extra corrosion. Some samples were immersed in the liquid nitrogen (LN_2). The LN_2 inhibits the corrosion by converting any trapped electrolyte to ice and also stops coarsening of the porous gold ligament [54]. After certain time (typically 10 seconds for water, 1 hour for LN_2) the samples were taken out of the water or LN_2 and bent by hand immediately into V shape. This bending puts stress on the porous layer and cracks are generated inside it. Table 4 provides details of the crack injection experiments.

Table 4 Experimental details of the crack injection samples

#	Sample info.	Dealloying conditions			Post dealloying treatment
		Electrolyte	Voltage vs SHE (approx. current density)	time	
1	$Ag_{70}Au_{30}$ 125 um	0.1M $AgNO_3$	1.8 V (X*)	40 s	Dipped in H_2O for 10 s bent by hand heated to 300^oC for 10 mins
2	$Ag_{70}Au_{30}$ 125 um	1M $HClO_4$	1.260 V (6 mA/cm^2)	60 s	Dipped in H_2O for 10 s bent by hand
3	$Ag_{70}Au_{30}$ 125 um	1M $HClO_4$	1.240 V (1 mA/cm^2)	180 s	Dipped in H_2O for 10 s bent by hand
4	$Ag_{70}Au_{30}$ 125 um	1M $HClO_4$	1.280 V (10 mA/cm^2)	30 s	Dipped in H_2O for 10 s bent by hand
5	$Ag_{70}Au_{30}$ 125 um	1M $HClO_4$	1.260 V (6 mA/cm^2)	30 s	Dipped in LN_2 for 1 hr bent by hand
6	$Ag_{80}Au_{20}$ 125 um	1M $HClO_4$	1.215 V (~40 mA/cm^2)	15 s	Dipped in H_2O for 10 s bent by hand
7	$Ag_{70}Au_{30}$ 125 um	1M $HClO_4$	1.260 V (6 mA/cm^2)	60 s	Dipped in H_2O for 1 hr bent by hand
8	$Ag_{70}Au_{30}$ 125 um	1M $HClO_4$	1.260 V (6 mA/cm^2)	60 s	Dipped in H_2O for 10 s bent by hand 5 days later
9	$Ag_{70}Au_{30}$ 125 um	1M $HClO_4$	1.260 V (6 mA/cm^2)	60 s	Dipped in H_2O for 10 s (no bending, control)
10	$Ag_{70}Au_{30}$ 125 um	1M $HClO_4$	1.240 V (1 mA/cm^2)	180 s	Dipped in H_2O for 10 s (no bending, control)
11	$Ag_{70}Au_{30}$ 125 um	-	-	-	(no dealloying, control)

* Current density cannot be determined as water oxidation also takes place along with the dealloying at 1.8 V.

Some samples for the crack injection experiments were also obtained from a 50 um thick AgAu alloy sheet. These samples underwent same procedure as sample 1. All the 50 um thick samples were cross-sectioned and examined in the focused ion beam (FIB).

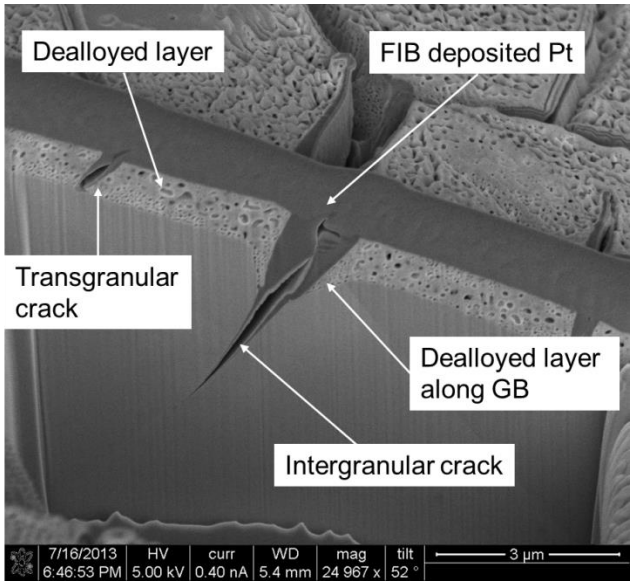

Figure 8: Cross-section of a crack along a grain boundary in a dealloyed sample (Sample 1)

As seen in the Figure 8, typically the dealloying along the grain boundary has been observed to be deeper than the bulk dealloyed layer thickness. Some of the intergranular cracks penetrate beyond the visible depth of the dealloyed layer along the grain boundary. This can be observed by milling the sample along a wide open grain boundary in a focused ion beam microscope. Figure 8 shows one of such cross-section of an intergranular crack in a dealloyed sample that was bent.

Crack milling in a focused ion beam (FIB) microscope:

Focused ion beam (FIB) microscope (Figure 9) works on same principle as a secondary electron microscope (SEM), except that the FIB uses an ion beam instead of an electron beam. This was developed from the principles of field ion microscopy [111]. The ion beam interacts with the sample surface to produce secondary electrons. A liquid metal ion source (LMIS) – mostly gallium (Ga+) ion source is used in the FIB instruments. Ga has melting point of $30^{O}C$ with low volatility and low vapor pressure which makes it an ideal choice for the ion beam source [112]. The Ga liquid metal flows to a tungsten (W) needle tip through capillarity. The needle tip has ~ 10 um radius of curvature. A large negative potential between the needle tip and the extraction electrode generate an electric field of magnitude ~ 10^{10} V/m. This electric field generates an ion beam at the tip of the tungsten needle. The column typically has two lenses – condenser lens for

probe forming and objective lens for focusing the beam on the sample. Set of apertures are used to control the probe size and ion current (typically 10 pA – 30 nA). The beam column also consists of deflection plates to raster beam over the sample surface, stigmation poles to make the beam spherical, and high speed beam blanker to deflect beam away from the sample.

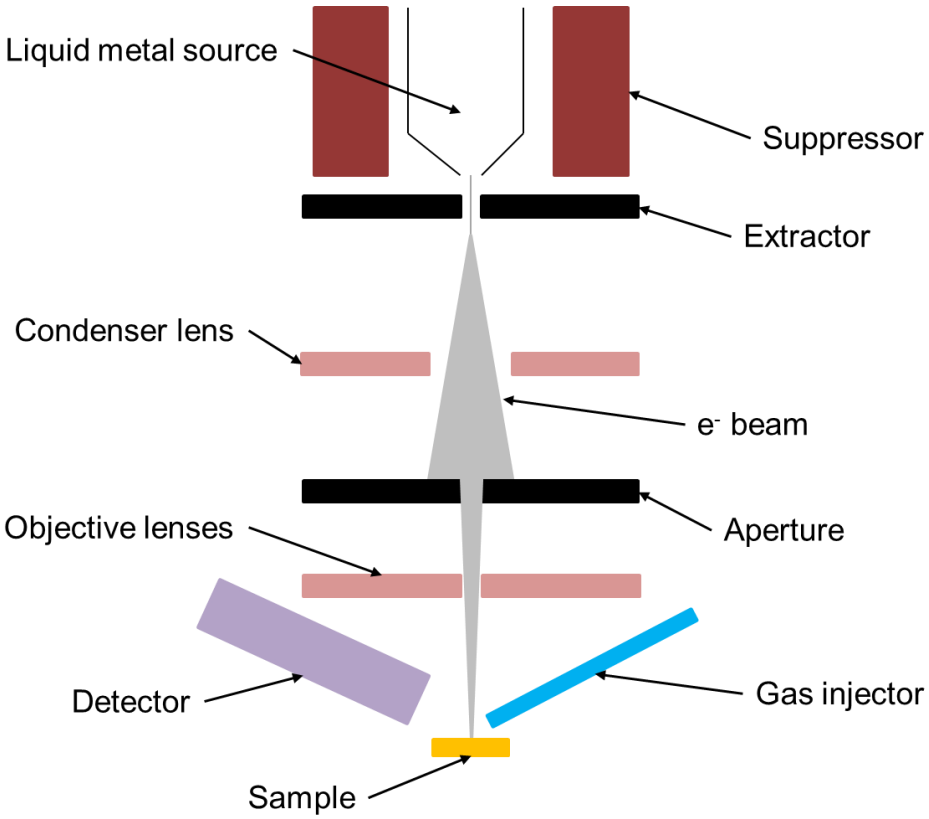

Figure 9: Basic schematic of a focused ion beam (FIB) microscope

The FIB is mainly used for imaging, milling, and deposition. Most of the ion beam instruments have dual beam channels (SEM and FIB), where the ion beam usage is limited to milling and deposition. The electron beam is used for non-destructive imaging of the sample surface. As the Ga+ ions hit the sample surface, the ion and the sample material interacts. As the kinetic energy of the ion is transferred to the sample surface, several processes occur simultaneously, which include sputtering of sample atoms and ion generation, secondary electron generation, sample heating, sample damage, ion reflection and backscattering, and

electromagnetic radiation. The secondary electrons are collected by the detector to form sample image. The resolution can be manipulated by adjusting beam diameter and sputtering rate through beam current. At very low beam currents, 5 – 10 nm imaging resolution can be achieved. A FIB can also be used for depositing material on sample surface through local chemical vapor deposition (CVD). A gas source, e.g. trimethyl-methylcyclopentadienyl-platinum ($C_9H_{16}Pt$) [113] is introduced in the chamber. When the ion beam interacts with the gas, it decomposes the gas producing a deposition layer of platinum (Pt) on the sample surface. Tungsten, carbon, and gold are some other common elements used for deposition in the FIB. The size of these milling or deposition features, which can be from ~ 10 nm to hundreds of micrometers, is controlled by adjusting the beam current. The precise milling and deposition techniques have made the FIB instruments very popular in the preparation of thin specimens for TEM. The sample is generally mounted on a grounded stage which has three axis translation, rotation, and tilt movement capability.

FIB is an excellent instrument for thin TEM sample preparation. A nano-manipulator is generally installed on a FIB. This manipulator has a tungsten (W) needle attached to its end which can be maneuvered inside the FIB chamber using computer software. This W needle is used to lift out thin cross-sectioned samples and attach to a copper lift-out grid [114].

Three different FIB instruments were used to perform certain parts of the experimental work. FEI Nova 200 dual beam microscope (ASU) was used to prepare one TEM sample (sample 1). Other TEM samples (sample 2, 6, 9, 10, and 11) were prepared using FEI Quanta 3D FEG (PNNL). The atom probe tomography samples (sample 10 and 11) were prepared using FEI Helios dual beam system (PNNL). Also all the milling cross-sections that were examined in ASU were prepared using the FEI Nova 200 dual beam microscope.

To compare results obtained from the bent samples, some control samples were prepared with nominally same dealloying conditions and post treatments except that they were not bent along with two un-dealloyed samples with same polishing and annealing treatment as other samples (Table 4). One of the un-dealloyed samples was used to prepare a TEM sample and the other one was used for atom probe tomography analysis.

Analysis using the aberration corrected transmission electron microscope:

Transmission electron microscopy (TEM) is a technique where an electron beam is transmitted through a very thin sample (typically 50 – 100 nm thick). The electrons interact with the specimen as they pass through it. It is necessary to obtain a very thin beam of the electron in order to achieve high resolution. A TEM uses electromagnetic lenses for this. These lenses act to an electron beam similar to glass lenses act to a light ray. Theoretically the electrons travelling parallel to the axis of the lens are focused on a single point on the axes called focal point. However, practical lenses suffer from spherical and chromatic aberrations. Spherical aberration causes rays travelling away from the axis to bend more than those travelling close to the axis (Figure 10). This results in the rays not converging on a single focal point affecting the resolution of the TEM.

The aberration corrected TEMs incorporate extra electromagnetic lenses which act like a concave lens to correct the effect of aberration caused by the convex lenses. The TEM sample (# 1) prepared using the focused ion beam microscopes in ASU was analyzed in JEOL 2010F. Other TEM samples (sample 2, 6, 9, 10, and 11) were analyzed using JEOL ARM 200 aberration corrected TEM in ASU. The analysis involved high magnification imaging and energy dispersive spectroscopy (EDS) analysis at different spots to identify elemental composition.

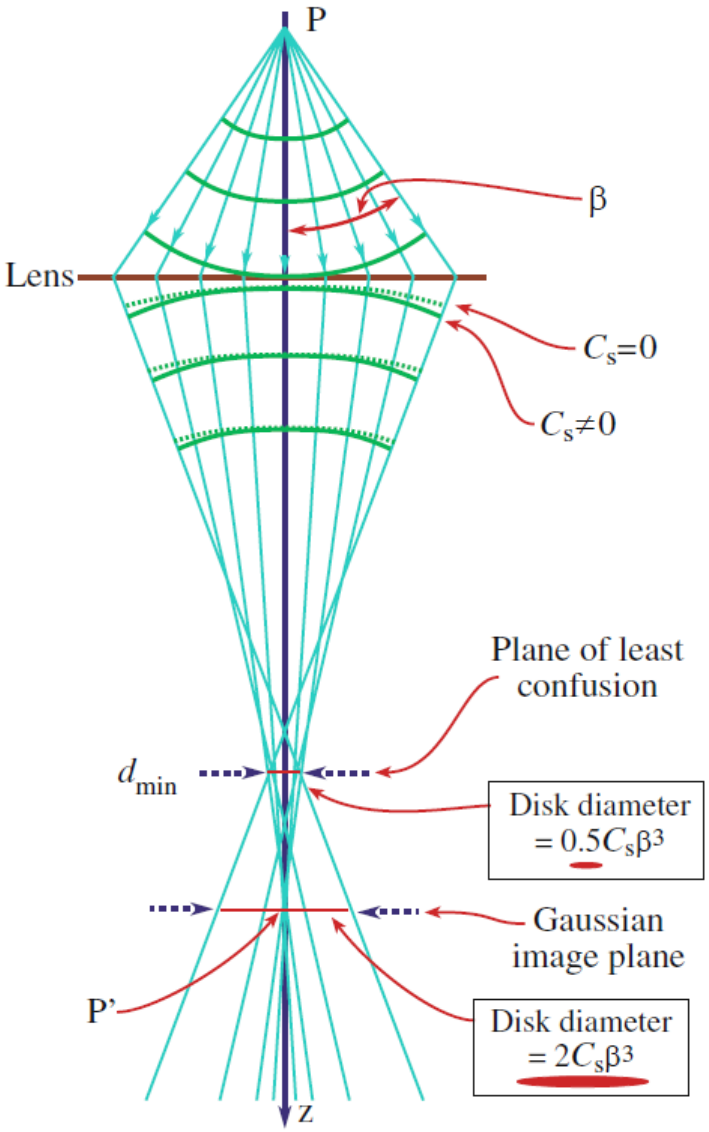

Figure 10: Spherical aberration causes off axis rays to bend more than the rays close to the axis. This results in the wavefront coming from a point object to get spherically distorted. Smallest image of the point object is created at the plane of the least confusion [115].

EDS quantitative analysis:

All the EDS data from Gatan DigitalMicrograph was saved as text file and analysed in Matlab. A Matlab code (Appendix A) was written to subtract the background, identify Ag and Au peaks, and measure counts at full width half maximum. The background subtraction was done using the window method which involves fitting the background to a straight line using the data where any peak is not present [115]. These counts were then converted to percentage

composition of Ag and Au for the specific scan location which was mapped back to the corresponding image. The crack was filled with Pt during FIB milling. Lα peaks are very close to each other for Pt and Au since they are next to each other in the periodic table. Lα peak for Pt is 9.44 keV whereas that for Au is 9.71 keV. Typical size of the window for measuring counts of Ag and Au is 40-50 eV which corresponded to the full width half maximum of the peak. Hence if there is presence of Pt in the effective volume scanned, it could artificially increase Au counts and introduce error in the analysis. This was tried to avoid by measuring ratio of total counts of Pt and total counts of Au in the region where Pt was certainly not present for the specific scan. Once the ratio increases beyond average + 3*standard deviation of the values in the "no Pt region", the scan point was labelled as Pt affected zone and neglected from the compositional analysis.

The quantitative analysis was done based on Cliff – Lorrimer analysis [116]. The analysis involves measuring counts for A and B from a known composition region and using that as a reference to calculate a constant known as Cliff – Lorrimer factor (k_{AB})

$$\frac{C_A}{C_B} = k_{AB} \times \frac{I_A}{I_B} \qquad 35$$

Where I_A and I_B are characteristic intensities after background subtraction for element A and B and C_A and C_B are weight percentages of elements A and B respectively. Later when calculating the composition for an unknown region, this constant can be used to get the actual composition again using the Equation 35. This k factor can be affect by sample thickness [117]. The TEM samples prepared in FIB are typically wedge shaped where thickness of the sample at the top is highest and it reduces towards the bottom of the sample e.g. the sample 2 was ~ 100 nm thick at the top and the thickness decreased to 15 nm at the bottom of the sample as measured using EELS technique [115]. Hence for almost all the line scans some part of the un-corroded region was included while obtaining the data. The Matlab analysis takes start and end point of this region as input and uses that to calculate the k factor for every scan individually.

Atom probe tomography:

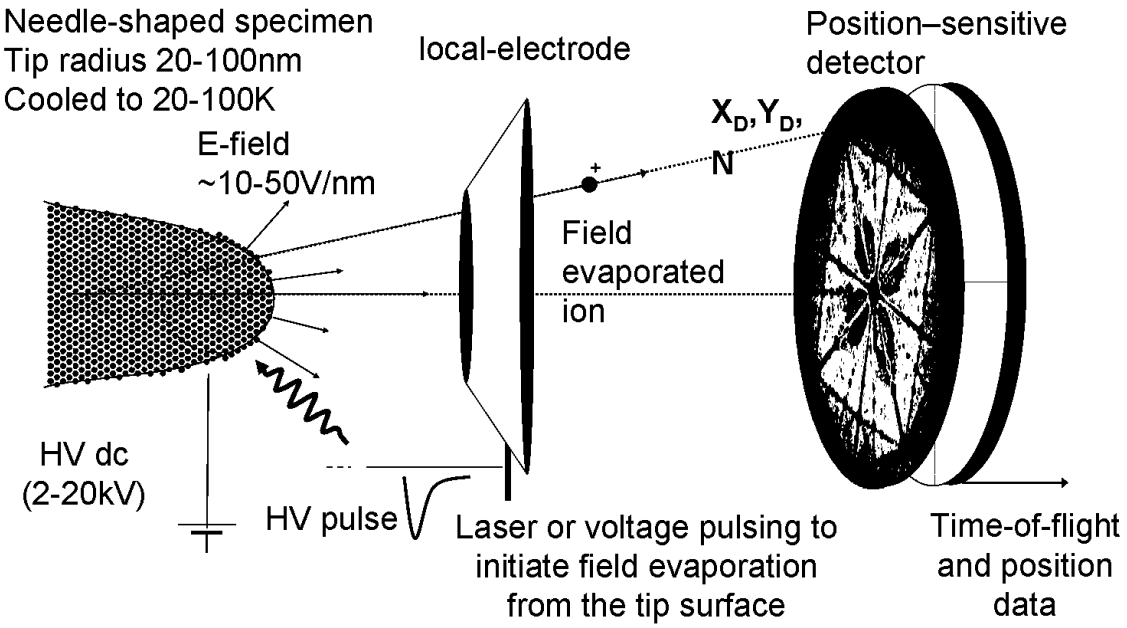

Figure 11: Schematic of atom probe tomography (APT) working principle [118]

Atom probe tomography (APT) (Figure 11) is an instrument developed from the basic principles of field ion microscope [111, 119]. The sample is typically a sharp needle with radius of curvature ~ 50 – 100 nm with the taper angle at the apex of the needle no larger than 10^{o}. The samples are cryogenically cooled to ~ 20 – 100 K in ultrahigh vacuum placed ~ 5 cm from a phosphor screen pointing towards it. A small amount of image gas (generally helium or neon) is introduced in the vacuum chamber till the pressure is ~ 10^{-5} mbar. A very high voltage pulses (~ 1 – 20 kV at ~ 100 – 200 kHz) are applied to the specimen. The radius of curvature of the tip of the sample keeps increasing as atoms from the tip are evaporated. Hence to keep the electric field constant, the voltage applied to the sample is increased continuously at a specific rate depending on the sample. The applied voltage pulse produces high electric field (few volts per nanometer) at the sample tip which polarizes the image gas atoms near the tip. These atoms are attracted to the tip and get ionized. This ionization process produces positively ionized atoms from the sample tip. These positive ions are radially repelled from the positively charged sample towards the phosphor screen. The delay between application of the pulse and ion detection gives time of flight for the

ion which gives information about mass-to-charge ratio of the detected atoms. This information is then used for atomic reconstruction of the sample.

The APT samples are prepared using either electro-polishing or ion milling depending on the material, original shape, and type of the specimen [120, 121]. The sample preparation involves lift-out of a wedge shaped bar using a FIB from the region of interest, mounting the sample on commercial silicon micro-posts array for APT, and sharpening using ion milling to obtain a needle-like geometry.

This work was performed in Pacific Northwest national laboratory (PNNL) with the help of Dr. Daniel Schreiber. Samples were prepared on dual-beam Helios SEM / FIB. Two different samples from a 70-30 sheet (Table 2) were analyzed using the atom probe tomography. Two samples of different grain boundaries from an un-dealloyed sample (# 11) were used for the reference compositional analysis in the sample before corrosion. Three APT samples from a grain boundary in a dealloyed sample (# 10) were analyzed. These samples were extracted from regions ~ 60 nm, ~ 660 nm and ~1700 nm below the surface of the sample.

Mechanical cross-sectioning:

Some of the crack injection samples (# 3, 4, 5, and 6) were mounted in epoxy and mechanically cross-sectioned along the thickness. The epoxies used to mount the sample were long cure (6 – 8 hours) two part epoxies obtained from Buehler (EpoThin) and Allied Tech (EpoxySet). Pieces of glass or aluminum were mounted in the epoxy touching the sample surface in order to obtain good edge retention during polishing of the sample. After the epoxy hardened, the sample was polished on grit 400 –> 600 –> 800 –> 1200 silicon carbide paper followed by 1 um, 0.3 um, and 0.05 um alumina. Sample # 5 was also polished on vibratory polisher (Pace technologies) using 0.05 um alumina. These samples were examined in a SEM.

2.2 Mechanical Testing of NPG:

Micromechanical testing device assembly:

A motorized stage (Thorlabs, Inc. - MTS25-Z8) was used as an actuator for the micromechanical testing device (Figure 12). This motorized stage has speed range of 3 um/s to 2.4 mm/s. The total displacement range is 25 mm and maximum horizontal load capacity is 25

lbs. Minimum incremental displacement that can be achieved by the stage is 0.05 um. A 25 lb-load cell (SMA-25, Interface, Inc.) was used to measure the load. A dial indicator was used to ensure alignment of the grips. Sample images were captured using Nikon D3200 (24 MP) camera along with 49 mm extension tube-set and 18-55 mm f/3.5-5.6 AF-S DX VR NIKKOR Zoom Lens. The strain measurement was done using digital image correlation. Some of the tensile and crack tip opening displacement (CTOD) experiments were performed using "EO-5012M ½" CMOS Monochrome USB microscope camera mounted on Zeiss Stemi 2000-C stereo microscope for image capturing. The images were analyzed using ARAMIS to obtain the displacement and the strain field.

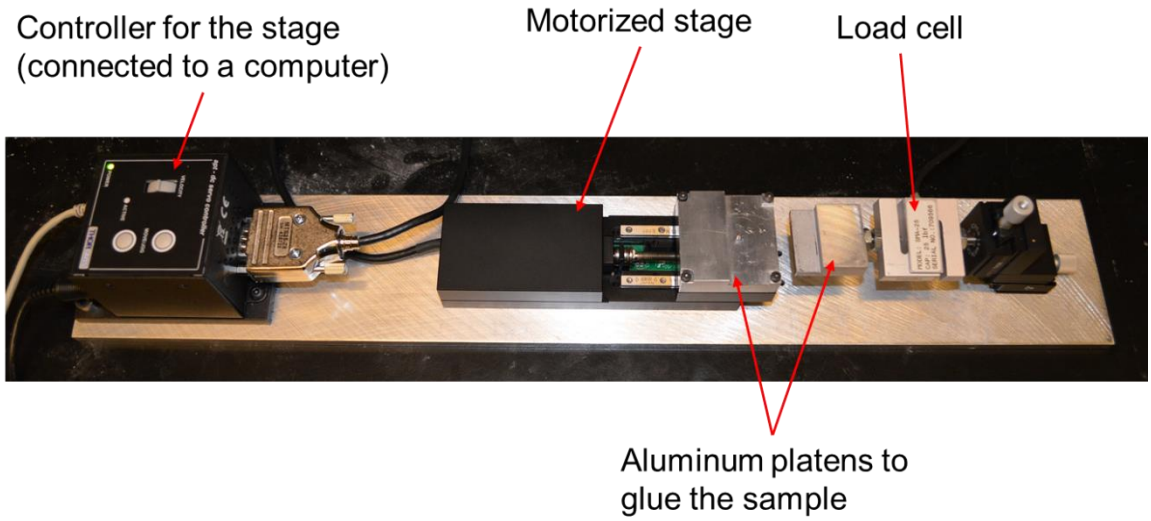

Figure 12: Picture of the micromechanical testing device

Monolithic NPG preparation:

$Ag_{72}Au_{28}$ alloy sheets were used for monolithic NPG sample synthesis. These samples were cut into rectangular sheets using wire electric discharge machine (EDM). Dimensions of these sheets differ for different tests and are mentioned separately in the specific sections. After polishing and annealing (Table 2), these samples were placed on a thin gold film deposited on a mica substrate using e-beam deposition. A thin gold wire was wound to the sample and the gold film for electrical connection. The sample was then immersed in 1M HNO_3 and potentiostatically dealloyed at ~ 535 mV vs MSE (corresponding to 1 mA/cm^2 current density). The dealloying was carried out until the current dropped below 5 uA to ensure complete dealloying. The NPG

samples obtained using this technique has nominally 40 nm ligament size. Monolithic NPG samples were oxidized and their properties were also studied. In order to oxidize the samples, they were wound on the thin gold film with a gold wire. The samples were then oxidized in 1M $HClO_4$ by applying 0.760 V vs MSE (1.4 V vs SHE) with Pt wire as counter electrode using a Gamry potentiostat.

Tensile test:

3 mm X 15 mm rectangular samples cut using wire EDM were used for the tensile tests. Some oxidized samples were 1 mm X 15 mm. These samples were polished, annealed (Table 2) and dealloyed to get monolithic NPG samples for the tensile test. A speckle pattern was then painted on the samples using an air brush and white paint. Then the samples were glued on micromechanical testing device using 5 minute epoxy (Figure 13). On axis alignment was checked under the camera and microscope before gluing the samples.

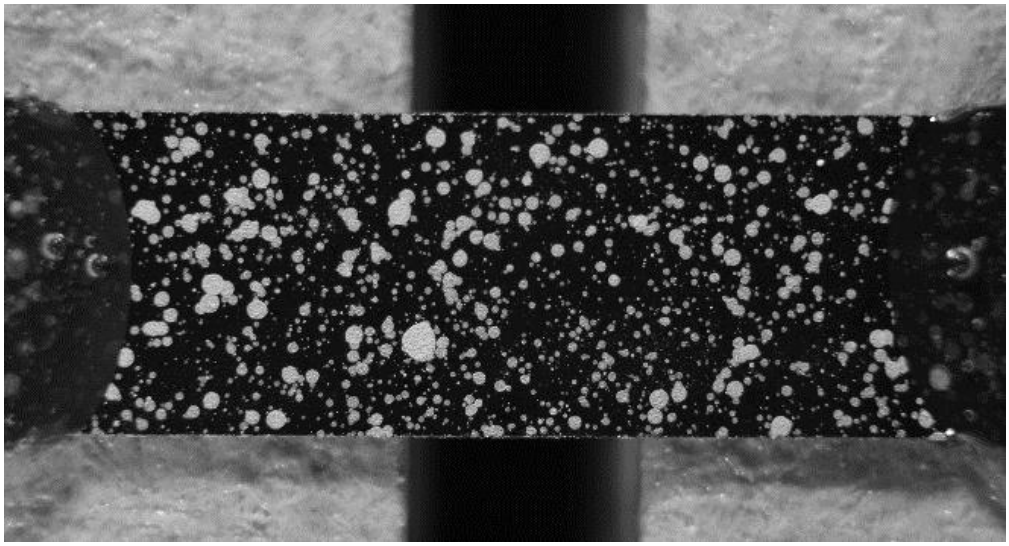

Figure 13: Tensile test sample with speckle pattern glued on the micromechanical testing device.

The tensile test for Young's modulus measurement was performed in steps. For every step the stage was moved by a displacement of 2 – 5 um (constant for a particular test) at speed of 3 um/s. An image was captured using the camera and the load value from the load cell was noted. Strain values obtained from the images along with the load values were used to plot the stress – strain curve for the NPG and obtain the Young's modulus, Poisson's ratio and the

fracture stress. Young's moduli for all the samples were measured on loading and unloading parts of the stress – strain curve. Finally all samples were loaded to fracture to get tensile strength. Three NPG and three oxidized NPG samples were tested using the technique.

Dynamic fracture test:

A 125 um thin sheet of $Ag_{72}Au_{28}$ alloy was cut into a rectangular sheet with a notch as shown in the figure 14 by electric discharge machine (EDM) using a 30 um wire at Majer Precision Engineering, Inc. This sample was then polished and annealed as mentioned in the table 2. After completely dealloying the sample, it was painted with white speckle pattern using an airbrush and white paint. Some of the samples were glued on a vise while some other were glued on the grips of the micromechanical testing device using 5 minute epoxy glue.

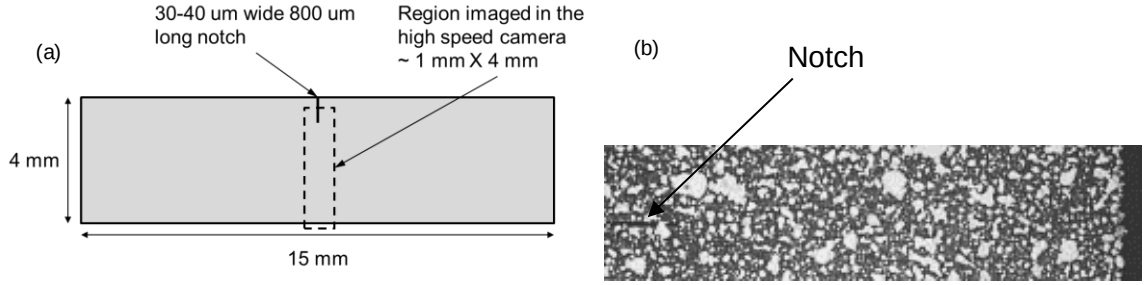

Figure 14 (a) Schematic of the sample for the dynamic fracture test (b) Image (256 X 64 pixels) of a sample with speckle pattern painted on the surface captured through high speed camera Phantom V12.1 at exposure of 4.34 us before fracture.

The Phantom V12.1 high speed camera was used to study dynamic fracture of NPG. The camera incorporates a proprietary global shutter complementary metal-oxide-semiconductor (CMOS) imaging sensor. This CMOS sensor can capture images at 6242 frames per second at a maximum resolution of 1280 X 800 and 1000000 frames per second at reduced resolution (128 X 8) with pixel size of 20 um X 20 um. The high speed camera was mounted on an optical microscope (Ziess Stemi 2000 C) and used to capture images of the sample during the crack propagation. Image size was set at 256 X 64 pixels with 1.25X magnification on the microscope objective lens. The frame rate was 230000 frames/sec (~ 4.34 us/frame) with exposure time 3.91 us/frame. At this speed, the camera can save 347648 images of the sample which is equivalent of ~ 1.51 s. The camera is set for continuous recording and needs a trigger to save images. The post trigger parameter was set at 1 frame which enabled us to capture images

~ 1.51 s prior to the trigger. The motorized stage was moved at constant displacement of 50 um/s. As soon as the sample is cracked, a trigger was sent to the camera. As long as, the trigger is sent within 1.51 s from the cracking event, the crack propagation can be captured in the saved data. This was fairly easy, as the live images are continuously monitored on a computer. One NPG and two oxidized NPG sample were tested using the technique. Load displacement data was also obtained for these samples to get fracture toughness and critical stress intensity. Three NPG samples were also tested by gluing them to a vise and manually turning the micrometer head connected to the vise to load the sample quickly and get the dynamic fracture data.

Fracture toughness measurement:

The samples used for the fracture toughness tests were same as the dynamic fracture test samples. These samples were fractured by loading them on the micromechanical testing device at a constant displacement rate of 3 um/s. The data from the load cell was obtained at a rate of 2500 Hz (maximum for the data acquisition software). The maximum value of the load was used to calculate the fracture stress (σ_f) of the sample. This value was then used to measure the critical stress intensity (K_{IC}) using Equation 36 and 37 [122].

$$K_{IC} = Y\sigma_f\sqrt{a} \tag{36}$$

$$Y = 1.99 - 0.41\left(\frac{a}{w}\right) + 18.7\left(\frac{a}{w}\right)^2 - 38.48\left(\frac{a}{w}\right)^3 + 53.85\left(\frac{a}{w}\right)^4 \tag{37}$$

Here a is the length of the notch (800 um) and w is the sample width (4000 um).

The fracture toughness was calculated using Equation 38

$$\mathcal{G} = \frac{K_{IC}^2}{E} \tag{38}$$

Apart from the three samples that were tested for the dynamic fracture, three non-oxidized and two oxidized samples were tested to obtain load-displacement data to fracture.

Crack tip opening displacement (CTOD) experiment:

These samples were same as the dynamic fracture test sample. The samples were painted with a speckle pattern and glued on the micromechanical testing device. Nikon D3200 (NPG) and EO-5012M ½ CMOS USB camera (Oxidized NPG) were used along with Zeiss

microscope (Stemi 2000 C) to capture images of the sample. The samples were loaded to different load values and images of the notch were captured. These images were analyzed using ARAMIS to obtain displacement field on the sample surface. The crack tip opening displacement (δ) value along with the corresponding load can be used to obtain yield stress (σ_y) of the NPG sample using Equation 39 [122].

$$\delta = \frac{4K_I^2}{\pi E \sigma_y} \tag{39}$$

Here K_I is just the stress intensity calculated using Equation 36 by replacing σ_f by σ which is the stress calculated at the corresponding load value. One NPG and one oxidized NPG samples were tested to obtain the yield stress from CTOD measurements. More tests were not possible because of limited resources.

DIC displacement resolution determination:

One of the notched – sample with speckle pattern was used after it was broken in the dynamic fracture test. One end of the sample was still attached to the moving stage with glue. Images of this specimen were collected in while moving the stage in one direction by 5 – 10 steps with step size of 0.1 um, 0.2 um, 0.5 um and 1.0 um. The stage has minimum repeatable movement of 0.8 um. However, the displacement measurement collected from the software was accurate within 0.05 um. These displacement values were compared with the displacement values obtained from the DIC analysis using ARAMIS. This test was essential to obtain error in the CTOD measurements.

A similar test was performed to determine the displacement resolution for the images from the high speed camera. Pixel resolution was kept same as the dynamic fracture tests (256 X 64 with ~ 15 um per pixel). The speed for movement of the stage was set at 0.5 mm/s. The image capture rate was set at 5000, 2500 and 1000 frames per seconds which gives 0.1 um, 0.2 um and 0.5 um movement per frame. Images of the moving stage were captured and analyzed using DIC to obtain average displacement at the sample surface. This average displacement was then compared to the estimated displacement from the stage.

CHAPTER 3

RESULTS AND DISCUSSION

3.1 Crack Injection Tests Results:

SCC Tests Results:

The sample SCC1 (1.05 V, 0.25 um/s) was dealloyed at lower potential and lower loading rate than the sample SCC2 (1.15 V 1.0 um/s). This reflected in the load displacement graph as it needed larger displacement for failure (~ 400 um) compared to the sample 1 (~ 200 um). The crack propagation rate was calculated from the sample thickness and the time to fracture. It was ~ 40 nm/s for the sample SCC1 and ~ 300 nm/s for the sample SCC2. Figure 15 shows the load displacement curve for the SCC tests.

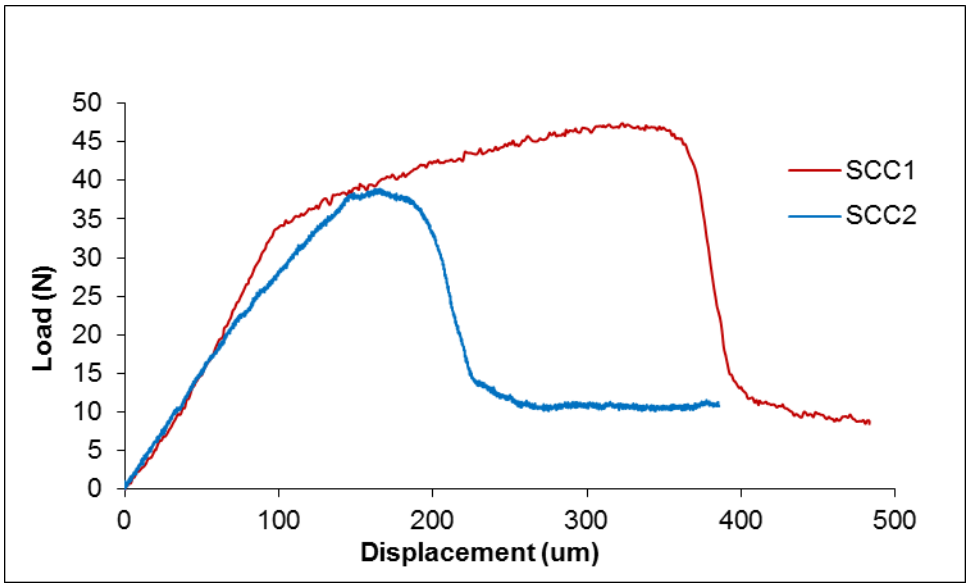

Figure 15: The load displacement data for the SCC tests showed that the sample SCC2 with higher voltage and loading rate failed at lower displacement

The main aim of these tests was to identify the nature of the fracture surface. The fracture surfaces of both of the SCC samples showed intergranular fracture (Figure 16). This observation confirms the grain boundary dealloying and intergranular SCC in polycrystalline AgAu alloy samples.

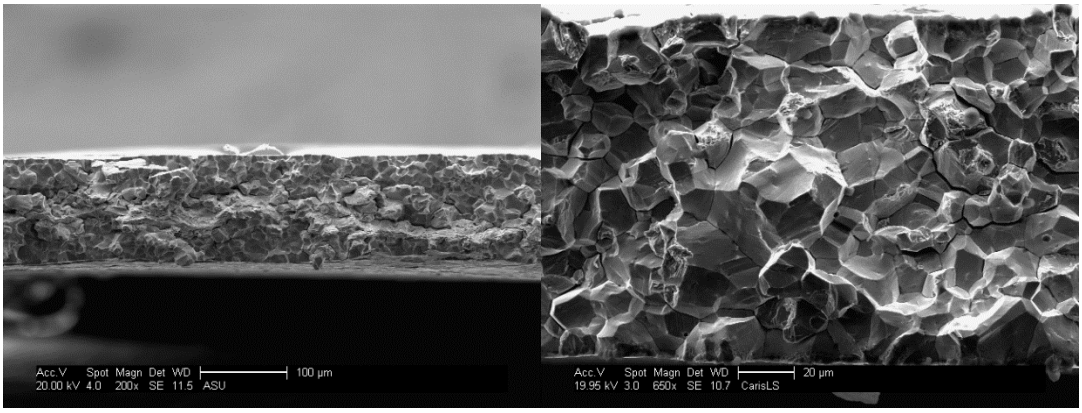

Figure 16: Fracture surface of the SCC test samples confirmed intergranular SCC

TEM analysis of cracked samples:

Figure 17 shows a typical cross-section of a crack (sample 1) that is chosen for lifting-out a thin section around the crack to obtain the TEM sample, whereas Figure 18 shows the final TEM sample obtained from the sample 2 along with the conventions used to report the EDS results.

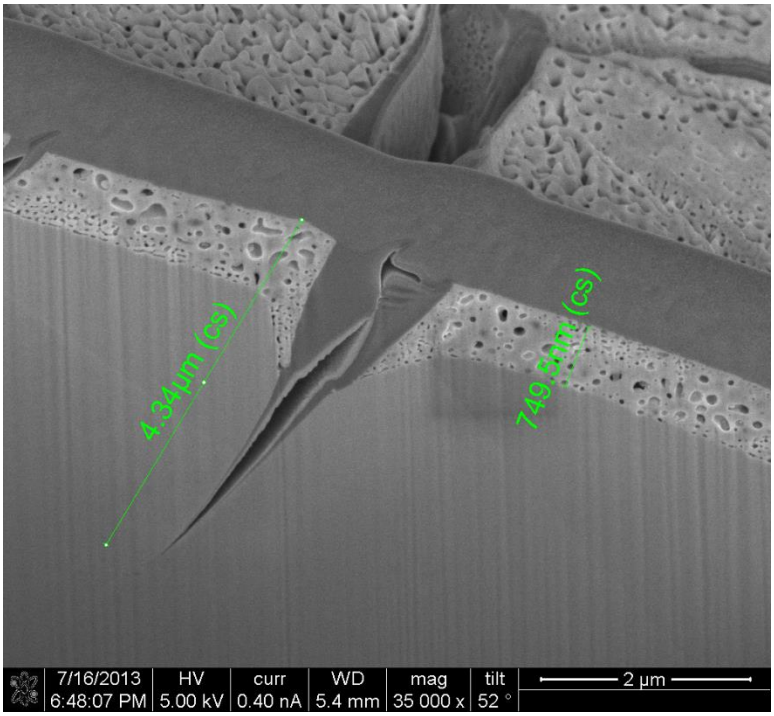

Figure 17: A TEM sample was prepared from a 4 um deep crack from sample 1 using lift-out technique in the FIB. Crack length is ~ 5 times the bulk dealloyed later thickness and the visible dealloyed region along the grain boundary is ~ 1.5 um

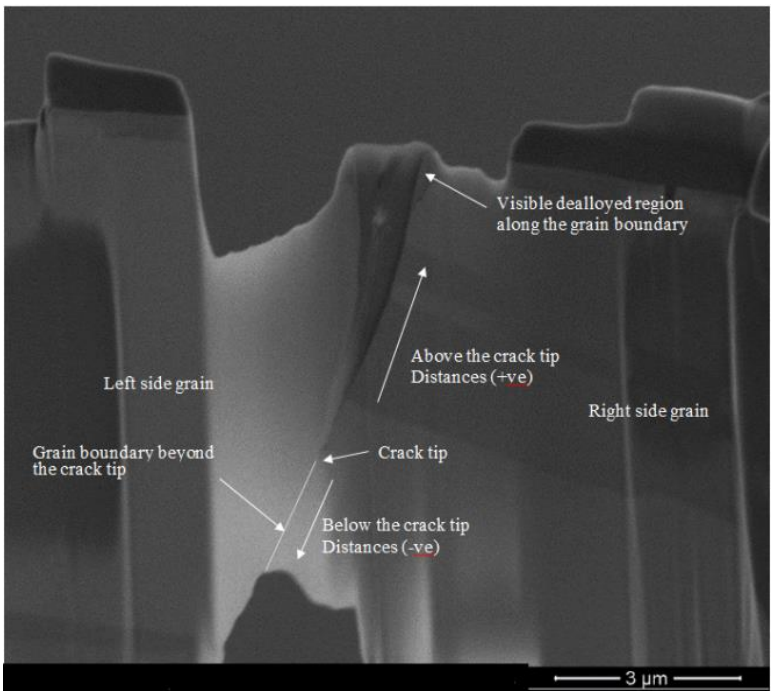

Figure 18: TEM sample prepared from a 6 um deep crack from sample # 2. The sample had ~ 450 nm deep bulk dealloyed layer. The conventions for distances marked on the image are used for both the TEM samples with cracks (sample 1 and 2) while presenting the EDS data.

For the sample 1, a cross-section in the FIB showed that the bulk dealloyed layer was ~ 750 nm deep and a sharp crack that went ~ 4 um deep from the surface (Figure 17). This crack was used to mill out a TEM sample from, using the FIB lift out technique. 0.7 nm probe size was used to do EDS analysis on the sample in JEOL 2010F scanning transmission electron microscope (STEM). All data points were taken with 2 seconds exposure time per point at 200 keV. The sample 2 had ~ 450 nm deep bulk dealloyed layer thickness. A region around a 6 um deep grain boundary crack was used to cut a TEM sample using Quanta 3D FEG FIB in PNNL (Figure 18). The EDS line scanning and STEM imaging were performed on the sample in the aberration corrected scanning TEM (Jeol ARM 200) at 80 keV (probe size 0.15 nm, 0.5 s per point for EDS) and 120 keV, respectively.

High angle annular dark field (HAADF) image (Figure 19) showed porosity in the sample below the crack tip. The EDS line scans below the crack tip along the grain boundary showed ~ 40 – 50 % Au to depth of 2 um below the crack tip i.e. 8 um below the surface (Figure 20).

However, the porosity extended to only ~ 300 nm below the crack i.e. to the depth of ~ 6.3 um from the surface.

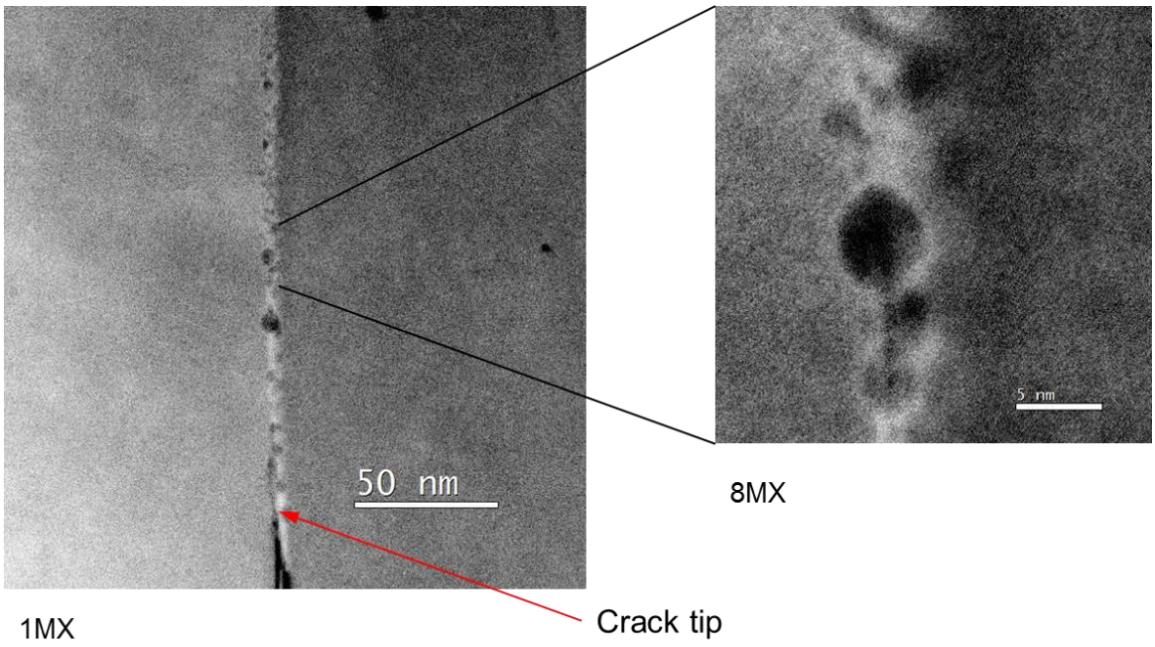

Figure 19: High angle annular dark field image at the crack tip of the sample 2 showed porosity along the grain boundary below the crack tip. This porosity extended to ~ 300 nm below the crack tip.

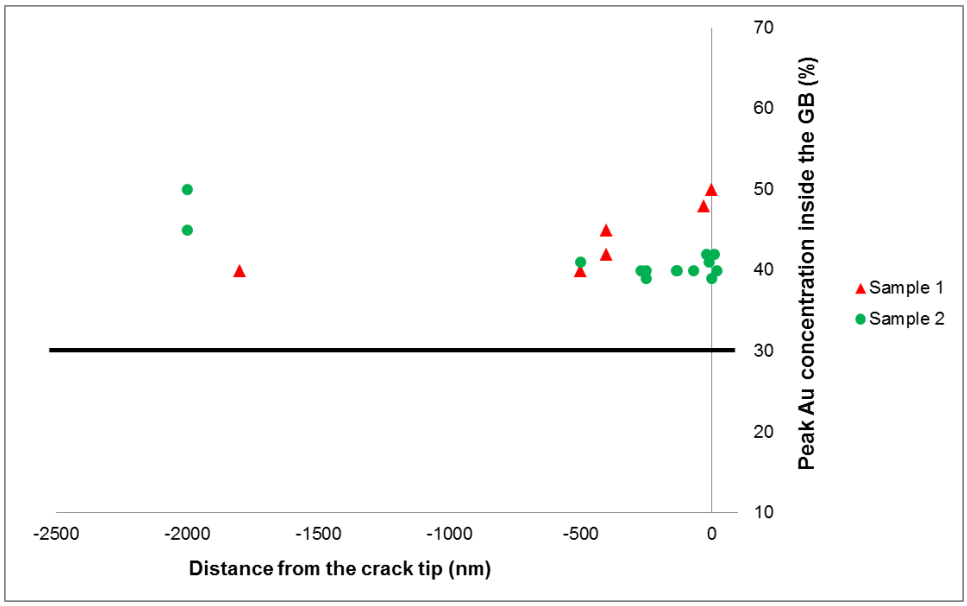

Figure 20: Peak Au concentration inside the grain boundary below the crack tip for the sample 1 and 2. The black line represents the bulk Au composition.

The sample 1 had higher Au composition inside the grain boundary than the bulk which decreased from 50% at the crack tip to ~ 40% at 1800 nm below the crack tip. However, the sample 2 showed different trend in the Au composition inside the grain boundary below the crack tip. The peak Au composition remained ~ 39 – 42% from crack tip to ~ 500 nm below the crack tip. However, couple of line scans along the GB at ~ 2 um below the crack tip had Au compositions ~ 45 – 50%. The Au composition along the crack above the crack tip cannot be determined due to presence of Pt inside the crack as discussed earlier.

If we assume that the increased Au composition is due to a dealloying process, the width of the region along the line scan with increased Au concentration along the grain boundary (W_{Au}) should have decreasing trend below the crack tip. The measured values of this width for the sample 2 are concurrent to this assumption as seen in the Figure 21. This analysis could not be performed on the sample 1 due to lack of sufficient data across the grain boundary.

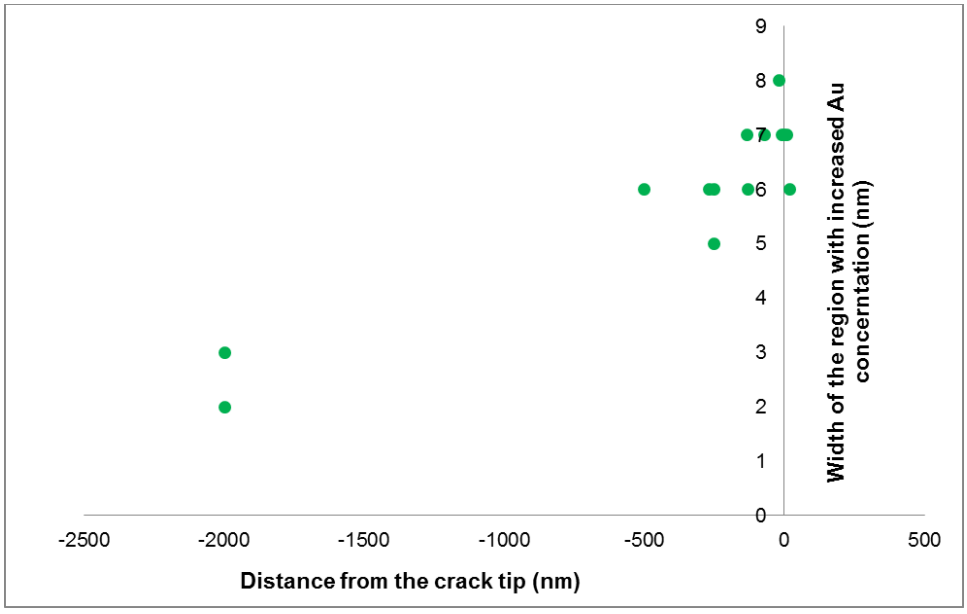

Figure 21: Thickness of the region with increased Au concentration along the GB decreases below the crack tip for the sample 2.

While analyzing the EDS data, the beam broadening in the TEM must be considered. The size of the beam broadening in the TEM for thin samples based on single scattering model [115] is given by

$$b = 8 \times 10^{-12} \cdot \frac{Z}{E_0} \cdot (N_v)^{\frac{1}{2}} \cdot t^{\frac{3}{2}} \quad (40)$$

Where b is the size of the beam in m, Z is the atomic number, E_0 is the beam energy in keV, N_v is the number of atoms/m^3 and t is the thickness of the sample in m. The thickness of this wedge shaped sample was measured using EELS technique [115]. It was ~ 100 nm near the top of the sample and ~ 15 nm near the bottom edge of the sample i.e. 2 um below the crack tip. The sample thickness near the crack tip was ~ 40 nm. For the AgAu alloy sample with given imaging conditions, the calculated value for the beam broadening is ~ 5.5 nm near the crack tip and ~ 1.3 nm near the bottom edge of the sample. Typical grain boundary width in the sample is ~ 1 nm. This means that the Ag-Au composition calculated through EDS at the center of the sample has effect of bulk composition. The Au composition calculated from EDS line scan across the GB just below the crack tip was ~ 40%. However, actual composition should be larger than 40% considering that we are averaging over the 5.5 nm wide beam region of which only 1 nm is the GB. The Au composition measured ~ 2 um below the crack tip near edge of the sample where sample thickness is ~ 15 nm was also ~ 40%. Considering only 1.3 nm beam spreading, the actual Au composition should be much closer to the calculated 40%. Hence it is possible that the Au composition decreases inside the grain boundary from the crack tip to the farthest point of ~ 2 um below the crack tip. However, to determine the exact composition, information about exact width and shape of the Au composition profile along the line scan should be available. This can be used to deconvolute the beam shape from the EDS scan profile [123]. In the case of sample 1, this method may give even steeper decrease in the Au composition below the crack tip.

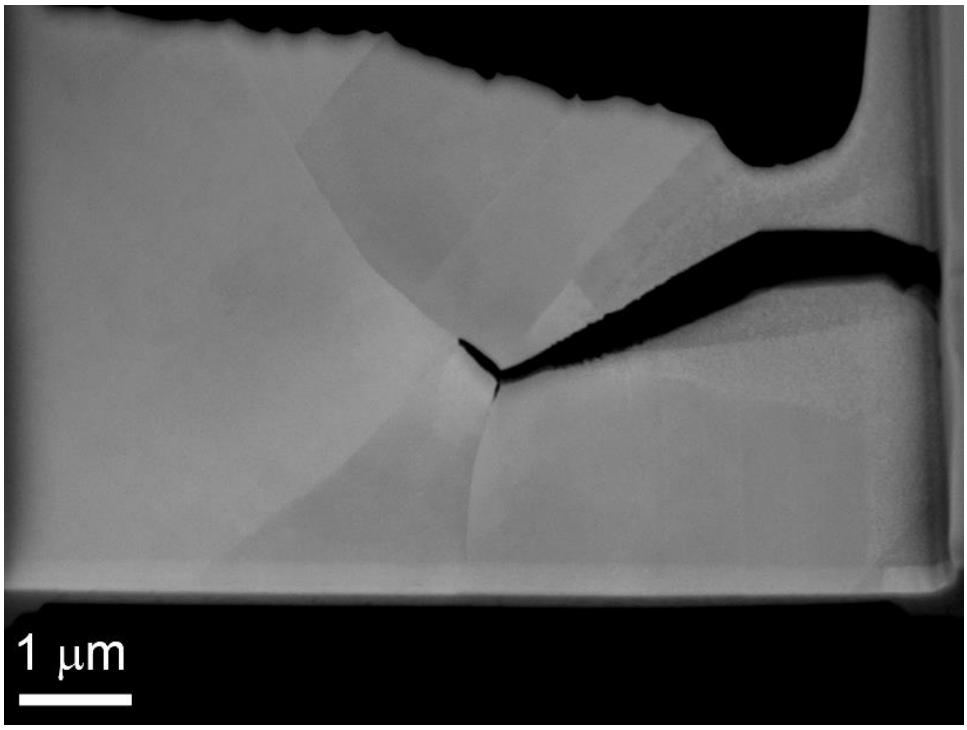

Figure 22: SEM image of the TEM sample milled from the sample 6 from the deepest crack found in the mechanical cross-section. The crack was ~ 4.5 um deep with 750 nm deep bulk dealloyed layer. The crack branched at the grain boundary triple point. Most of the TEM analysis was performed on the top part of the branched crack.

The composition for the sample 6 was $Ag_{80}Au_{20}$. This sample was dealloyed in 1M $HClO_4$ at 1.215 V (~ 45 mA/cm^2) vs SHE for 15 s to get ~ 750 nm thick bulk dealloyed layer. The sample was immersed in water for 10 s after dealloying and bent immediately. This sample was then mounted in epoxy and mechanically cross-sectioned. Largest crack observed (~ 4.5 um) in the cross-section was used to get a TEM sample (Figure 22). The crack had branched along two different grain boundaries at a grain boundary triple point. The TEM sample was imaged in aberration corrected TEM Jeol ARM-200.

This sample did not show any porosity along the GB below the crack tip as seen in the Figure 23 (a). However, EDS line scan ~ 5 nm below the crack tip (Figure 23 (b)) showed increase in the Au composition inside the GB below the crack tip.

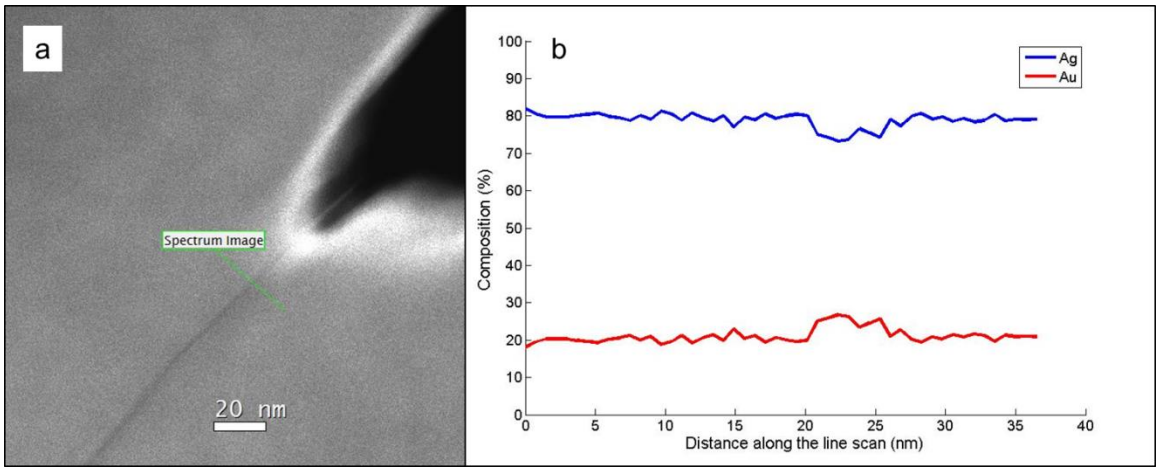

Figure 23: (a) Sample 6 did not show any hint of porosity below the crack tip at 1MX magnification. (b) However, the EDS scan showed Au composition increase to 27% inside the grain boundary and the width of the region with the higher Au concentration was ~ 6 – 7 nm. Again considering the beam broadening effect, actual composition of Au could be even higher.

The control samples:

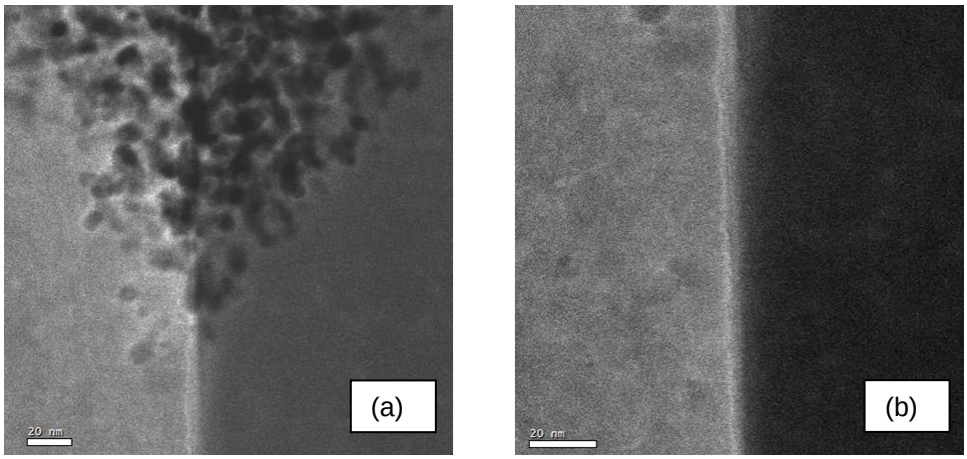

Figure 24: (a) 1 MX magnification HAADF image just at the end of the V along the grain boundary (b) 1.5 MX magnification HAADF image ~ 50 nm below the V along the grain boundary for Sample 10 showed no grain boundary porosity beyond ~ 780 nm below the surface.

The bulk dealloyed layer thickness in the sample 10 (1 mA/cm^2 for 180 s unbent) was ~ 450 nm and the V shape along the GB extended to ~ 780 nm below the surface. There was no hint of porosity along the grain boundary below the end of the V to ~ 8 um below the surface i.e. bottom edge of the TEM sample (Figure 24).

Similar result was observed for the sample 9 (6 mA/cm^2 for 60 s unbent). This sample had ~ 470 nm thick dealloyed layer. There was no hint of porosity below the end of the V which was 620 nm below the surface (Figure 25). However, ~ 6 um below the surface, there was some

porosity inside the GB which extended for ~ 100 nm (Figure 26). EDS line scan along this region did not show any hint of increase in the Au concentration inside the GB.

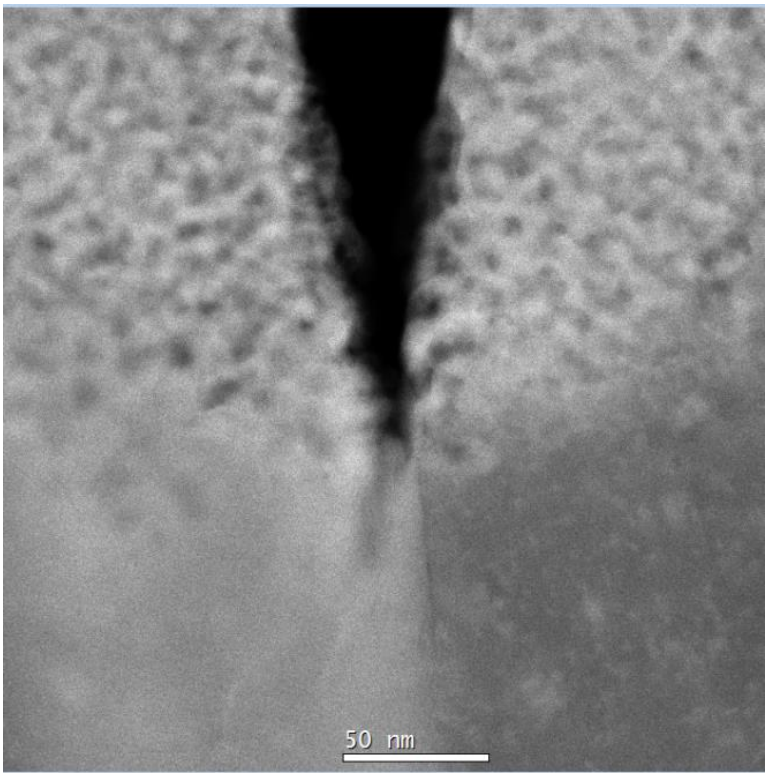

Figure 25: Sample 9 showed no porosity beyond the visible V along the grain boundary which extended to only ~ 620 nm below the surface. The high current density (6 mA/cm^2) causes the porous layer to crack due to quick volume change.

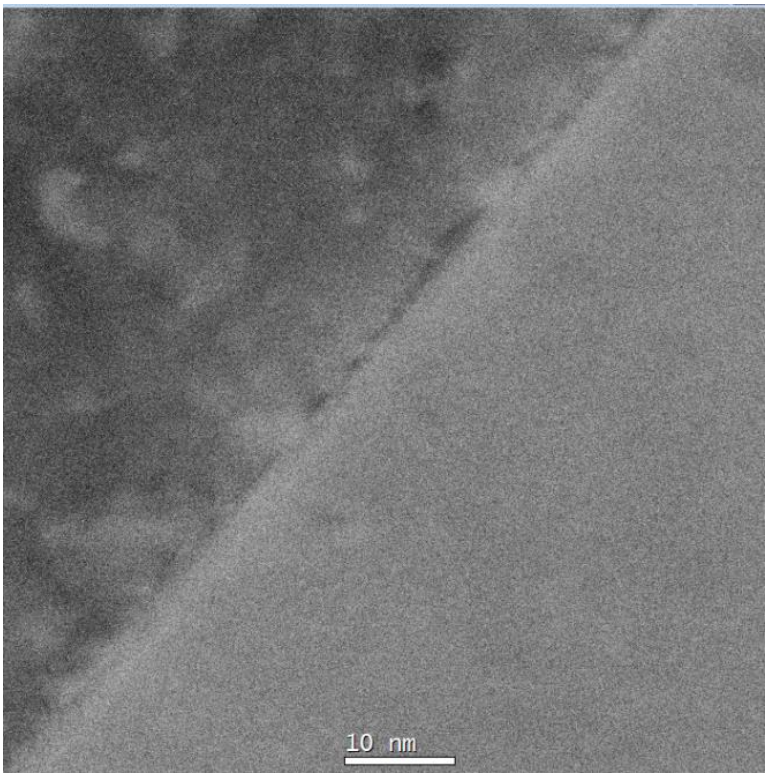

Figure 26: Sample 9 showed porosity inside the grain boundary ~ 6 um below the surface. However, EDS along the grain boundary in this region did not show any increase in the Au composition inside the grain boundary unlike sample 2 which was dealloyed with the same protocol and was bent.

A TEM sample prepared from sample 11 (un-corroded) consisted of 7 different grain boundaries which were analyzed in the aberration corrected TEM (ARM 200F). This sample did not show any defects along the grain boundary unlike the defects sample 9 showed at ~ 6 um below the surface. The EDS line scans also showed that the compositions in all the grain boundaries were same as the bulk ($Ag_{70}Au_{30}$). This can be attributed to the limited number of grain boundaries that were analyzed. Although all the samples were cut from the same sheet of the Ag-Au alloy, there could still be variations from one grain boundary to the other which can depend on the orientations of the adjacent grains, and local/random fluctuations.

Atom probe tomography analysis:

Two control samples from the $Ag_{70}Au_{30}$ sheet were studied in an atom probe tomography. Sample 10 (1 mA/cm^2 for 180 s) had ~ 350 nm bulk dealloyed layer thickness and the V along the grain boundary extended to ~ 600 nm below the surface. Two different APT samples were obtained from this sample along the grain boundary below the SEM visible V along the grain boundary. Both these samples showed increase in the Au composition inside the GB as compared to the bulk composition. If we had to attribute this increase in the Au concentration to dealloying, the point near the surface of the sample should have higher Au composition than the point below it. However, the first APT sample which was obtained from ~ 650 nm below the surface (i.e. ~ 50 nm below the V) showed ~ 3% increase in the Au concentration inside the grain boundary, whereas the second APT sample that was obtained from ~ 1700 nm below the surface (i.e. ~ 1100 nm below the end of the V) showed ~ 6% increase in the Au concentration along the grain boundary as shown in the Figure 27.

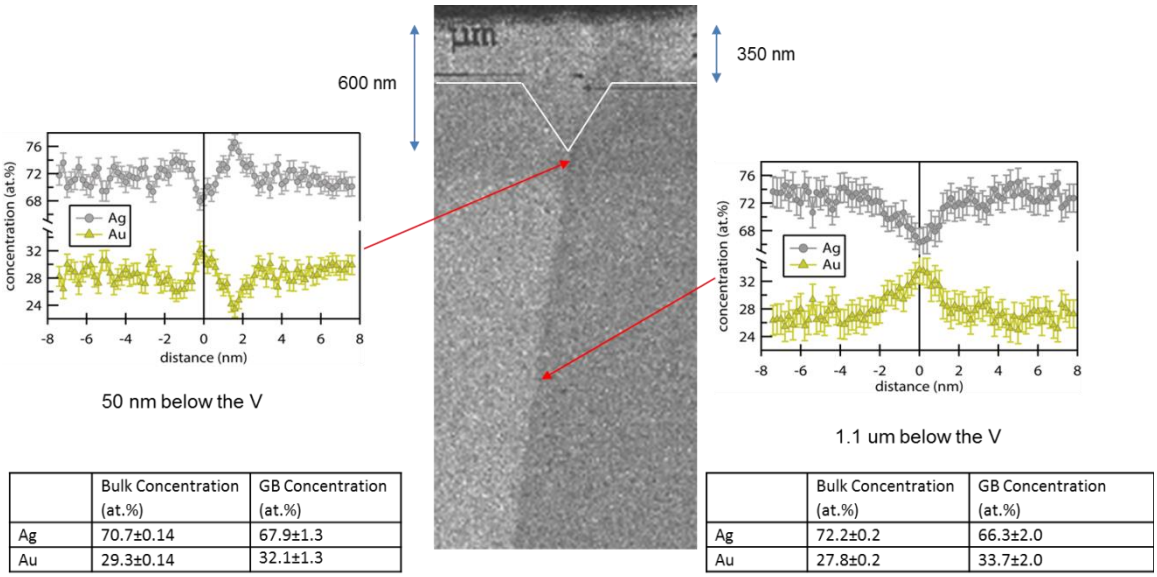

	Bulk Concentration (at.%)	GB Concentration (at.%)
Ag	70.7±0.14	67.9±1.3
Au	29.3±0.14	32.1±1.3

	Bulk Concentration (at.%)	GB Concentration (at.%)
Ag	72.2±0.2	66.3±2.0
Au	27.8±0.2	33.7±2.0

Figure 27: APT analysis of grain boundary in a corroded sample (# 10) at different locations below the visible dealloyed region along the grain boundary showed that Au composition inside the grain boundary increases by 3 – 6 %.

Two more APT samples were prepared from an un-corroded sheet (sample 11). The APT analysis report is shown in the Figure 28. It showed that the composition in the grain boundary was same as the bulk composition which is $Ag_{70}Au_{30}$.

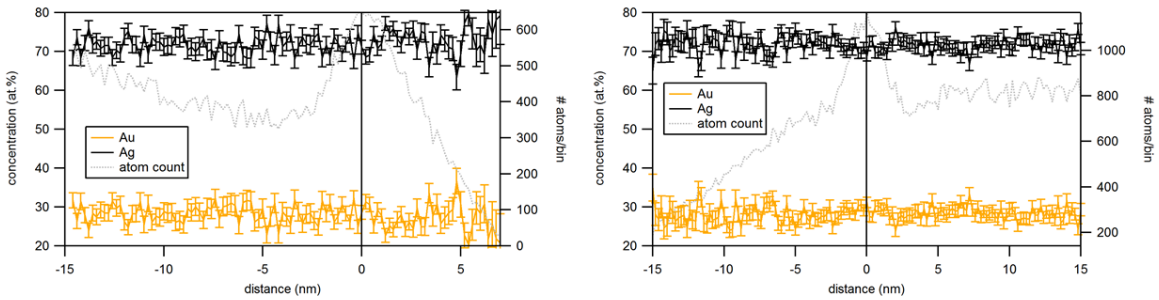

Figure 28: Compositional analysis of a grain boundary in an un-corroded sample (# 11) using APT shows no segregation of either Ag or Au along the grain boundary. The black vertical line represents grain boundary location. The dotted faint line gives atom count which was high in the grain boundary as it is easier to dislodge the grain boundary atoms than the atoms inside the grains.

Crack Injection experiments after immersing in water and LN_2:

The samples dipped in water for 1 hour after dealloying had cracks going little past the SEM visible GB dealloyed depth (Figure 29). This can be attributed to the coarsening of the ligaments in water over time after the dealloying.

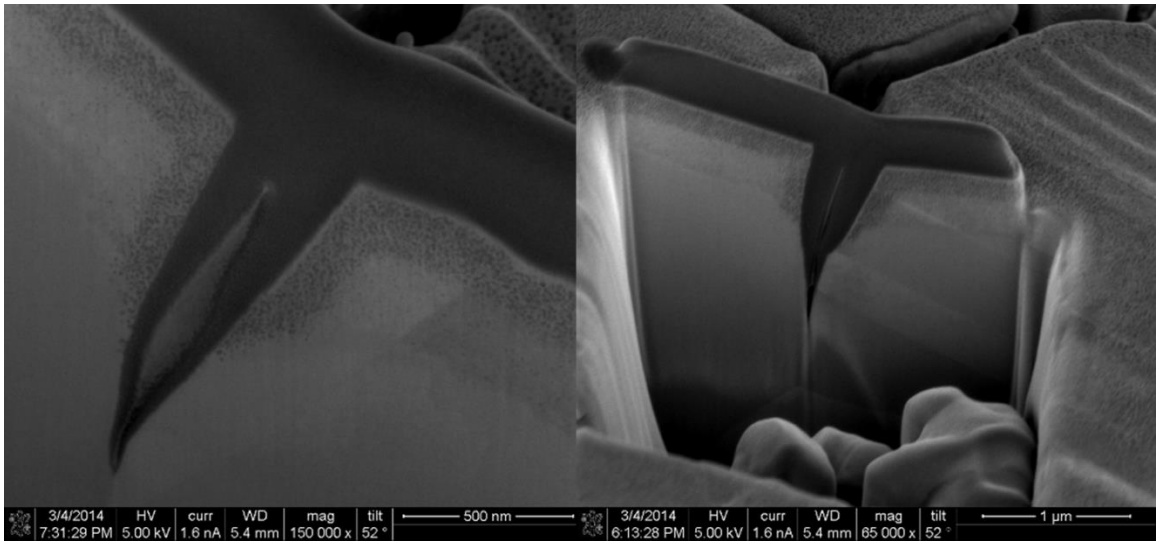

Figure 29: Samples that were immersed in water for 1 - 2 hours after dealloying prior to bending showed much shallower cracks.

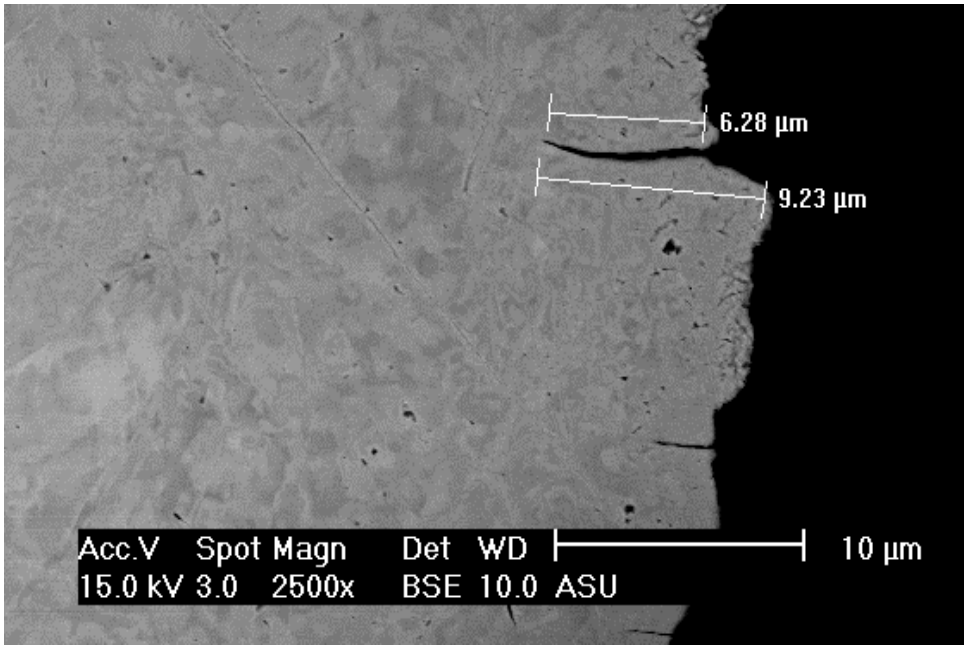

Figure 30: Mechanical cross-section of the Sample 3 (dealloyed at ~ 1 mA/cm^2 in 1M $HClO_4$ for 180 s) had largest crack ~ 7 – 9 um deep. The expected dealloyed layer thickness for this sample is 450 – 500 nm.

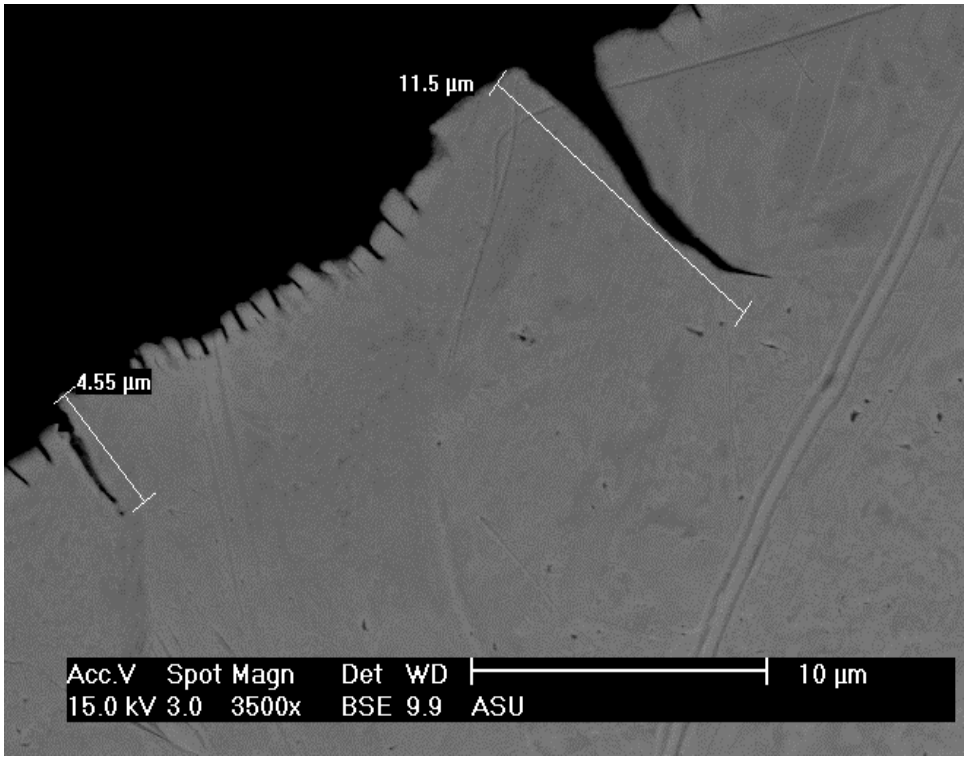

Figure 31: Mechanical cross-section of the Sample 4 (dealloyed at ~ 10 mA/cm^2 in 1M $HClO_4$ for 30 s) had largest crack ~ 11.5 um deep. The expected dealloyed layer thickness for this sample is ~ 500 – 700 nm.

Sample 3 (Figure 30) and 4 (Figure 31) – dealloyed at 1 and 10 mA/cm^2 respectively – were also mechanically cross-sectioned and polished. Both of these samples showed sharp intergranular cracks ~ 15 – 20 times deeper than the bulk dealloyed layer thickness.

The sample 5 was dealloyed at ~ 6 mA/cm^2 in 1M $HClO_4$ and dipped in LN_2 for 1 hour before bending. This sample had ~ 300-500 nm deep bulk dealloyed layer. Two FIB – milled cracks (a) and (b) were ~ 8 and 10 um deep whereas deepest crack found in the mechanically cross-sectioned surface was ~ 6.7 um deep (Figure 32). These cracks are ~ 13 – 30 times deeper than the bulk dealloyed layer thickness.

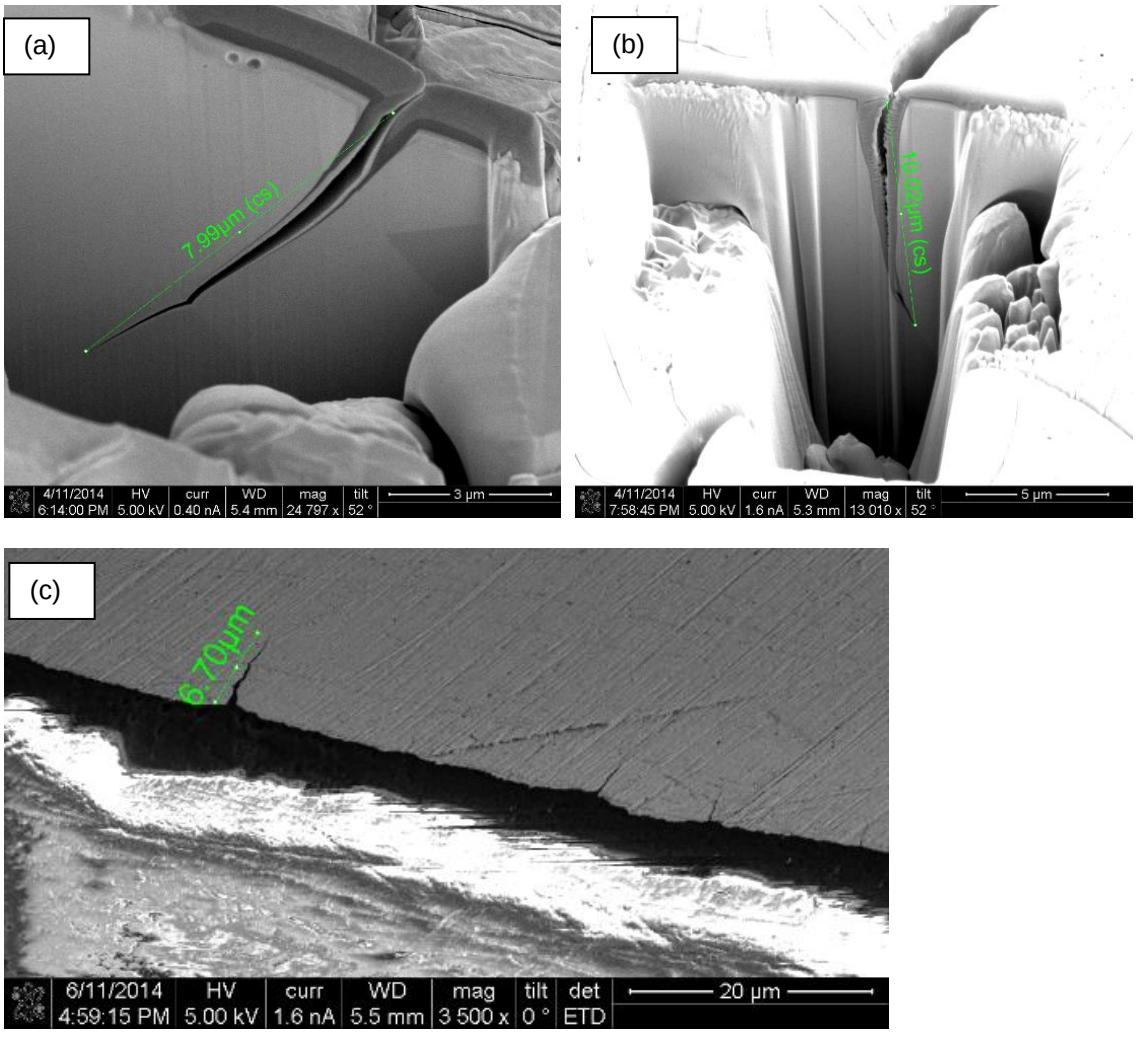

Figure 32: The sample 5 had ~ 300-500 nm deep bulk dealloyed layer. Two FIB milled cracks (a) and (b) were ~ 8 and 10 um deep whereas deepest crack found in the mechanically cross-sectioned surface was ~ 6.7 um deep.

3.2 Mechanical Properties and Dynamic Fracture Results:

Tensile tests:

The tensile test images were analyzed using ARAMIS to obtain strain on the sample surface as a function of the stress value. The loading direction was assumed to be X axis. Average strain values in X and Y direction (ε_x and ε_y) on the sample surface were obtained from ARAMIS along with the standard deviations. The stress – strain curves for all of the NPG samples provided similar values of the Young's moduli for loading and unloading (Figure 33). Figure 34 shows the stress – strain curve for all NPG samples that were loaded to fracture. The Poisson's ratio of the NPG was obtained from the strain values in X and Y direction (Figure 35).

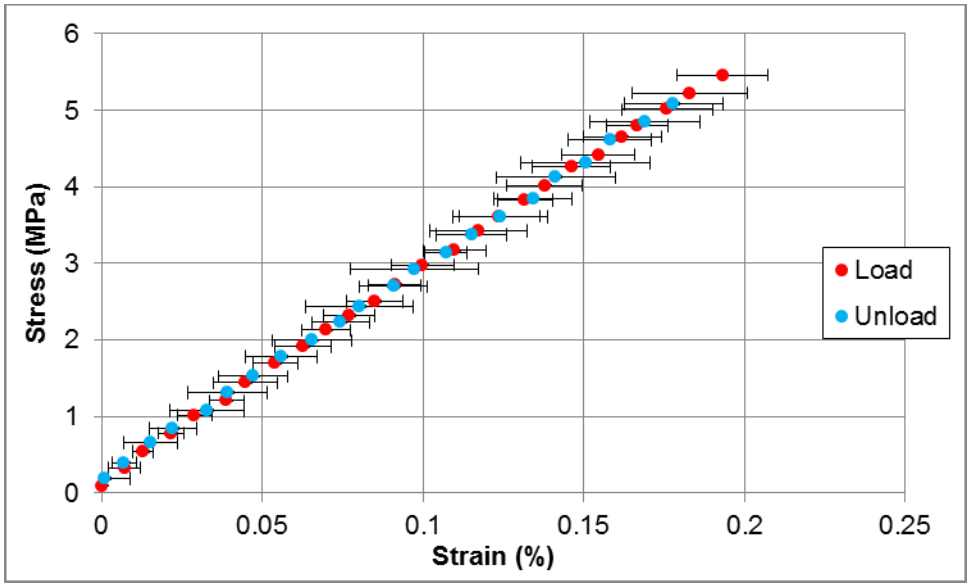

Figure 33: A representative load – unload curve (sample T2). There wasn't significant difference in the Young's modulus values obtained from the loading part and the unloading part of the curve. The error bars on strain values represent the standard deviation in the strain values obtained from typically 500 – 1000 data poitns from the sample surface. The maximum error in the load cell data was ~ 0.01 lb which corresponds to a stress value of ~ 0.12 MPa. These error bars are present but not visible.

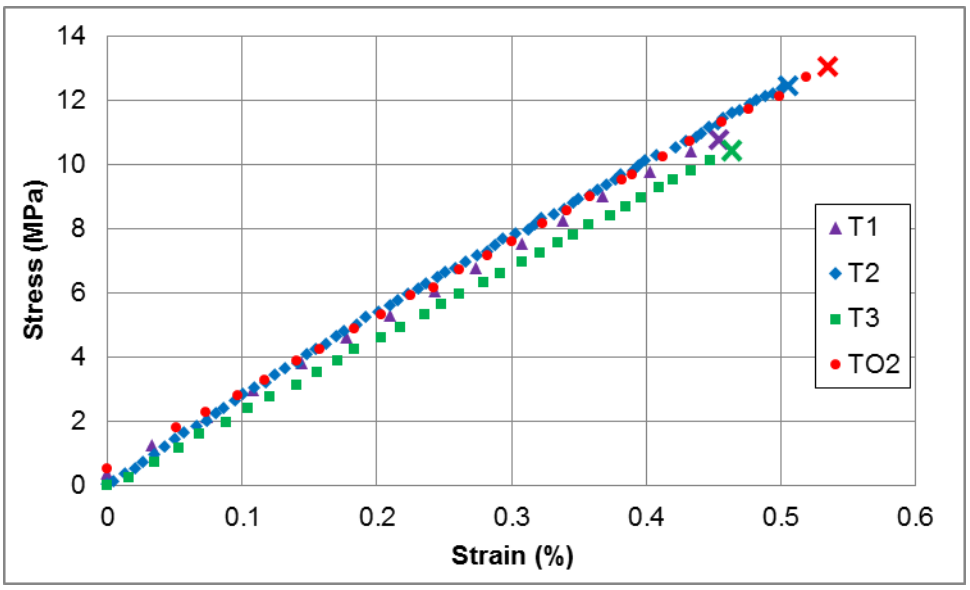

Figure 34: Stress - Strain curves for the NPG samples to fracture. The sample TO2 is oxidized NPG sample.

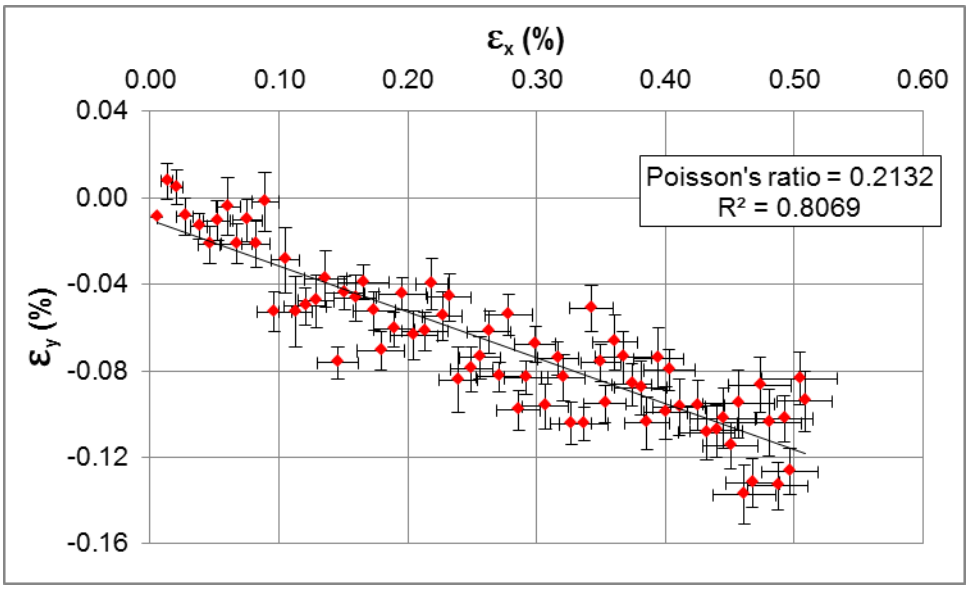

Figure 35: The slope of the straight line fit to ε_y – ε_x for sample T2 gives Poisson's ratio of ~ 0.2132. The error bars represent standard deviations in the strain values obtained from ~ 500 – 1000 points from the sample surface.

Table 5: Mechanical properties of NPG (The O denotes the oxidized samples)

Sample (Total number of tests)	Young modulus (E) (GPa)	Poisson's ratio (v)	Fracture stress (σ_f) (MPa)
T1 (9)	2.39 (0.08)	0.1801 (0.0429)	10.79
T2 (5)	2.78 (0.05)	0.2132 (0*)	12.35
T3 (5)	2.37 (0.10)	0.1878 (0*)	10.64
TO1 (4)	2.35 (0.09)	0.2573 (0*)	X**
TO2 (3)	2.35 (0.04)	0.2391 (0*)	13.08
TO3 (3)	2.60 (0.05)	0.2322 (0*)	X**

* Only one test had acceptable linear fit i.e. $R^2 > 0.65$.
** These samples broke after few load – unload tests due to handling / glue issues and hence could not be loaded to fracture to obtain the fracture stress. The samples TO1 and TO3 were loaded to maximum stress of 6.23 MPa and 8.78 MPa respectively without any hint of yielding.

Table 5 summarizes all results for the tensile tests. The average values of the Young's moduli for non-oxidized NPG and oxidized NPG were very similar (2.51 ± 0.20 GPa and 2.44 ± 0.15 GPa respectively). The Poisson's ratio, however, showed some difference in for the non-oxidized and oxidized samples (0.1896 ± 0.0350 and 0.2429 ± 0.0130). Average fracture stress for the NPG sample was 11.26 MPa.

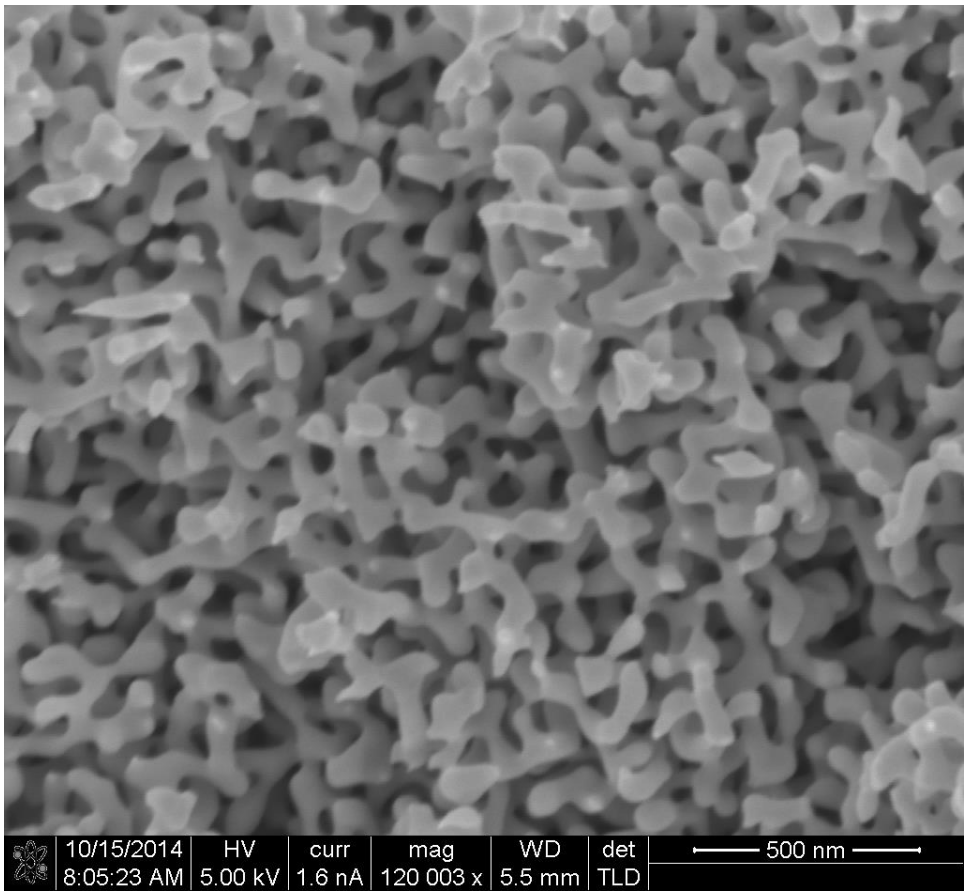

Figure 36: Fracture surface of a tensile NPG sample shows necking of individual ligaments

Even though the fracture surface (Figure 36) shows plastically deformed Au ligaments, the macroscopic failure of the NPG is brittle. Let us assume a simple log normal distribution in ligament diameters distribution in the NPG sample. For Au ligaments, the fracture load increases with increase in the ligament diameter. When such sample is subjected to tensile loading, the weakest ligament undergoes failure at first. This broken ligament then generates a crack in the sample. Duxbury [124] studied the strength of such dilute networks. He estimated stress intensity (σ_{tip}) generated by such a crack of size "a" as,

$$\frac{\sigma_{tip}}{\sigma_0} \sim 1 + ka^{1/2} \qquad 41$$

Here σ_0 is the applied stress and k is an unknown constant. Now if the disorder in the system is weak, i.e., the width of the ligament size distribution is small so that the stress field produced by this crack is larger than the strength of the ligaments, a single crack grows and sample failure is

extremely brittle. The microscopically ductile ligament failure will be confined to a single plane of ligaments. However the ligament size distribution is wide, distributed single ligament fractures would occur throughout the volume of the solid. If the disorder is large the fracture process will be uncorrelated and sample failure will be macroscopically ductile. The situation for our 30 – 50 nm NPG lies close to the weak disorder limit where we see macroscopic brittle behavior with ductile ligaments failure on the fracture surface.

Crack tip opening displacement (CTOD) test:

Pixel size for all the CTOD and DIC displacement resolution tests was ~ 1 um. For the displacement resolution test, the actual average displacements for 0.1 um, 0.2 um, 0.5 um and 1.0 um tests were 0.06 um, 0.14 um, 0.43 um and 0.95 um. The motorized stage has minimum repeatable movement of 0.8 um whereas the built in encoder can measure displacement with resolution of 29 nm [125]. However, the software used to control the stage provided displacement with resolution of 0.1 um. Hence the error in the actual measured displacement from the stage was fixed at ± 0.05 um. This error is very close to the actual average displacement for the “0.1 um” test. Hence that test was concluded invalid. For all of the other tests, the standard deviation obtained from displacement values from ~ 10000 points on the sample surface was ~ 0.06 um. Two of these tests are shown in the Figure 37.

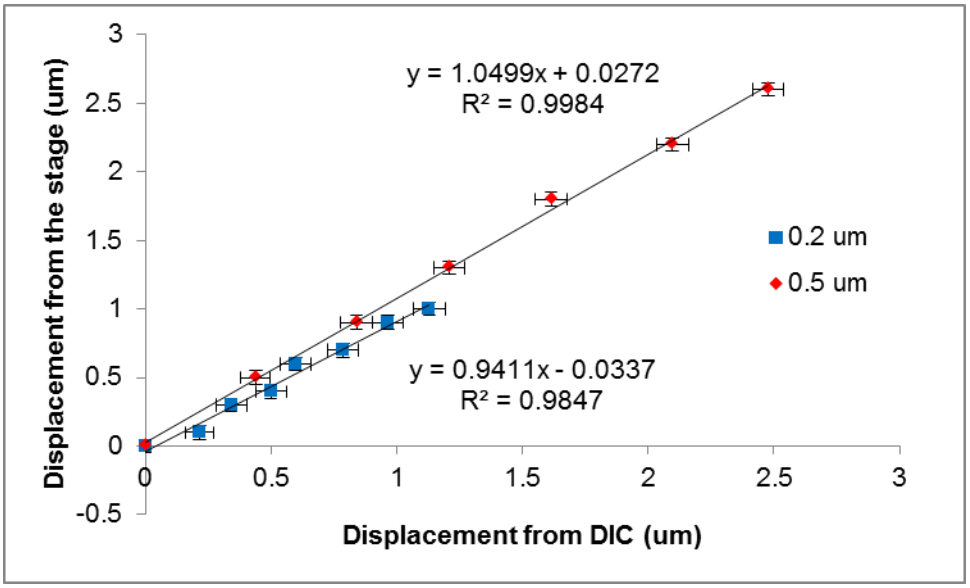

Figure 37: The displacement resolution tests showed ~ 5 – 6 % misfit (in ideal case the slopes should be 1). Actual average displacement for the "0.2 um" and the "0.5 um" tests were 0.14 um and 0.43 um respectively.

The images obtained for the CTOD test were analyzed using ARAMIS to get displacement field on the sample surface. The difference of the displacement values at the notch tip was measured as shown in the Figure 38. The load values for different images were used to calculate the stress intensity values using Equation 36. Then, from Equation 39, slope of the curve $\frac{4K_I^2}{\pi E}$ vs δ gave the yield stress (Figure 39).

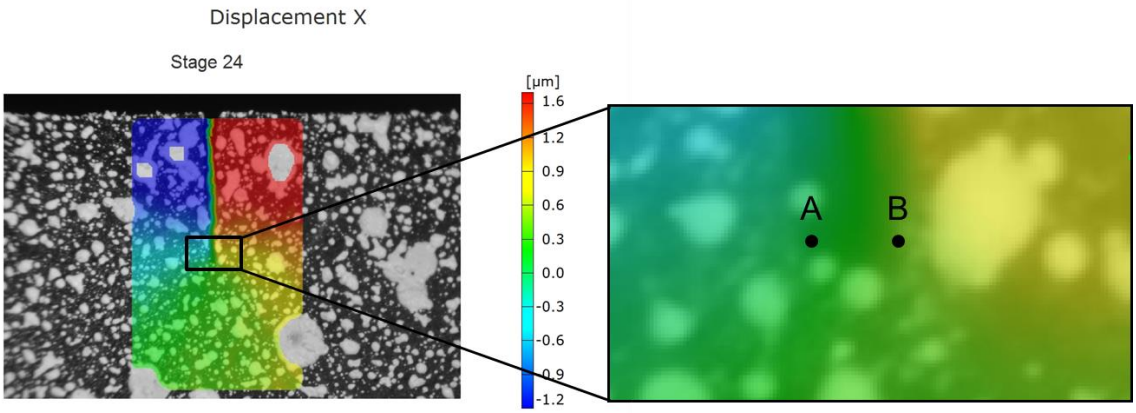

Figure 38: Displacement values at point A and B (at the notch tip) were measured from the displacement field calculated using DIC software (ARAMIS). These two displacement values were used to calculate the CTOD (δ) value for the corresponding load value measured from the load cell.

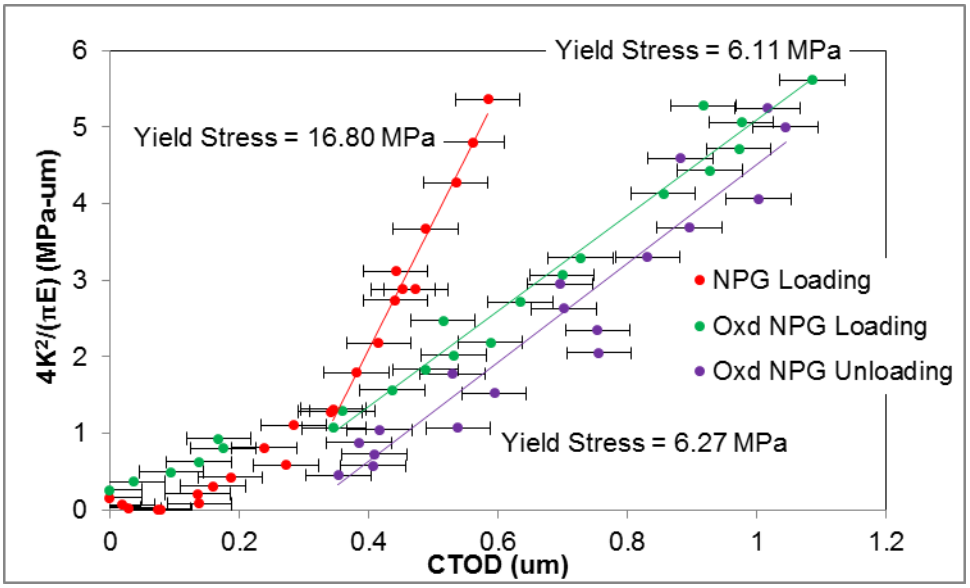

Figure 39: The CTOD tests showed that the yield stress obtained for the monolithic NPG sample was 16.80 MPa whereas that for the oxidized sample was ~ 6.20 MPa.

Both of the curves were linear beyond CTOD value ~ 0.3 um. This linear region was used to obtain the yield stress of the sample. The yield stress for the NPG sample was 16.80 MPa. However, the oxidized sample showed much lower yield stress (~ 6.20 MPa) than the fracture stress of the oxidized NPG sample (13.08 MPa). This apparent lower yield stress can be attributed to the curvature observed in the oxidized samples. All of the oxidized samples had a visible curvature which occurred due to possible non-uniform oxidation of the sample. The samples were placed on a gold thin film on mica and immersed in the electrolyte to oxidize. This caused one surface of the sample being directly exposed to the electrolyte whereas the other surface came in contact with the electrolyte only when the electrolyte penetrated through the pores of the NPG. This could result in non-uniform oxidation of the sample. As reported by McCann [126] nanoindentation tests on Au and Au-oxide surfaces showed that the yield stress of Au-oxide is larger than the Au. Jin and Weissmuller [11] also observed higher flow stress in the oxidized NPG than the non-oxidized NPG in compression tests. This difference in the yielding along with non-uniform oxidation can result in the curvature. While gluing the sample on the mechanical testing device, the samples were not sitting flat on the grips. However during the tensile loading, the samples got straightened. This can cause apparent increase in the measured CTOD values for the oxidized samples which would result in lower yield stress. Also another

possible reason is cracks present near the notch of the sample. The NPG is extremely brittle and it is easily possible to cause cracks in the sample during handling. This can also lead to lower σ_y.

Critical stress intensity factor / Fracture toughness:

The load-displacement curves for fracture toughness tests are shown in the Figure 40. The critical stress intensity factor (K_{IC}) was calculated from Equation 36 and the fracture load. The average values for the K_{IC} for non-oxidized and oxidized samples were 0.165 ± 0.033 MPa-$m^{1/2}$ and 0.147 ± 0.027 MPa-$m^{1/2}$. Although the oxidized samples showed more curvature that the non-oxidized NPG samples, not much difference was observed in the fracture toughness values for both of those. The fracture toughness values calculated using Equation 38 are 10.89 ± 3.36 J/m^2 and 8.85 ± 2.36 J/m^2 for non-oxidized and oxidized samples respectively.

The oxidized samples showed much larger compliance than non-oxidized samples. One would expect the oxidized samples to be stiffer based on the discussion earlier. This observed lower stiffness in the oxidized samples cannot be explained.

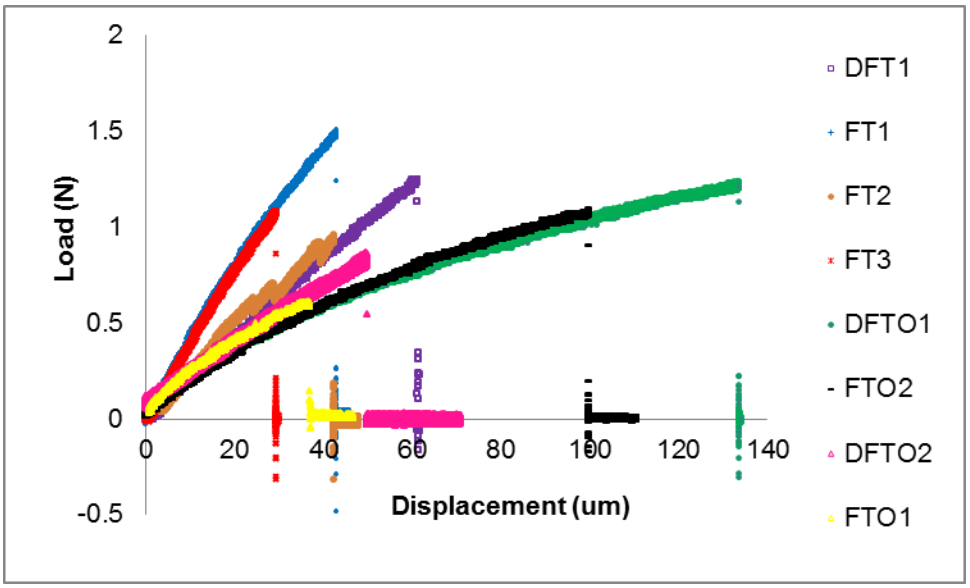

Figure 40: Load – Displacement data for the NPG samples. The D in the name represents a simultaneous dynamic fracture test and O stands for oxidized samples

The critical stress intensity value calculated by Briot et al. [67] in their tensile tests is 0.22 MPa-$m^{1/2}$ for a sharp crack with a note that a semicircular notch would lower this number by 20%

which is 0.176 MPa-$m^{1/2}$. Our observed value 0.165 ± 0.033 MPa-$m^{1/2}$ is in agreement with their results.

The maximum extent of the plastic zone for a notch (r_p) is well approximated by [122],

$$r_p = \frac{\pi K_{IC}^2}{8\sigma_y^2} \quad (42)$$

Using the critical stress intensity and yield stress values (from CTOD) for the NPG sample, the calculated size of this plastic zone is ~ 40 um. The samples has ligament size ~ 40 – 60 nm. Hence we can assume linear density of number of ligaments to be ~ 1 ligament per 100 nm. This gives us linear density of number of ligaments ~ 10^7 ligaments/m. Hence the volume density would be 10^{21} ligaments/m^3. If we assume that the width of the plastic zone for the CTOD NPG sample to be ~ 40 um (width of the notch), the volume of the plastic zone will be (40 um X 40 um X 125 um) ~ 2 X 10^{-13} m^3. This volume contains ~ 2 X 10^8 ligaments. Then the total number of ligaments in the tensile test samples (volume = 3 mm X 15 mm X 125 um) would be 7.5 X 10^{12}.

Duxbury and Leath [127] performed statistical analysis of strength of random array of fiber. They showed that for a fiber bundle with total L number of bond, the average strength scales as $\frac{1}{\ln L}$. If we apply this relation to the strength of the CTOD sample and the tensile sample, we get:

$$\frac{\sigma_{CTOD\ Sample}}{\sigma_{Tensile\ Sample}} = \frac{\ln\left(L_{Tensile\ Sample}\right)}{\ln\left(L_{CTOD\ plastic\ zone}\right)} = \frac{\ln(7.5 \times 10^{12})}{\ln(2 \times 10^{8})} = 1.55$$

$$\frac{\sigma_{CTOD\ Sample}}{\sigma_{Tensile\ Sample}} = \frac{16.80\ MPa}{11.26\ MPa} = 1.49$$

These numbers are in good agreement with each other. This reconfirms the conclusion that the number obtained for the yield stress value of the oxidized sample may have got affected by the curvature of the sample and possible cracks near the notch occurred during handling of the sample.

Dynamic fracture test:

The images obtained for the dynamic fracture tests from the high speed camera (Phantom V12.1) were analyzed using ARAMIS to obtain displacement and strain field on the

sample surface during the dynamic fracture. The displacement field and/or strain field on the sample surface can be used to obtain crack velocity during the fracture process (Figure 41). The displacement field and the strain field move as the crack progresses through the sample. The scale was adjusted so that region far from the crack contains little noise and no hot or cold spots. A suitable value was assumed as the threshold and crack tip was determined from the threshold value along the crack propagation path for all images.

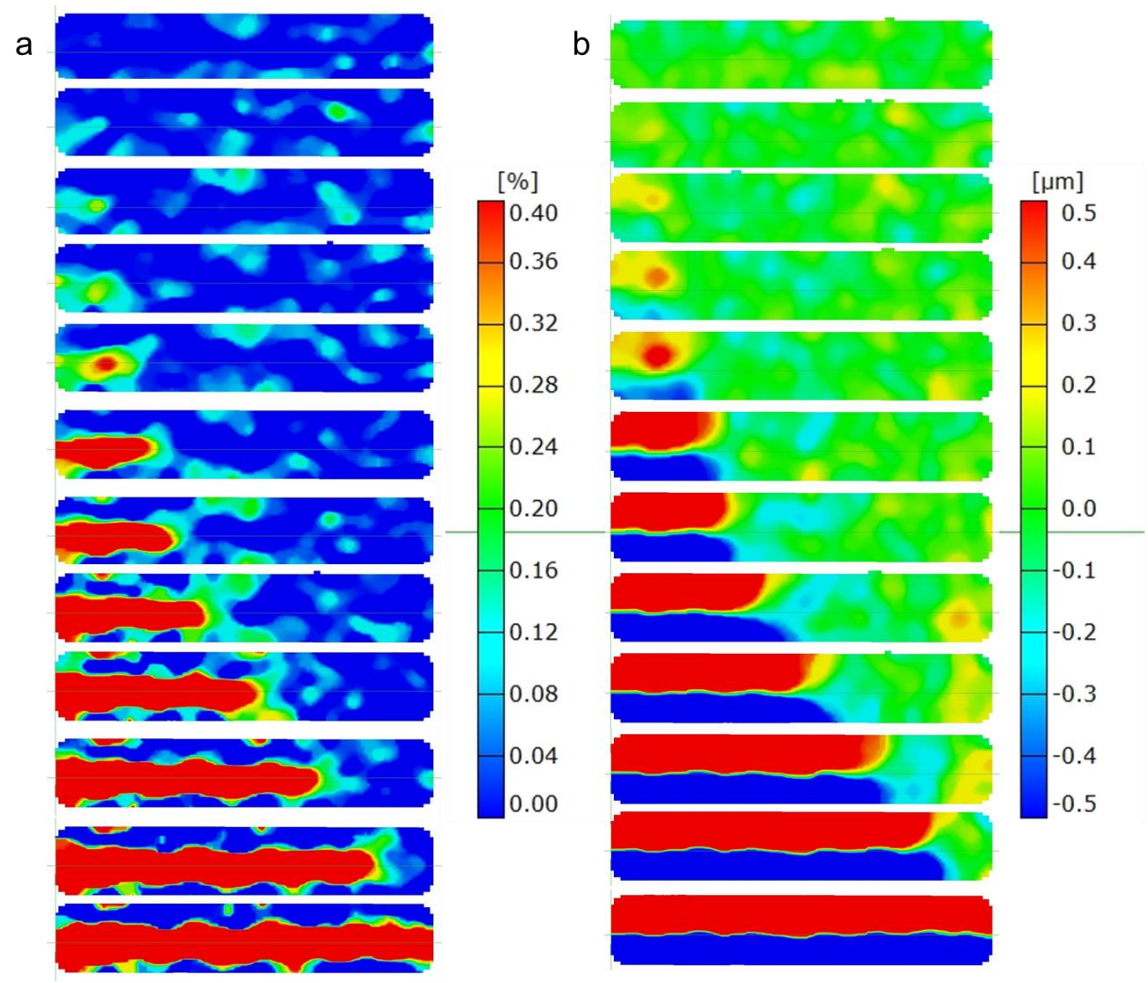

Figure 41: (a) Strain and (b) Displacement field on sample surface as the crack propagated though the monolithic NPG sample (DFT1). Crack tip location for this sample was determined from the tip of region where the strain exceeds 0.40%. The strain and displacements measured here are with respect to the image captured just before the fracture event occurred.

Strain in Y direction for all points along the crack was extracted from ARAMIS and analyzed using Matlab to obtain crack tip location and crack velocity (Appendix B). The crack velocities obtained for the NPG samples are shown in the Figure 42 as a function of the crack

length. The maximum crack velocity obtained for a non-oxidized sample is ~ 185 m/s. Any micro-cracks in the sample can affect stiffness of the sample resulting in lower crack velocity. Also the initial crack velocity depends on the instantaneous stress intensity. If the loading rate is low, the crack velocity will slowly increase from 0 [91]. Any shear waves produced from the crack tip perpendicular to the crack propagation direction will reflect back from the boundaries and limit the crack velocity to a lower value. The calculated shear wave velocity for the NPG sample using Equation 18 is ~440 m/s and the Rayleigh wave velocity from Equation 17 is 399 m/s. These numbers are in agreement with the velocities measured by Ahn and Balogun [74] using laser ultrasonic measurements. The distance between the notch and the glue is ~ 4 – 5 mm. If we assume that the shear wave emitted from the moving crack tip reflects from the point where it is glued, we can say that it travels ~ 8 – 10 mm before affecting the crack velocity. At the shear wave speed, it would take the wave ~ 19 – 23 us. This time is equivalent to ~ 4 – 5 frames from the high speed camera capturing at 4.34 us/frame. Some of the crack velocity data reflects this behavior as the crack velocity suddenly drops for ~ 4 – 5th data point before again jumping to a higher velocity. For the samples that don't show this behavior, the crack velocities have already stabilized by 4 – 5th data point to a maximum value.

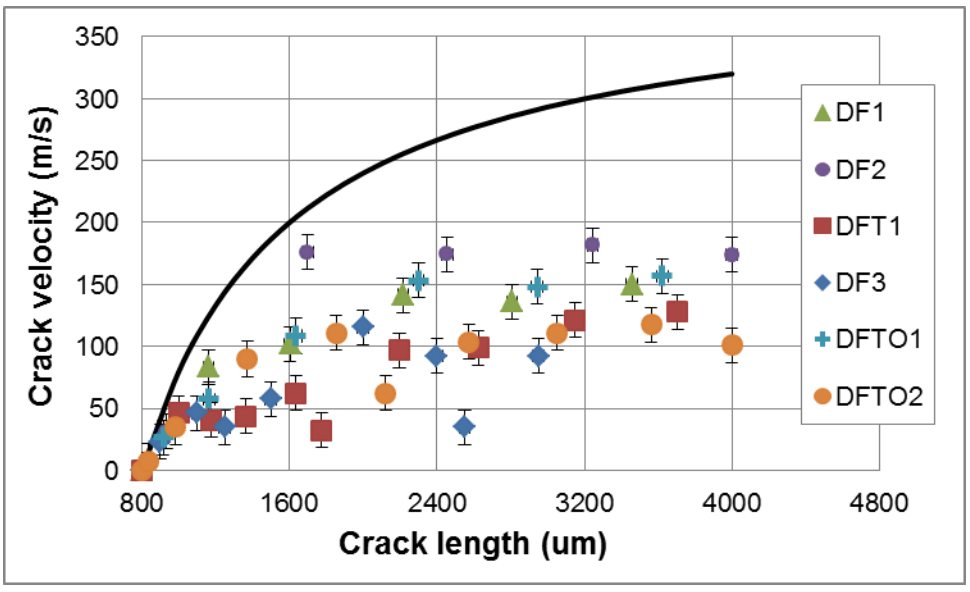

Figure 42: Crack velocity vs Crack length data for the dynamic fracture tests. The error in the crack length was estimated to be ± 30 um which gives error in the velocity measurement as ± 14 m/s. The black line represents the theoretical curve calculated from Equation 24.

One can estimate the strain rates from the crack velocity and the yield stress. The extent of the plastic zone (r_p) in front of the notch as calculated earlier is ~ 40 um. If we assume crack velocity (V) of ~ 100 m/s, the strain rate would be given by V/r_p. Hence the order of magnitude of the strain rate is ~ 10^6/s.

There wasn't much difference in the velocities of the oxidized and non-oxidized samples. This is in disagreement with results obtained by Sun [128], where she observed significantly higher crack velocities for oxidized NPG samples. The reason behind this could be the loading rates. The high crack velocities for NPG samples were observed for mainly the samples that were fractured on a vise where it is possible to obtain loading rates of ~ 1 – 10 mm/s. However, both the tests for the oxidized samples were conducted using the micro-mechanical testing device at a displacement rate of 3 um/s. Hence for those samples, the crack started at a smaller velocity and the velocity slowly increased. For these cracks, the shear wave reflected from the boundary limited the crack velocity at a lower value than the values obtained by Sun for similar tests on a vise.

The DIC displacement resolution tests using the high speed camera showed that the average displacements even of the order of 0.1 um were achievable from the DIC (Figure 43). However, the standard deviation from ~ 10000 data points from the sample surface for all three tests was ~ 0.25 um.

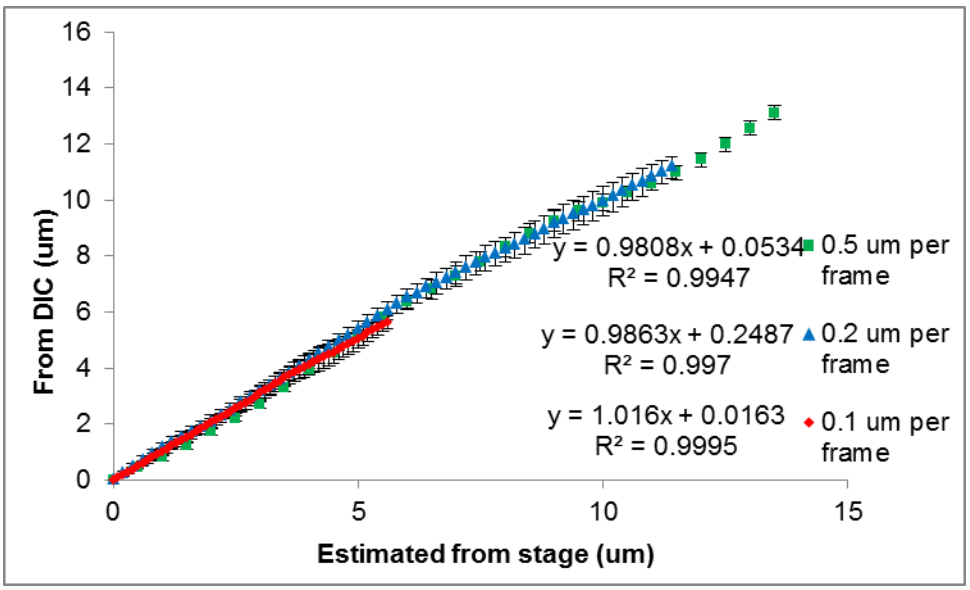

Figure 43: The displacement resolution test using the high speed camera showed that there was ~ 2 % error in the linear fit of the displacement estimated from the stage and the average displacement obtained from the sample surface (ideally the slope should be 1) for all three tests.

The static stress intensity factor (K_I^{stat}) was measured from the displacement field obtained from the sample surface using Equation 43 [122]

$$u = \frac{K_I^{stat}}{2G}\left(\frac{r}{2\pi}\right)^{\frac{1}{2}}\left\{\sin\left(\frac{\theta}{2}\right)\left[\kappa + 1 - 2\cos^2\left(\frac{\theta}{2}\right)\right]\right\} \qquad 43$$

Here u is the displacement in Y direction, K_I^{stat} is the static stress intensity, G is the shear modulus, r and θ are the co-ordinates of the point with respect to the notch tip where $\theta \in (-\pi, \pi)$ and $\kappa = (3 - v)/(1 + v)$ for plane stress where v is the Poisson's ratio.

A region behind the crack tip was selected to do this analysis. The displacement values of every point in that region were obtained from DIC analysis in ARAMIS. This analysis was performed using Matlab (Appendix D) on the images just prior to the fracture. The load during this time (~ 70 us) is essentially constant and equal to the fracture load of the sample. The static stress intensity calculated from the displacement field for the samples DFTO1 and DFTO2 were in agreement to those calculated from the measured fracture load values (Figure 44). This analysis could not be performed on other samples as an image prior to loading was not available to obtain the exact displacement values for the points on the sample surface.

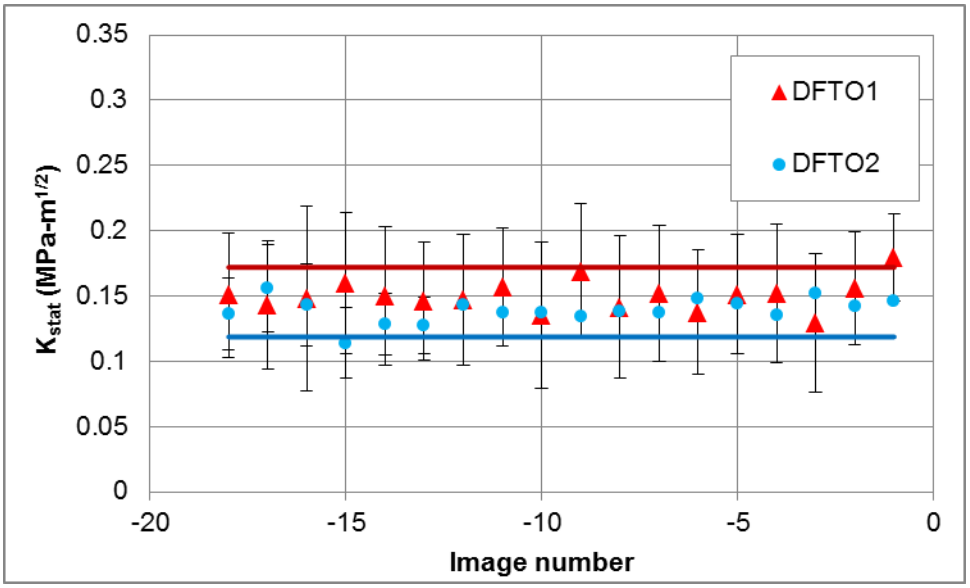

Figure 44: The critical stress intensity values calculated from the displacement field for the sample DFTO1 and DFTO2 were in fair agreement to the values calculated from the Equation 36 (solid lines) and the fracture stress obtained from the load cell. The error bars represents standard deviation in the K_{stat} values obtained for different points on the sample surface through DIC. Images prior to the fracture (0^{th} image) are shown here.

The dynamic stress intensity factor for the advancing crack was also calculated from the displacement field obtained from ARAMIS. The dynamic stress intensity analysis was performed on the sample DFT1 and DFTO2. The crack did not travel perpendicular to the loading direction for the sample DFTO1. The pixel resolution being small, the displacement field could not be obtained for that sample. Certain area behind the notch tip ($100^{o} < \theta < 170^{o}$) was used for this analysis. Two different ways were used to calculate the dynamic stress intensity:

1. K_{dyn} calculated from the Equation 15 using the K_{stat} values obtained from the fracture toughness tests,
2. K_{dyn} calculated from displacement rates obtained from the DIC analysis along with the Equation 20. Matlab code (Appendix C) was used to perform this analysis.

The dynamic fracture toughness ($\mathcal{G}_{dyn}$) was calculated from these K_{dyn} values using Equation 21. The standard deviation in the K_{dyn} values was used to obtain the error bars for $\mathcal{G}_{dyn}$. As seen in the Figure 45 and Figure 46, the K_{dyn} and the $\mathcal{G}_{dyn}$ values calculated from DIC are in good agreement with those calculated from the K_{stat} till 4 – 5^{th} data point. As discussed earlier, the

shear wave reflected from boundary takes ~ 16 – 20 us (4 – 5 frames) to affect the displacement field around the crack and limit the crack velocity. The same effect can be observed here in the K_{dyn} and $\mathcal{G}_{dyn}$ plots. The applied stress value at the time of onset of fracture, which is used to calculate the K_{stat}, is no longer applicable as load relaxation occurs at the sample surface. The crack acquires inertia after this interaction and the dynamic stress intensity and dynamic fracture toughness values are capped.

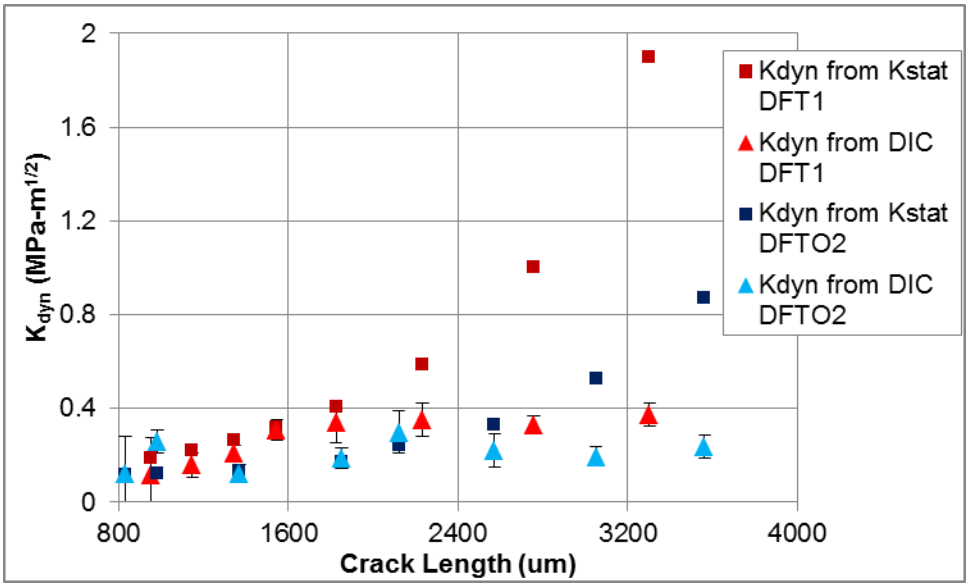

Figure 45: The dynamic stress intensity for sample DFT1 and DFTO2 increased till the shear wave – boundary interaction occurred.

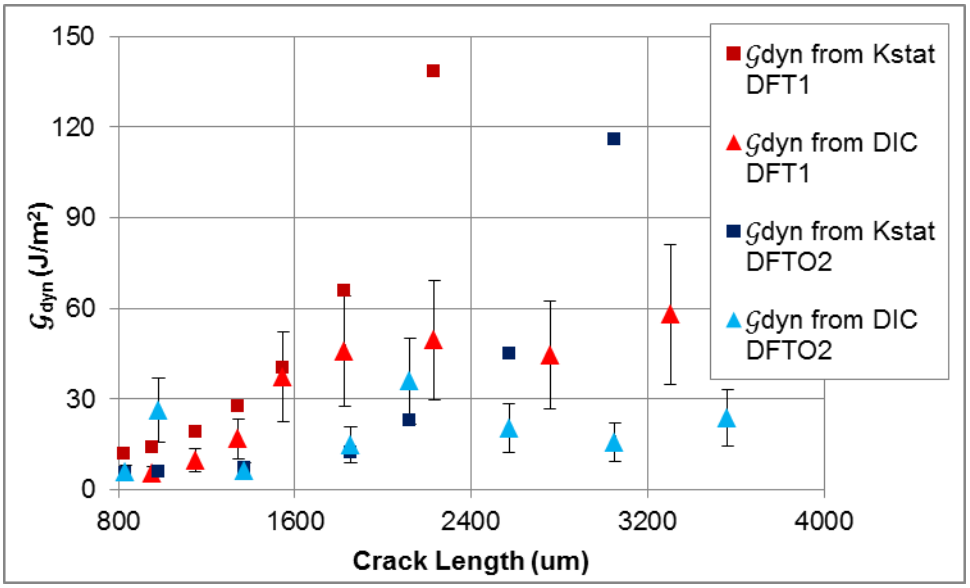

Figure 46: Dynamic fracture toughness values for sample DFT1 and DFTO2 were obtained from DIC were in agreement with those calculated from the K_{stat} value before the crack interacts with the boundary and acquires inertia.

The obtained crack velocities along with the mechanical properties of the parent phase can be used to make estimate of the crack penetration distance in transgranular cracking in AgAu alloy using the Equation 10. Figure 47, obtained through a simple Matlab simulation, shows how the crack velocity for a particular crack jump would slow down in such case for different values of n, number of dislocations emitted by a moving crack per burger's vector advance. This analysis assumes starting crack length of 1 mm, crack penetration velocity of 100 m/s, dislocation velocity = 0.1*shear wave velocity (the Equation is very weakly dependent on the dislocation velocity), b = 0.35 nm, dislocation core size of the order of a burger's vector whereas the size of the region encompassing a dislocation ~ 10 um (annealed sample has ~ 10^6 dislocations/cm^2 which gives ~ 10^3 dislocations/cm i.e. 10^{-3} cm (= 10 um)/dislocation). The surface free energy is assumed to be ~ 2 J/m^2.

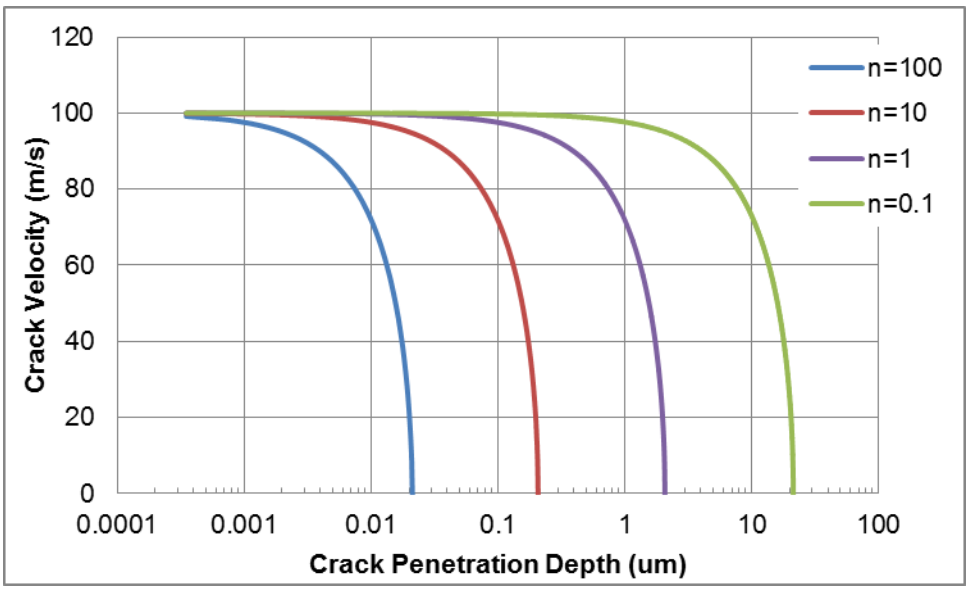

Figure 47: Crack penetration depth in $Ag_{70}Au_{30}$ alloy with starting velocity 100 m/s for different values of number of dislocations emitted by the moving crack per burger's vector advance in the parent phase.

Figure 48 shows that as the crack velocity in the brittle film increases, it penetrates deeper in the parent phase for a single crack jump. This simulation encompasses different velocities observed in the dynamic fracture tests. It is possible to obtain crack penetration depth of the order of 1 – 10 um for a starting crack of 1 mm with realistic crack velocities.

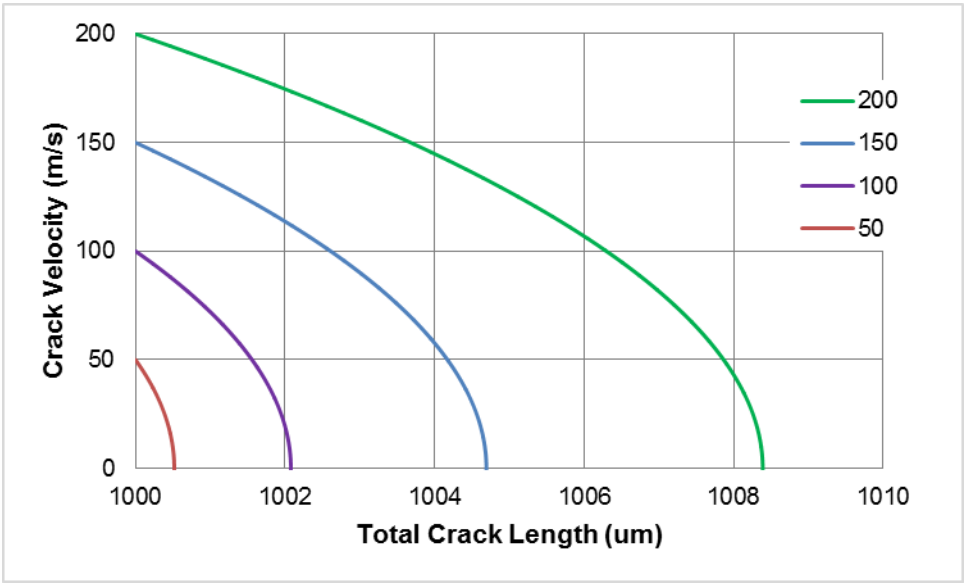

Figure 48: Effect of crack velocity on the crack penetration depth with 1 mm starting crack length and 1 dislocation emitted per burger's vector crack advance.

Typically the crack penetration doesn't stop after one crack arrest. The freshly exposed material again undergoes dealloying to form new brittle layer which can in turn inject cracks in the parent material. Now for the new analysis, the starting crack length would be the original crack length + the crack penetration depth. Another Matlab simulation was performed to see how the crack penetration distance changes as the crack length increases (Figure 49). This analysis was performed for n = 1 and other parameters same as the previous analysis.

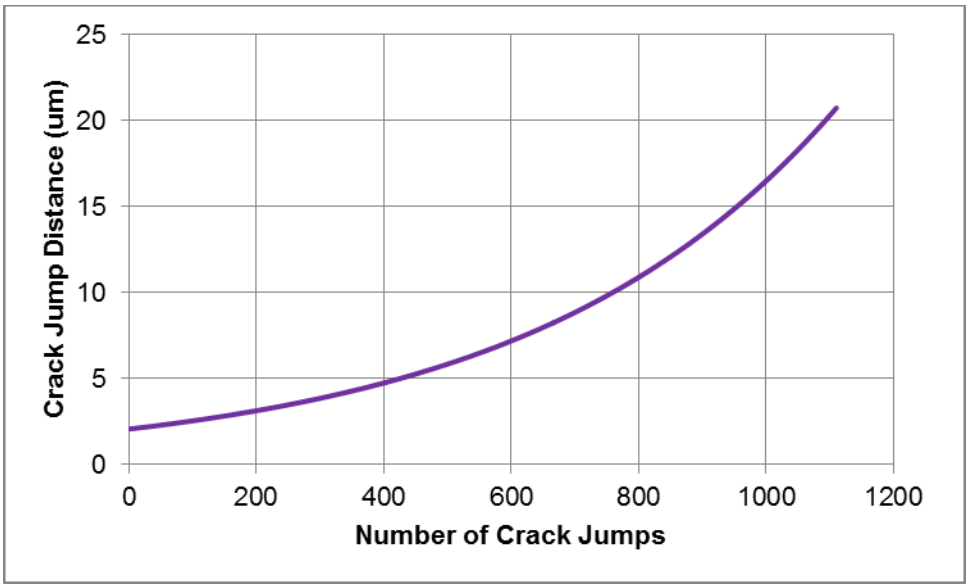

Figure 49: Evolution of crack jump distance as number of crack jumps increase.

It can be seen here that the crack penetration distance increases for each crack jump as the total crack length increases. The larger crack length would create larger stress intensity resulting in larger crack jump distance.

CHAPTER 4

CONCLUSIONS

All the control samples with no dealloying showed no porosity or excess Au inside the grain boundary in the TEM – EDS analysis and the APT analysis. All dealloyed cracked samples showed excess Au inside the grain boundary beyond the crack tip. One of the crack injection samples (# 2) showed porosity along the grain boundary beyond the crack tip for ~ 300 nm. Also the un-corroded control samples showed that the grain boundary composition is same as the bulk composition in both TEM – EDS and APT. At the same time, the APT analysis of the corroded sample showed excess Au in the grain boundary at ~ 1.1 um below the SEM visible dealloyed region. All these evidences point towards possible dealloying beyond the crack tip. However, the dealloyed control sample that was tested in the APT showed higher increase in the Au concentration inside the grain boundary for a point away from the surface than a point closer to the surface which is not consistent with possible dealloying. The sample 1 showed a decreasing trend of Au composition below the crack tip, whereas in case of the sample 2, this trend was not consistent with a possible corrosion down the GB. The point away from the crack tip (2 um) contained more Au (45 – 50%) than the point closer (0 – 500 nm) to the crack tip (40 – 42 %). The dealloyed unbent control samples that were tested in the TEM did not show any porosity beyond 600 – 700 nm from the surface along the grain boundary for similar bulk dealloyed layer thickness. Also, none of these samples had any porosity visible along the grain boundary beyond this point.

The samples which were immersed in the LN_2 after dealloying showed much deeper cracks than the samples immersed in water. The very low temperature of LN_2 converts the electrolyte to ice inhibiting any further corrosion. Also it suppresses surface diffusion of Au atoms keeping the ligament size to a very small value (~3 nm). Smaller the ligament size less is the chance of a dislocation being present in the material and more brittle the material is [58]. This can result in larger crack velocities with higher starting kinetic energy. This would give us much deeper cracks. The experimental results support this theory. The samples that were immersed in water for 1 hour before bending would have coarsened ligaments in the dealloyed layer. The

coarsened ligaments are not capable of forming high speed cracks due to their ductile nature. This would explain the shallower cracks observed in these samples.

Considering all these results, it is concluded that particular grain boundaries may have inherently higher Au concentration which may or may not depend on the adjacent grain orientations and such grain boundaries may be more susceptible to the cracking. Another possibility is that, particular grain boundaries may have higher dealloying rate which can depend on the adjacent grain orientation. This can be observed from Figure 18 and Figure 25 where both samples were dealloyed using the exact same protocol. The bulk dealloyed layer thickness for both the samples is similar (450 nm vs 470 nm). However, the depth of the V along the grain boundary is 1600 nm for sample 2 and 620 nm for sample 9. In spite of this, it is difficult to explain the grain boundary corrosion of 8 um for one grain boundary vs 620 nm for another grain boundary. The porosity beyond the crack tip may exist, if the crack propagation occurs by nucleation and growth model of the dynamic fracture. The stress waves are generated in the material when the crack travels at very high speed along the grain boundary during the quick bending. These waves can produce pores ahead of the main crack along the grain boundaries. The crack progress is simply a process where the advancing crack connects these pores producing more shock waves which in turn cause porosity formation along the grain boundary beyond the crack tip. The crack loses some energy during this process and finally when the energy drops below certain threshold, the crack gets arrested.

The results obtained for the Young's modulus are quite consistent for oxidized and non-oxidized NPG with very low standard deviation. The average modulus is ~ 2.5 GPa and the average Poisson's ratio is ~ 0.19 for non-oxidized and 0.24 for oxidized samples. These values are closest to those measured by Balk and coworkers [66, 67] in tensile tests and Ahn and Balogun [74] through laser ultrasonic measurements. The yield stress value of the NPG obtained from the CTOD test (16.80 MPa) is higher than that fracture stress of the tensile test sample (~ 11 MPa). This has been explained on the basis of the size effect on the strength of the material. The low yield stress observed for the oxidized NPG in the CTOD test and the fracture toughness

tests is attributed to the curvature observed in the sample after oxidation. The fracture toughness value obtained for the NPG samples is ~ 10 J/m^2.

The dynamic fracture tests yielded crack velocities in the NPG ~ 100 – 180 m/s. Also the DIC analysis of the dynamic fracture sample was performed to obtain and verify the static stress intensity observed in the fracture toughness test. The dynamic stress intensity and fracture toughness analysis of the dynamic fracture analysis supports the theory proposed by Goldman et al. [91] that the crack acts inertia-less until the shear wave generated by the moving crack is reflected from the boundaries and limits the crack velocity. The crack velocities obtained in the dynamic fracture tests were used to predict evolution of the crack penetration depth as crack progresses in transgranular SCC by film induced cleavage in AgAu alloy based on a model proposed by Sieradzki and Newman [46] with some modifications.

CHAPTER 5

FUTURE WORK

15 – 20 samples from each of an un-corroded and a corroded Ag-Au alloy sheet can be analyzed in the atom probe tomography to obtain a statistically significant result for the grain boundary composition in each case.

The mechanically cross-sectioned samples can be analyzed using the EBSD to obtain information about the grain orientation along with the crack depth for different grain boundaries. This can be useful to determine if there are particular grain boundaries which are more susceptible to the film induced cracking.

A fracture surface of an intergranular crack can be analyzed using Auger electron spectroscopy for composition along the crack face. Auger electrons are generated from very near surface region (~ 1 nm). This can be helpful to understand depth of the dealloying along the crack face above the crack tip.

The dealloyed layer thickness can be varied systematically keeping rest of the protocol constant and crack depth statistics along with EBSD data can help understand the crack injection phenomenon.

Different orientation Ag-Au alloy single crystals can be used to perform the crack injection experiment. The absence of the grain boundaries would facilitate the process of understanding the relative depths of the crack and the dealloyed layer. Also the crack jump model presented here can be verified using single crystal samples.

As recently observed by Zhong et al. [27], a Cu-Au sample can be dealloyed to form a monolithic crack free NPG with ligament size of ~ 10 nm. Such sample can be used to understand effect of ligament size on mechanical and dynamic fracture properties viz. Young's modulus, Poisson's ratio, fracture strength, crack velocity and fracture toughness of the NPG. Also AgAuPt alloys can be used to prepare monolithic NPG with ligament size ~ 5 nm. Here 2 – 5% Pt inhibits surface diffusion of Au preventing coarsening. This restricts the ligament diameter in the NPG.

REFERENCES

[1] J. Biener, A. Wittstock, L. Zepeda-Ruiz, M. Biener, V. Zielasek, D. Kramer, R. N. Viswanath, J. Weissmüller, M. Bäumer, A. Hamza, "Surface-chemistry-driven actuation in nanoporous gold," *Nature Materials,* vol. 8, no. 1, pp. 47-51, 2008.

[2] V. Zielasek, B. Jürgens, C. Schulz, J. Biener, M. Biener, A. Hamza,M. Bäumer, "Gold catalysts: nanoporous gold foams," *Angewandte Chemie International Edition,* vol. 45, no. 48, pp. 8241-8244, 2006.

[3] C. Xu, J. Su, X. Xu, P. Liu, H. Zhao, F. Tian, Y. Ding, "Low temperature CO oxidation over unsupported nanoporous gold," *Journal of the American Chemical Society,* vol. 129, no. 1, pp. 42-43, 2007.

[4] S. Kameoka, A. Tsai, "CO oxidation over a fine porous gold catalyst fabricated by selective leaching from an ordered AuCu3 intermetallic compound," *Catalysis Letters,* vol. 121, no. 3-4, pp. 337-341, 2008.

[5] R. Zeis, A. Mathur, G. Fritz, J. Lee, J. Erlebacher, "Platinum-plated nanoporous gold: An efficient, low Pt loading electrocatalyst for PEM fuel cells," *Journal of Power Sources,* vol. 165, no. 1, pp. 65-72, 2007.

[6] L. C. Nagle, J. F. Rohan, "Nanoporous gold anode catalyst for direct borohydride fuel cell," *International Journal of Hydrogen Energy,* vol. 36, no. 16, pp. 10319-10326, 2011.

[7] R. Zeis, T. Lei, K. Sieradzki, J. Snyder, J. Erlebacher, "Catalytic reduction of oxygen and hydrogen peroxide by nanoporous gold," *Journal of Catalysis,* vol. 253, no. 1, pp. 132-138, 2008.

[8] D. McCurry, M. Kamundi, M. Fayette, F. Wafula, N. Dimitrov, "All electrochemical fabrication of a platinized nanoporous Au thin-film catalyst," *ACS Applied Materials & Interfaces,* vol. 3, no. 11, pp. 4459-4468, 2011.

[9] A. Wittstock, V. Zielasek, J. Biener, C. Friend, M. Baumer, "Nanoporous gold catalysts for selective gas-phase oxidative coupling of methanol at low temperature," *Science,* vol. 327, no. 5963, pp. 319-322, 2010.

[10] H. Jin, X. Wang, S. Parida, K. Wang, M. Seo, J. Weissmuller, "Nanoporous Au− Pt alloys as large strain electrochemical actuators," *Nano letters,* vol. 10, no. 1, pp. 187-194, 2009.

[11] H. Jin, J. Weissmuller, "A material with electrically tunable strength and flow stress," *Science,* vol. 332, no. 6034, pp. 1179-1182, 2011.

[12] K. Hu, D. Lan, X. Li, S. Zhang, ""Electrochemical DNA biosensor based on nanoporous gold electrode and multifunctional encoded DNA− Au bio bar codes," *Analytical chemistry,* vol. 80, no. 23, pp. 9124-9130, 2008.

[13] [Online]. Available: http://www.nytimes.com/2014/10/20/business/power-plants-seek-to-extend-life-of-nuclear-reactors.html.

[14] J. Erlebacher, M. J. Aziz, A. Karma, N. Dimitrov, K. Sieradzki, "Evolution of nanoporosity in dealloying," *Nature,* vol. 410, no. 6827, pp. 450-453, 2001.

[15] H. W. Pickering, "Characteristic features of alloy polarization curves," *Corrosion Science,* vol. 23, no. 10, pp. 1107-1120, 1983.

[16] K. Sieradzki, R. newman, "Stress-corrosion cracking," *Journal of Physics and Chemistry of Solids,* vol. 48, pp. 1101-1113, 1987.

[17] H. Scher, R. Zallen, "Critical density in percolation processes," *The Journal of Chemical Physics,* vol. 53, no. 9, pp. 3759-3761, 1970.

[18] K. Sieradzki, "Curvature effects in alloy dissolution," *Journal of Electrochemical Society,* vol. 140, no. 10, pp. 2868-2872, 1993.

[19] K. Sieradzki, N. Dimitrov, D. Movrin, C. McCall, N. Vasiljevic, J. Erlebacher, "The dealloying critical potential," *Journal of Electrochemical Society,* vol. 149, no. 8, pp. B370-B377, 2002.

[20] J. Rugolo, J. Erlebacher, K. Sieradzki, "Length scales in alloy dissolution and measurement of absolute interfacial free energy," *Nature Materials,* vol. 5, no. 12, pp. 946-949, 2006.

[21] H. Baker and H. Okamoto, ASM handbook: Alloy phase diagrams, 3, 1992.

[22] A. M. Hodge, J. R. Hayes, J. A. Caro, J. Biener, A. V. Hamza, "Characterization and Mechanical Behavior of Nanoporous Gold," *Advanced Engineering Materials,* vol. 8, no. 9, pp. 853-857, 2006.

[23] A. M. Hodge,, J. Biener, J.R. Hayes, P.M. Bythrow, C.A. Volkert, A.V. Hamza, "Scaling equation for yield strength of nanoporous open-cell foams," *Acta Materialia,* vol. 55, pp. 1343-1349, 2007.

[24] J. Snyder, K. Livi, J. Erlebacher, "Dealloying Silver/Gold Alloys in Neutral Silver Nitrate Solution: Porosity Evolution, Surface Composition, and Surface Oxides," *Journal of Electrochemical Society,* vol. 155, no. 8, pp. C464-C473, 2008.

[25] Y. Sun, T. J. Balk, "A multi-step dealloying method to produce nanoporous goldwith no volume change and minimal cracking," *Scripta Materialia,* vol. 58, pp. 727-730, 2008.

[26] H. Jin, L. Kurmanaeva, J. Schmauch, H. Rosner, Y. Ivanisenko, J. Weissmuller, "Deforming nanoporous metal: Role of lattice coherency," *Acta Materialia,* vol. 57, no. 9, pp. 2665-2672, 2009.

[27] Y. Zhong, J. Markmann, H. J. Jin, Y. Ivanisenko, L. Kurmanaeva, J. Weissmuller, "Crack Mitigation during Dealloying of Au25Cu75," *Advanced Engineering Materials,* vol. 16, no. 4, pp. 389-398, 2014.

[28] J. Snyder, P. Asanithi, A. Dalton, J. Erlebacher, "Stabilized nanoporous metals by dealloying ternary alloy precursors," *Advanced materials,* vol. 20, pp. 4883-4886, 2008.

[29] Y. Ding, Y. Kim, J. Erlebacher, "Nanoporous gold leaf: "Ancient technology" / Advance material," *Advanced materials,* vol. 16, no. 21, pp. 1897-1900, 2004.

[30] L. H. Qian, M. W. Chen, "Ultrafine nanoporous gold by low-temperature dealloying and kinetics of nanopore formation," *Applied physics letters,* vol. 91, p. 083105, 2007.

[31] R. A. Oriani, in *Stress Corrosion Cracking and Hydrogen Embrittlement of Iron Base Alloys*, Houston, TX, NACE, 1973, p. 351.

[32] C. D. Beachem, "A new model for hydrogen-assisted cracking (hydrogen “embrittlement”)," *Metallurgical transactions,* vol. 3, no. 2, pp. 441-455, 1972.

[33] H. K. Birnbaum, I. M. Robertson, P. Sofronis, D. Teter, "Mechanisms of hydrogen related fracture - a review," in *Second International Conference on Corrosion-Deformation Interactions. CDI'96*, 1996.

[34] N. J. Petch, P. Stables, "Delayed fracture of metals under static load," *Nature,* vol. 169, pp. 842-843, 1952.

[35] A. A. Griffith, *Philosophical transactions of the royal society of London. A211,* p. 163, 1921.

[36] H. H. Uhlig, in *Fundamental Aspects of Stress Corrosion Cracking*, Houston, TX, NACE, 1969, p. 86.

[37] S. P. Lynch, "Environmentally assisted cracking: overview of evidence for an adsorption-induced localised-slip process," *Acta Metallurgica,* vol. 36, no. 10, pp. 2639-2661, 1988.

[38] J. Galvele, "A stress corrosion cracking mechanism based on surface mobility," *Corrosion Science,* vol. 27, no. 1, pp. 1-33, 1987.

[39] J. Galvele, "Surface mobility mechanism of stress-corrosion cracking," *Corrosion science,* vol. 35, no. 1, pp. 419-434, 1993.

[40] J. Galvele, "Enhanced Surface mobility as the cause of stress corrosion cracking," *Journal of the Electrochemical Society,* vol. 133, no. 5, pp. 953-954, 1986.

[41] F. R. N. Nabarro, "Report of a Conference on the Strength of Solids," Physical Society, London, 1948.

[42] C. Herring, "Diffusional viscosity of a polycrystalline solid," *Journal of Applied Physics,* vol. 21, pp. 437-445, 1950.

[43] K. Sieradzki, F. Friedersdorf, "Notes on the surface mobility mechanism of stress-corrosion cracking," *Corrosion Science,* vol. 36, no. 4, pp. 669-675, 1994.

[44] D. A. Vermilyea, "A theory for the propagation of stress corrosion cracks in metals," *Journal of the Electrochemical Society,* vol. 119, no. 4, pp. 405-407, 1972.

[45] R. N. Parkins, "Predictive approaches to stress corrosion cracking failure," *Corrosion*

Science, vol. 20, no. 2, pp. 147-166, 1980.

[46] K. Sieradzki and R. Newman, "Brittle behavior of ductile metals during stress-corrosion cracking," *Philosophical Magazine A,* vol. 51, no. 1, pp. 95-132, 1985.

[47] C. Edeleanu, A.J. Forty, "Some observations on the stress-corrosion cracking of α-brass and similar alloys," *Philosophical Magazine,* vol. 5, no. 58, pp. 1029-1040, 1960.

[48] N. F. Mott, "Fracture of metals: theoretical considerations," *Engineering,* vol. 165, no. 4275, pp. 16-18, 1948.

[49] F. R. N. Nabarro, Theory of Crystal Dislocation, Oxford University Press, 1967.

[50] U. Bertocci, "Modeling of Crack Chemistry in Cu-Au Alloys," *Journal of Electrochemical Society,* vol. 136, no. 7, pp. 1887-1892, 1989.

[51] T. B. Cassagne, W. F. Flanagan, B. D. Lichter, "On the failure mechanism of chemically embrittled Cu3Au single crystals," *Metallurgical Transactions A,* vol. 17, no. 4, pp. 703-710, 1986.

[52] T. B. Cassagne, W. F. Flanagan, B. D. Lichter, "Transgranular stress-corrosion cracking of disordered Cu-25Au in aqueous chloride and sulfate media," *Metallurgical Transactions A,* vol. 19, no. 2, pp. 281-292, 1988.

[53] R. Newman, T. Shahrabi, K. Sieradzki, "Film-induced cleavage of alpha-brass," *Scripta metallurgica,* vol. 23, no. 1, pp. 71-74, 1988.

[54] R. G. Kelly, A. J. Frost, T. Shahrabi, R. C. Newman, "Brittle fracture of an Au/Ag alloy induced by a surface film," *Metallurgical Transactions A,* vol. 22, no. 2, pp. 531-541, 1991.

[55] R. P. Reed, A. F. Clark, "Materials at low temperatures," *American Society for Metals,* vol. 1983, p. 590, 1983.

[56] F. Friedersdorf, "Stress-Corrosion Cracking of Binary Noble Metal Alloys (Dissertation)," 1993.

[57] M. Saito, G. S. Smith, R. C. Newman, "Testing the film-induced cleavage model of stress-corrosion cracking," *Corrosion Science,* vol. 35, no. 1, pp. 411-417, 1993.

[58] R. Li, K. Sieradzki, "Ductile-brittle transition in random porous Au," *Physical Review Letters,* vol. 68, no. 8, p. 1168, 1992.

[59] J. S. Chen, T. M. Devine, M. Salmeron, "Brittle Fracture of Cu-30 Au Induced by a Surface Layer," *Journal of The Electrochemical Society,* vol. 139, no. 6, pp. L55-L57, 1992.

[60] J. S. Chen, M. Salmeron, T. M. Devine, "Intergranular and transgranular stress corrosion cracking of Cu-30Au," *Corrosion Science,* vol. 34, no. 12, pp. 2071-2097, 1993.

[61] F. Friedersdorf, K. Sieradzki, "Film-induced brittle intergranular cracking of silver-gold

alloys," *Corrosion Science,* vol. 52, no. 5, pp. 331-336, 1996.

[62] C. A. Volkert, E. T. Lilleodden, D. Kramer, J. Weissmüller, "Approaching the theoretical strength in nanoporous Au," *Applied Physics Letters,* vol. 89, no. 6, pp. 061920-061920, 2006.

[63] A. Barnes, N. A. Senior, R. C. Newman, "Film-induced cleavage of Ag-Au alloys," *Metallurgical and Materials Transactions A,* vol. 40, no. 1, pp. 58-68, 2009.

[64] L. J. Gibson, M. F. Ashby, Cellular Solids: Structure and Properties (2nd edition), Cambridge, U.K.: Cambridge University Press, 1997.

[65] J. Biener, A. M. Hodge, A. V. Hamza, L. M. Hsiung, J. H. Satcher, Jr., "Nanoporous Au: A high yield strength material," *Journal of Applied Physics,* vol. 97, no. 2, p. 024301, 2005.

[66] T. J. Balk, C. Eberl, Y. Sun, K. J. Hemker, D. S. Gianola, "Tensile and compressive microspecimen testing of bulk nanoporous gold," *JOM,* vol. 61, no. 12, pp. 26-31, 2009.

[67] N. J. Briot, T. Kennerknecht, C. Eberl, T. J. Balk, "Mechanical properties of bulk single crystalline nanoporous gold investigated by millimetre-scale tension and compression testing," *Philosophical Magazine,* vol. 94, no. 8, pp. 847-866, 2014.

[68] A. Mathur, J. Erlebacher, "Size dependence of effective Young's modulus of nanoporous gold," *Applied physics letters,* vol. 90, no. 6, p. 061910, 2007.

[69] D. Farkas, A. Caro, E. Bringa, D. Crowson, "Mechanical response of nanoporous gold," *Acta Materialia,* vol. 61, no. 9, pp. 3249-3256, 2013.

[70] R. Xia, C. Xu, W. Wu, X. Li, X. Feng, Y. Ding, "Microtensile tests of mechanical properties of nanoporous Au thin films," *Journal of materials science,* vol. 44, no. 17, pp. 4728-4733, 2009.

[71] D. Lee, X. Wei, X. Chen, M. Zhao, S. C. Jun, J. Hone, E. G. Herbert, W. C. Oliver, J. W. Kysar, "Microfabrication and mechanical properties of nanoporous gold at the nanoscale," *Scripta materialia,* vol. 56, no. 5, pp. 437-440, 2007.

[72] N. Mameka, J. Markmann, H. Jin, J. Weissmüller, "Electrical stiffness modulation—confirming the impact of surface excess elasticity on the mechanics of nanomaterials," *Acta Materialia,* vol. 76, pp. 272-280, 2014.

[73] X. Sun, G. Xu, X. Li, X. Feng, H. Gao, "Mechanical properties and scaling laws of nanoporous gold," *Journal of Applied Physics,* vol. 113, no. 2, p. 023505, 2013.

[74] P. Ahn, O. Balogun, "Elastic characterization of nanoporous gold foams using laser based ultrasonics," *Ultrasonics,* vol. 54, no. 3, pp. 795-800, 2014.

[75] J. Biener, A. M. Hodge, A. V. Hamza, "Microscopic failure behavior of nanoporous gold," *Applied Physics Letters,* vol. 87, no. 12, p. 121908, 2005.

[76] C. E. Inglis, "Stresses in a cracked plate due to the presence of cracks and sharp corners,"

Transaction of Naval Architects (London), vol. 60, pp. 219-230, 1913.

[77] A. A. Griffith, "The phenomena of rupture and flow in solids," *Philosophical transactions of the royal society of london. Series A, containing papers of a mathematical or physical character,* pp. 163-198, 1921.

[78] G. R. Irwin, "Analysis of stresses and strains near the end of a crack traversing a plate," *Journal of Applied Mechanics,* 1957.

[79] L. B. Freund, Dynamic Fracture Mechanics, New York: Cambridge University Press, 1990.

[80] L. E. Kinsler, A. R. Frey, A. B. Coppens, Fundamentals of Acoustics, New York: Wiley-VCH, 1999.

[81] E. Bouchbinder, T. Goldman, J. Fineberg, "The dynamics of rapid fracture: instabilities, nonlinearities and length scales," *Reports on Preogress in Physics,* vol. 77, no. 4, p. 046501, 2014.

[82] J. P. Berry, "Some kinetic consideration of the Griffith criterion for fracture - I Equation of motion at constant force," *Journal of mechanics and physics of solids,* vol. 8, pp. 194-206, 1960.

[83] K. Ravi-chandar, "Dynamic fracture of nominally brittle materials," *International journal of fracture,* vol. 90, pp. 83-102, 1998.

[84] F. Abraham, D. Brodbeck, R. Rafey, W. Rudge, "Instability dynamics of fracture: A computer simulation investigation," *Physical review letters,* vol. 73, no. 2, p. 272, 1994.

[85] M. Marder, S. Gross, "Origin of crack tip instabilities," *Journal of the Mechanics and Physics of Solids,* vol. 43, pp. 1-48, 1995.

[86] X. Xu, A. Needlemena, "Numerical simulations of fast crack growth in brittle solids," *Journal of the mechanics and physics of solids,* vol. 42, pp. 1397-1434, 1994.

[87] D. R. Curran, D. A. Shockey, L. Seaman, "Dynamic fracture criteria for a polycarbonate," *Journal of applied physics,* vol. 44, pp. 4025-4038, 1973.

[88] E. Johnson, "Process region changes for rapidly propagating cracks," *International journal of fracture,* vol. 55, pp. 47-63, 1992.

[89] J. Carlsson, L. Dahlberg, F. Nilsson, M. P. Wnuk, "Experimental studies of the unstable phase of crack propagation in metals and polymers," *Proceedings of an international conference on Dynamic Crack Propagation,* pp. 165-181, 1973.

[90] F. Kerkhof, "General Lecture Wave fractographic investigations of brittle fracture dynamics," *Proceedings of an international conference on Dynamic Crack Propagation,* pp. 3-35, 1973.

[91] T. Goldman, A. Livne, J. Fineberg, "Acquisition of inertia by a moving crack," *Physical Review Letter,* vol. 104, no. 11, p. 114301, 2010.

[92] E. Sharon, J. Fineberg, "The dynamics of fast fracture," *Advanced Engineering Materials,* vol. 1, no. 2, pp. 119-122, 1999.

[93] A. J. Rosakis, O. Samudrala, D. Coker, "Cracks faster than the shear wave speed," *Science,* vol. 248, no. 5418, pp. 1337-1340, 1999.

[94] B. Pan, K. Qian, H. Xie, A. Asundi, "Two-dimensional digital image correlation for in-plane displacement and strain measurement: a review," *Measurement science and technology,* vol. 20, no. 6, p. 062001, 2009.

[95] W. G. Knauss, I. Chasiotis, Y. Huang, "Mechanical measurements at the micron and nanometer scales," *Mechanics of Materials,* vol. 35, no. 3, pp. 217-231, 2003.

[96] W. H. Press, C++ Numerical Algorithms, Beijing: Publishing House of Electronics Industry, 2003.

[97] H. W. Schreier, J. R. Braasch, M. A. Sutton, "Systematic errors in digital image correlation caused by intensity interpolation," *Optical Engineering,* vol. 39, no. 11, pp. 2915-2921, 2000.

[98] B. Pan, H. Xie, Z. Guo, T. Hua, "Full-field strain measurement using a two-dimensional Savitzky-Golay digital differentiator in digital image correlation," *Optical Engineering,* vol. 46, no. 3, p. 033601, 2007.

[99] P. F. Luo, Y. J. Chao, M. A. Sutton, W. H. Peters III, "Accurate measurement of three-dimensional deformations in deformable and rigid bodies using computer vision," *Experimental Mechanics,* vol. 33, no. 2, pp. 123-132, 1993.

[100] J. D. Helm, S. R. McNeil, M. A. Sutton, "Improved three-dimensional image correlation for surface displacement measurement," *Optical Engineering,* vol. 35, no. 7, pp. 1911-1920, 1996.

[101] D. Garcia, J. J. Orteu, L. Penazzi, "A combined temporal tracking and stereo-correlation technique for accurate measurement of 3D displacements: application to sheet metal forming," *Journal of Materials Processing Technology,* vol. 125, pp. 736-742, 2002.

[102] B. Pan, H. Xie, L. Yang, Z. Wang, "Accurate measurement of satellite antenna surface using 3D digital image correlation technique," *Strain,* vol. 45, no. 2, pp. 194-200, 2009.

[103] B. K. Bay, T. S. Smith, D. P. Fyhrie., M. Saad, "Digital volume correlation: three-dimensional strain mapping using X-ray tomography," *Experimental Mechanics,* vol. 39, no. 3, pp. 217-226, 1999.

[104] T. S. Smith, B. K. Bay, M. M. Rashid, "Digital volume correlation including rotational degrees of freedom during minimization," *Experimental Mechanics,* vol. 42, no. 3, pp. 272-278, 2002.

[105] M. S. Kirugulige, H. V. Tippur, T. S. Denney, "Measurement of transient deformations using digital image correlation method and high-speed photography: application to dynamic fracture," *Applied Optics,* vol. 46, no. 22, pp. 5083-5096, 2007.

[106] J. Abanto-Bueno, J. Lambro, "Investigation of crack growth in functionally graded materials using digital image correlation," *Engineering Fracture Mechanics,* vol. 69, no. 14, pp. 1695-1711, 2002.

[107] S. Roux, J. Rethore, F. Hild, "Digital image correlation and fracture: an advanced technique for estimating stress intensity factors of 2D and 3D cracks," *Journal of Physics D: Applied Physics,* vol. 42, p. 214004, 2009.

[108] S. Roux, F. Hild, "Stress intensity factor measurements from digital image correlation: post-processing and integrated approaches," *International Journal of Fracture,* vol. 140, pp. 141-157, 2006.

[109] V. Tarigopula, O. S. Hopperstad, M. Langseth, A. H. Clausen, F. Hild, "A study of localisation in dual-phase high-strength steels under dynamic loading using digital image correlation and FE analysis," *International Journal of Solids and Structures,* vol. 45, pp. 601-619, 2008.

[110] A. Dursun, D. V. Pugh, S. G. Corcoran, "Probing the Dealloying Critical Potential: Morphological Characterization and Steady-State Current Behavior," *Journal of The Electrochemical Society,* vol. 152, no. 2, pp. B65-B72, 2005.

[111] E. W. Muller, Advances in electronics and electron physics, vol. 13, New York: Marton, 1960, p. 83.

[112] C. A. Volkert, A. M. Minor, "Focused ion beam microscopy and micromachining," *MRS Bulletin,* vol. 32, no. 05, pp. 389-399, 2007.

[113] K. A. Telari, B. R. Rogers, H. Fang, L. Shen, R. A. Weller, D. N. Braski, "Characterization of platinum films deposited by focused ion beam-assisted chemical vapor deposition," *Journal of Vacuum Science & Technology,* vol. B20, no. 2, pp. 590-595, 2002.

[114] L. A. Giannuzzi, F. A. Stevie, "A review of focused ion beam milling techniques for TEM specimen preparation," *Micron,* vol. 30, no. 3, pp. 197-204, 1999.

[115] D. B. Williams, C. B. Carter, in *Transmission Electron Microscopy*, Springer, 2009.

[116] G. Cliff, G. W. Lorimer, "The quantitative analysis of thin specimens," *Journal of Microscopy,* vol. 103, no. 2, pp. 203-207, 1975.

[117] T. Malis, S. C. Cheng, R. F. Egerton, "EELS log-ratio technique for specimen-thickness measurement in the TEM," *Journal of electron microscopy technique,* vol. 8, no. 2, pp. 193-200, 1988.

[118] [Online]. Available: http://atomprobe.materials.ox.ac.uk/.

[119] E. W. Müller, J. A. Panitz , S. B. McLane, "The Atom-Probe Field Ion Microscope," *Review of Scientific Instruments,* vol. 39, no. 1, pp. 83-86, 1968.

[120] M. K. Miller, Atom Probe Tomography: Analysis at the Atomic Level, New York, NY: Kluwer

Academic/Plenum Press, 2000.

[121] M. K. Miller, A. Cerezo, M. G. Hetherington and G. D. W. Smith, Atom Probe Field Ion Microscopy, Oxford: Oxford University Press, 1996.

[122] D. Broek, Elementary Engineering Fracture Mechanics, Leyden, Netherlands: Noordhoff International Publishing, 1974.

[123] P. Crozier , M. Catalano, R. Cingolani, "A modeling and convolution method to measure compositional variations in strained alloy quantum dots," *Ultramicroscopy,* vol. 94, no. 1, pp. 1-18, 2003.

[124] P. M. Duxbury, "Breakdown of diluted and hierarchical systems," in *Statistical models for the fracture of disordered media (Ed. H. J. Herrmann, S. Roux)*, New York, Elsevier Science Publishers B. V. (North-Holland), 1990, pp. 189-228.

[125] [Online]. Available: http://www.thorlabs.us/newgrouppage9.cfm?objectgroup_id=3423.

[126] M.M. McCann, "Nanoindentation of Gold Single (Dissertation)," 2004.

[127] P. M. Duxbury, P. L. Leath, "Exactly solvable models of material breakdown," *Physical review B,* vol. 49, no. 18, p. 12676, 1994.

[128] S. Sun, "Dealloying Induced Stress Corrosion Cracking (Dissertation)," 2012.

[129] D. J. Tulimieri, J. Yoon, M. H. W. Chan, "Ordering of Helium Mixtures in Porous Gold," *Physical Review Letters,* vol. 82, no. 1, p. 121, 1999.

APPENDIX A

MATLAB CODE FOR EDS QUANTITATIVE ANALYSIS

```
clear;
close all;

% Name of the EDS text file “1.txt” and name of the info file “1 info.txt” in the current folder in
Matlab

for num1 = 1
   % You can also give multiple input if more than one file e.g. instead of num1=1 it can be
num1=[2, 4:13, 15:27, 29:48, 54:58]
   clearvars -except num1
   close all;
   num = num2str(num1);
   file_name = strcat(num, '.txt');
   data1 = textread(file_name);
   data=data1;
   % info.txt contents:
   % 1st line: Ag composition in bulk (%)
   % 2nd line: Length of the line scan in nm
   % 3rd line: Start point of bulk in nm
   % 4th line: End point of bulk in nm
   % 5th line: EOF (For some Matlab versions EOF is not needed)
   % e.g.
   % 70
   % 58.88
   % 40
   % 58.88
   % EOF

   info_file_name = strcat(num, 'info.txt');
   info = textread(info_file_name);
   Ag_comp=info(1);
   Au_comp=100-Ag_comp;
   line_length=info(2);
   bulk1=info(3);
   bulk2=info(4);
   [numrows, numcols] = size(data);
   data=data(1:numrows, 1:2048);
   [numrows, numcols] = size(data);
   line_scan = zeros(1,numrows);
   counts_Ag = zeros(numrows);
   counts_Au = zeros(numrows);
   counts_Pt = zeros(numrows);
   PtbyAu = zeros(numrows);
   comp_Ag = zeros(numrows);
   comp_Au = zeros(numrows);
   for i=1:numrows
      line_scan(i)=line_length/(numrows-1)*(i-1);
   end
   bulk1pt=floor(bulk1/line_length*(numrows-1))+1;
   bulk2pt=floor(bulk2/line_length*(numrows-1))+1;
   % numcols should be 2048 numrows should be number of pixels along line scan

   %% background subtraction
   x=1:numcols;
   S = sum(data(bulk1pt:bulk2pt,:));
```

```
S1=S;
window_size = 50;
midpts = [400:750];
[numrows1, numcols1] = size(midpts);
sums = zeros(1,numcols1);
midptsXsums = zeros(1,numcols1);
smdpt = zeros(1,numcols1);
for i = 1:numcols1
   smdpt(1,i) = S(1,midpts(i));
   sums(1,i) = sum(S(1,midpts(1,i)-window_size/2:midpts(1,i)+window_size/2));
   midptsXsums(1,i) = sums(1,i)*midpts(i);
end
[fitcrv, gof] = fit(transpose(midpts),transpose(smdpt),'poly1');
bck = fitcrv.p1*x+fitcrv.p2;
wtd_bck = bck/sum(S);
row_sum = zeros(1,numrows);
for i = 1:numrows
   row_sum(1,i) = sum(data(i,:));
   for j = 1:numcols
      data(i,j) = data(i,j) - wtd_bck(1,j)*row_sum(1,i);
   end
end
S = sum(data(bulk1pt:bulk2pt,:));

%% Peak finding
% Ag peak
S_Ag = S(1, 250:360);
[pk,peak_Ag] = max(S_Ag);
peak_Ag=peak_Ag+249;
i=peak_Ag;
while(S(1,i)>pk/2)
   i=i-1;
end
Ag_window_1=i;
i=peak_Ag;
while(S(1,i)>pk/2)
   i=i+1;
end
Ag_window_2=i;
% Au peak
S_Au = S(1, 950:990);
[pk,peak_Au] = max(S_Au);
peak_Au=peak_Au+949;
i=peak_Au;
while(S(1,i)>pk/2)
   i=i-1;
end
Au_window_1=i;
i=peak_Au;
while(S(1,i)>pk/2)
   i=i+1;
end
Au_window_2=i;
Ag_window_1=288;
Ag_window_2=331;
```

```
Au_window_1=958;
Au_window_2=994;

%% Measure counts
%Ag
for i=1:numrows
    counts_Ag(i)=0;
    for j=Ag_window_1:Ag_window_2
        counts_Ag(i)=counts_Ag(i)+data(i,j);
    end
end
%Au
for i=1:numrows
    counts_Au(i)=0;
    for j=Au_window_1:Au_window_2
        counts_Au(i)=counts_Au(i)+data(i,j);
    end
end
%Pt
for i=1:numrows
    counts_Pt(i)=0;
    for j=Au_window_1-27:Au_window_2-27
        counts_Pt(i)=counts_Pt(i)+data(i,j);
    end
    PtbyAu(i)=counts_Pt(i)/counts_Au(i);
end
%% Composition: Cliff Lorimer k factor calculations
sumk = 0;
PtbyAusum = 0;
for i=bulk1pt:bulk2pt
    sumk = sumk + counts_Ag(i)/(counts_Ag(i)+counts_Au(i));
    PtbyAusum = PtbyAusum + PtbyAu(i);
end
k=0.7/(sumk/(bulk2pt-bulk1pt+1));
PtbyAuave = PtbyAusum/(bulk2pt-bulk1pt+1);
PtbyAustdev = std(PtbyAu(bulk1pt:bulk2pt));
sample_start = 0;
sample_end = 0;
%% Pt effect
%    PtbyAu ratio is used to determine where Pt effect starts mean and standard deviation of
PtbyAu values inside bulk/un-corroded sample is calculated and extreme points beyond which the
PtbyAu ratio is more than mean + 3*std dev are considered
for i=1:numrows
    if (PtbyAu(i)<3*PtbyAustdev+PtbyAuave && sample_start == 0)
        sample_start = i;
    else
        sample_end = i;
    end
end
for i=sample_start:sample_end
    comp_Ag(i)=k*counts_Ag(i)/(counts_Ag(i)+counts_Au(i))*100;
    comp_Au(i)=100-comp_Ag(i);
end
for i=1:numrows
    if (comp_Ag(i)==0 && comp_Au(i) == 0 ||...
```

```
            PtbyAu(i)>3*PtbyAustdev+PtbyAuave)
        comp_Ag(i) = NaN;
        comp_Au(i) = NaN;
      end
   end
   trans_line_scan = transpose(line_scan);
   %% Output
   % Graph of Ag and Au composition
   hl1 = line(line_scan,comp_Ag,'Color','b');
   hl1 = line(line_scan,comp_Au,'Color','r');
   ax1 = gca;
   set(ax1,'XColor','r','YColor','r','XGrid','on','YGrid','on',...
      'Ylim',[0 100]);
   ax2 = axes('Position',get(ax1,'Position'),...
      'XAxisLocation','top','YAxisLocation','right',...
      'Color','none','Xlim',get(gca,'xlim'),'Ylim',[-2 6],...
      'XColor','k','YColor','k');
   hl2 = line(line_scan,PtbyAu,'Color','k','Parent',ax2);
   output_fig_name = num;
   saveas(gcf,output_fig_name,'jpg');
   close all;
   % Write relevant data to an excel file output.xlsx; This creates separate sheet for each file with
1st row as position along the scan line in nm, second row Ag composition in % and third row Au
composition in. Also creates another file summary.xlsx with information regarding k factor and Ag
and Au windows for every EDS scan analysis%
   rowsstr = num2str(numrows);
   xlswrite('output.xlsx',{'nm', 'Ag', 'Au'},num,'A1:C1');
   rangenm = strcat('A2:A',rowsstr);
   xlswrite('output.xlsx',trans_line_scan,num,rangenm);
   rangeAg = strcat('B2:B',rowsstr);
   xlswrite('output.xlsx',comp_Ag,num,rangeAg);
   rangeAu = strcat('C2:C',rowsstr);
   xlswrite('output.xlsx',comp_Au,num,rangeAu);
   if (max(comp_Au(1,:))==0)
      maxAu = max(comp_Au(:,1));
   else
      maxAu = max(comp_Au(1,:));
   end
   summary_range = strcat('A',num,':I',num);
   summary = {num, k,
maxAu,Ag_window_1,peak_Ag,Ag_window_2,Au_window_1,peak_Au,Au_window_2};
   xlswrite('summary.xlsx',summary,summary_range);
end
```

APPENDIX B

MATLAB CODE FOR CRACK VELOCITY ANALYSIS

```
% Open the directory with all txt files from ARAMIS with section along crack

clear
d = dir('*.txt');
nfiles = length(d);
data1 = [];
for k = 1:nfiles
    data1 = [data1; importdata(d(k).name,' ',14)]; % 14 lines of header
    strain(:,k) = data1(k,1).data(:,12); % 12th column is the column for y strain hence data1(:,12)
end
ptpos1(:,1) = data1(1,1).data(:,2);
ptpos1(:,2) = data1(1,1).data(:,3);
[rows,columns] = size(ptpos1);
threshold =1.1; % eyy(%) threshold for CT location
strainx=size(strain,1);
% initial notch position mm
notchpos = [0.310,0];
ctpos = zeros(nfiles,3);
for i = 1:nfiles
    ctpos(i,1) = i;
    if (max(strain(:,i)>threshold))
        p=1;
        while(threshold>strain(p,i)) %crack moving from right to left "<" left to right ">"
            p = p+1;
            if (p==strainx)
                break;
            end
        end
        ptemp = p;
        if(notchpos(1)>ptpos1(p,1))
            ctpos(i,2) = notchpos(1);
            ctpos(i,3) = notchpos(2);
        else
            ctpos(i,2) = ptpos1(p,1);
            ctpos(i,3) = ptpos1(p,2);
        end
    else
        ctpos(i,2) = notchpos(1);
        ctpos(i,3) = notchpos(2);
    end
end
fr = 4.34e-6; % frame rate in seconds
[f,e] = size(ctpos); % f = no of frames

crackvel = zeros(f,1);
% crack velocity calculation from CT position and frame rate
for i=2:f;
    crackvel(i,1)=sqrt((ctpos(i,2)-ctpos(i-1,2))^2+(ctpos(i,3)-ctpos(i-1,3))^2)*10^-3/fr;
end
```

APPENDIX C

MATLAB CODE FOR DYNAMIC STRESS INTENSITY ANALYSIS

```
% Run importmultipletext_cracksection_CTpos.m first with crack section
% Open the folder with 3D data of the selected region in txt format and then run this file
% All SI units

    d = dir('*.txt');
    nfiles = length(d);
    data = [];
    for k = 1:nfiles
        data = [data; importdata(d(k).name,' ',14)]; % 14 lines of header
        dispy(:,k) = data(k,1).data(:,10); % 10th column is the column for y displacements hence data(:,9)
    end
    % store X Y coordinates of points in ptpos
    ptpos(:,1) = data(1,1).data(:,3);
    ptpos(:,2) = data(1,1).data(:,4);


Cd = 717; % longitudinal velocity m/s
Cs = 440; % Transverse velocity m/s
v = 0.19; % Poisson's ratio
E = 2.50e+09; % Young's modulus Pa
G = E/(2*(1+v)); % Shear modulus Pa
rho = 5404; % density in kg/m3

% ctpos = crack tip position - first column image no., second column crack
% tip position X, third column crack tip position Y.

% ptpos = point position matrix first column X coordinate, second column Y
% coordinate

% dispy = Y displacement of all points, no. of rows = no. of points = n and
% no. of columns = no. of frames = f;

[n,m] = size(ptpos); % n = no of points

fr = 4.34e-6; % frame rate in seconds

[f,e] = size(ctpos); % f = no of frames

crackvel = zeros(f,1);
% crack velocity calculation from CT position and frame rate
for i=2:f;
    crackvel(i,1)=sqrt((ctpos(i,2)-ctpos(i-1,2))^2+(ctpos(i,3)-ctpos(i-1,3))^2)*10^-3/fr;
end


ad = zeros(f,1); % alpha-d
for i=1:f;
    ad(i,1)=sqrt(1-(crackvel(i,1)/Cd)^2);
end
as = zeros(f,1); % alpha-s
for i=1:f;
    as(i,1)=sqrt(1-(crackvel(i,1)/Cs)^2);
end
D = zeros(f,1); % D
for i=1:f;
```

```
    D(i,1)=4*ad(i,1)*as(i,1)-(1+as(i,1)^2)^2;
end

r = zeros(n,f); % r for n points and f frames from crack tip
for i = 1:f
    for j = 1:n
        r(j,i) = sqrt((ptpos(j,1)-ctpos(i,2))^2+(ptpos(j,2)-ctpos(i,3))^2)*10^-3;
    end
end
theta = zeros(n,f); % theta for n points and f frames from crack tip
for i = 1:f
    for j = 1:n
        theta(j,i) = atan((ptpos(j,2)-ctpos(i,3))/(ptpos(j,1)-ctpos(i,2)));
        if (ptpos(j,1)-ctpos(i,2))<0
            if (ptpos(j,2)-ctpos(1,3))<0
                theta(j,i) = theta(j,i)-pi;
            else
                theta(j,i) = theta(j,i)+pi;
            end
        end
    end
end


thetad = zeros(n,f); % theta-d for n points and f frames from crack tip
for i = 1:f
    for j = 1:n
        thetad(j,i) = atan(ad(i,1)*tan(theta(j,i)));
        if (ptpos(j,1)-ctpos(i,2))<0
            if (ptpos(j,2)-ctpos(1,3))<0
                thetad(j,i) = thetad(j,i)-pi;
            else
                thetad(j,i) = thetad(j,i)+pi;
            end
        end
    end
end
thetas = zeros(n,f); % theta-s for n points and f frames from crack tip
for i = 1:f
    for j = 1:n
        thetas(j,i) = atan(as(i,1)*tan(theta(j,i)));
        if (ptpos(j,1)-ctpos(i,2))<0
            if (ptpos(j,2)-ctpos(1,3))<0
                thetas(j,i) = thetas(j,i)-pi;
            else
                thetas(j,i) = thetas(j,i)+pi;
            end
        end
    end
end


Yd = zeros(n,f); % Gamma-d for n points and f frames from crack tip
for i = 1:f
    for j = 1:n
```

```
        Yd(j,i) = sqrt(1-(crackvel(i,1)*sin(theta(j,i))/Cd)^2);
    end
end
Ys = zeros(n,f); % Gamma-s for n points and f frames from crack tip
for i = 1:f
    for j = 1:n
        Ys(j,i) = sqrt(1-(crackvel(i,1)*sin(theta(j,i))/Cs)^2);
    end
end

dispydot = zeros(n,f);
for i = 2:f
    for j = 1:n
        dispydot(j,i) = (dispy(j,i)-dispy(j,i-1))*10^-3/fr;
    end
end

Kidyn = zeros(n,f);
for i = 2:f
    for j = 1:n
        if(ptpos(j,1)<0.36)
        Kidyn(j,i) = -dispydot(j,i)*G*D(i,1)*sqrt(2*pi*r(j,i))...
            /(crackvel(i,1)*ad(i,1))/((1+as(i,1)^2)*sin(0.5*thetad(j,i))...
            /sqrt(Yd(j,i))-2*sin(0.5*thetas(j,i))/sqrt(Ys(j,i)));
        end
    end
end

Kidyn_ave = zeros(f,1);
Kidyn_stdev = zeros(f,1);
for i = 2:f
    Kidyn_ave(i,1)=mean(Kidyn(:,i));
    Kidyn_stdev(i,1)=std(Kidyn(:,i));
end
```

APPENDIX D

MATLAB CODE FOR STATIC STRESS INTENSITY ANALYSIS

```
% Open the directory with all txt files from ARAMIS with 3D data

% All SI units

d = dir('*.txt');
nfiles = length(d);
data = [];
for k = 1:nfiles
   data = [data; importdata(d(k).name,' ',14)]; % 14 lines of header
   dispy(:,k) = data(k,1).data(:,10); % 10th column is the column for y displacements hence data(:,9)
end
% store X Y coordinates of points in ptpos
ptpos(:,1) = data(1,1).data(:,3);
ptpos(:,2) = data(1,1).data(:,4);

Cd = 717; % longitudinal velocity m/s
Cs = 440; % Transverse velocity m/s
v = 0.19; % Poisson's ratio
E = 2.50e+09; % Young's modulus Pa
G = E/(2*(1+v)); % Shear modulus Pa
rho = 5404; % density in kg/m3
kappa = (3-v)/(1+v); % for plane stress, plane strain change to (3-4v)

% ctpos = crack tip position - first column image no., second column crack
% tip position X, third column crack tip position Y.

% ptpos = point position matrix first column X coordinate, second column Y
% coordinate

% dispy = Y displacement of all points, no. of rows = no. of points = n and
% no. of columns = no. of frames = f;

[n,m] = size(ptpos); % n = no of points
fr = 4.34e-6; % frame rate in seconds


[f,e] = size(ctpos); % f = no of frames

crackvel = zeros(f,1);
% crack velocity calculation from CT position and frame rate
for i=2:f;
   crackvel(i,1)=sqrt((ctpos(i,2)-ctpos(i-1,2))^2+(ctpos(i,3)-ctpos(i-1,3))^2)*10^-3/fr;
end


r = zeros(n,f); % r (in m - 10^-3 factor) for n points and f frames from crack tip
for i = 1:f
   for j = 1:n
      r(j,i) = sqrt((ptpos(j,1)-ctpos(i,2))^2+(ptpos(j,2)-ctpos(i,3))^2)*10^-3;
   end
end

theta = zeros(n,f); % theta for n points and f frames from crack tip
for i = 1:f
   for j = 1:n
```

```
        theta(j,i) = atan((ptpos(j,2)-ctpos(i,3))/(ptpos(j,1)-ctpos(1,2)));
        if (ptpos(j,1)-ctpos(i,2))<0
            if (ptpos(j,2)-ctpos(i,3))<0
                theta(j,i) = theta(j,i)-pi;
            else
                theta(j,i) = theta(j,i)+pi;
            end
        end
    end
end


Kistat = zeros(n,f);
for i = 2:f
    for j = 1:n
        Kistat(j,i) = dispy(j,i)*1e-3*2*G/sqrt(r(j,i)/(2*pi))...
            /(sin(theta(j,i)/2)*(kappa+1-2*(cos(theta(j,i)/2))^2));
    end
end

Kistat_ave = zeros(f,1);
Kistat_stdev = zeros(f,1);
for i = 2:f
    Kistat_ave(i,1)=mean(Kistat(:,i));
    Kistat_stdev(i,1)=std(Kistat(:,i));
end
```

APPENDIX E

COPPER / EPOXY ADHESION

The use of epoxy resins in microelectronic packaging is increasing because of requirements pertaining to the need for low dielectric constant, high thermal stability, good mechanical properties, and processing ability [1 – 5]. They are used as photo-resists, radiation masks, dielectrics and inter-level insulators. In most of these applications, the mechanical properties of the epoxy resins and its adhesion to other components of the system are of utmost importance in order to ensure performance and reliability of the device. Hence the adhesion between epoxy resins and metal has been a topic of research for long time.

The parameter of most practical significance with respect to adhesion is interfacial fracture toughness, the energy required per unit area to separate an interface. Various protocols have been used to access adhesion including the pull test [6], double cantilever beam (DCB) [7], four-point bending [8], double cantilever drilled compression (DCDC) [9], peel testing [10], button shear test [11], laser spallation [12], and the scratch test [13]. Although some measure of interface strength can be measured by all these methods, the measurement of fracture toughness is a challenge. Peel tests require tedious analysis for fracture toughness determination, whereas, the button shear test, pull test and laser spallation yield qualitative results. Only the DCB test, four-point bend test and the DCDC test provide easy measurement of the fracture toughness. Different mode mixity can be achieved in DCB test by varying thickness of the layers [14] whereas in four point bend testing there is an approximately equal mode I and mode II component [8]. Volinsky et al. [15], Chen et al. [16] have extensively reviewed various tests for adhesion measurement. Volinsky et al. [15], in their review paper, have shown the effect of different intrinsic (modulus, yield strength, the thermodynamic work of adhesion and length scales in the samples) and extrinsic (residual stress, extent of delamination, film thickness and temperature) variables on the adhesion between thin films and substrates.

Kim et al. [17] studied effect of surface roughness on the interfacial fracture toughness for steel and a carbon fiber reinforced polymer in different mode mixities. They used DCB sample for mode I, edge notched flexure sample for mode II and single leg bend sample for mixed mode fracture toughness measurement. They showed the effect of surface patterning / mechanical interlocking on adhesive strength of the interface. Contact angle measurements were used to access a thermodynamic work of adhesion for the epoxy/steel interface as 88.3 mJ/m^2 whereas the measured interfacial fracture

toughness was 210 J/m^2. They have claimed that the adhesion strength of the interface increases with increase in the surface roughness only when the mechanical interlock results in the transition of failure from adhesive to cohesive. Kook and Dauskardt [18] used the DCB sample to study effect of moisture on crack growth rate as a function of applied strain energy release rate for Cu/Ni/Silica filled epoxy polymer/Ni/Cu sample. The failure occurred between the epoxy polymer and an interaction layer that formed during the curing process between the epoxy and NiO layer. It was found that the crack growth rate in region II (plateau region) was directly proportional to the relative humidity in the air. Ge et al. [4] used pull test to measure strength of electrolessly-deposited copper/photosensitive epoxy interface. The measured strength was in the range 5.3-7.0 MPa for different conditions such as surface roughness, epoxy swelling time etc. Yun et al. [19] studied effect of copper oxide on the copper/epoxy (Diglycidyl ether of bisphenol-A) interface adhesion using peel and blister test. They have shown that for black and red oxides on the surface, the interfacial fracture toughness can be improved to 0.4 and 1.1 kJ/m^2 respectively.

The double cleavage drilled compression (DCDC) specimen was developed by Janssen [20, 9] in order to obtain crack length independent fracture toughness measurements of monolithic brittle materials. Later, He et al. [21] showed that it can also be used to measure the fracture toughness of an interface between two different materials. One of the major advantages of the DCDC specimen over the DCB or the four point bend specimen is stable crack growth at the interface. The stress intensity at the crack tip for the DCDC specimen decreases as the crack propagates at constant load unlike the DCB or the four-point bend test.

In the DCDC sample geometry, a thin sheet of one material is sandwiched between thick layers of the other material as shown in the Figure E1. A hole is then drilled at the center parallel to the sandwiched sheet structure. The sample is then loaded in compression and interfacial delamination is achieved. At any point, given stress (σ), sample geometry and Young's modulus of the bulk material (E) and crack length (a), the fracture toughness ($\mathcal{G}$) can be calculated according to:

$$\mathcal{G} = \frac{\sigma^2 \pi R}{\bar{E}} \left[\frac{w}{R} + \left(0.235\frac{w}{R} - 0.259\right)\frac{a}{R}\right]^{-2} \text{ for } 6 \leq \text{a/R} \leq 15 \qquad 1$$

This Equation was derived by He et al. [21] using finite element analysis supported by experimental measurements. Here R is radius of the hole and w is the half width of the sample as shown in the Figure E1.

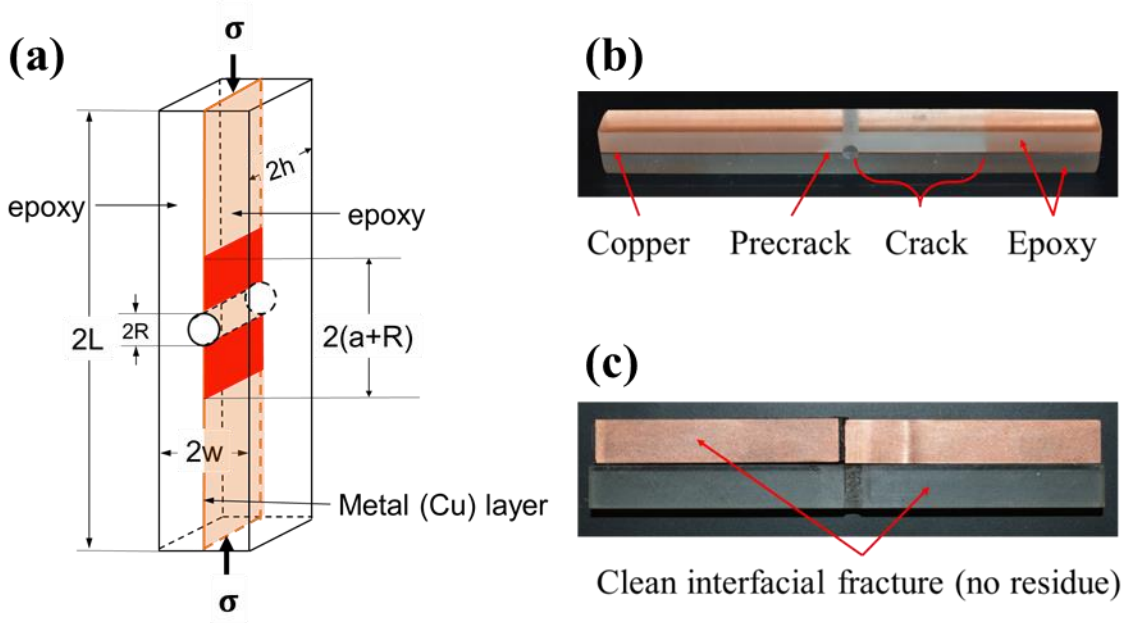

Figure E1: (a) Schematic illustration of the DCDC specimen geometry. The dimensional requirements for the DCDC sample are L/w = 10, w/h = 1.2 and w/R = 2 – 4. (b) An epoxy/Cu/epoxy DCDC sample. The actual dimensions of the sample were 2h = 6.5 mm, 2w = 5.4 mm and 2L = 65 mm. The hole in the center had a diameter, 2R = 2 mm. (c) All samples had clean interfacial fracture with no residue of the other material on either the copper or the epoxy fracture surfaces.

Another advantage of the DCDC sample test is preferential crack growth at the interface. The tendency of the crack to move or kink away from the interface is characterized by the loading phase angle (Ψ), which is defined as [22]:

$$\Psi = \tan^{-1}\left(\frac{K_{II}}{K_I}\right) \qquad 2$$

Here K_I and K_{II} are mode I and mode II stress intensity factors. For a mixed mode crack i.e. $\Psi > 0$, the crack stays at the interface even if the adjacent materials have lower fracture toughness than the interface. The mode mixity can be obtained by drilling the hole off center from the center plane [21]. For this study, the hole is configured in the center of the sample to achieve near mode I loading ($\Psi \approx 0$).

Turner et al. [23] used DCDC samples to measure the interfacial fracture toughness of sapphire/gold and glass/resin interfaces. For both systems, the fracture energy remained nominally constant with increase in the crack length with typical variation of +/- 25% of the mean value. They also measured fracture toughness of sapphire/Pt interface using DCDC sample for which they found that toughness at the crack initiation was ~ 52 J/m^2 and the toughness at the crack arrest was ~30 J/m^2. These values are more than the fracture toughness of the sapphire (~10 – 20 J/m^2). This supports the theory that there is preferential interfacial fracture in DCDC specimen even if the interfacial fracture toughness exceeds that of the bulk materials [21]. Gaudette et al. [24] studied the effect of sulfur (S) on the fracture resistance of the interface between γ-Ni(Cr) and α-Al_2O_3 using DCDC samples. They showed that liquid phase bonding which causes S segregation to the interface results in toughness values of 2 – 7 J/m^2. However interfaces produced by solid state diffusion bonding where S segregation is absent, results in toughness values ~ 300 J/m^2 where failure takes place in the sapphire.

Kiely and Bonnell [25] measured Ni/sapphire interface fracture strength as a function of embrittlement due to sulfur segregation using DCDC specimen. The sulfur segregation was controlled by controlling moisture during testing. Their interfacial fracture toughness values ranged from 8.5 to 34 J/m^2 and correlated with S segregation, oxide density, and test environment. The fracture energy increased with decreasing S segregation along the interface. The tests conducted in oil showed higher fracture toughness than those conducted in air.

In this study, DCDC samples are used to measure the interfacial fracture toughness of copper/epoxy interfaces. To the best of our knowledge this is the first study performed on metal/epoxy interfaces using the DCDC sample geometry.

200 μm thick copper sheets (supplied by McMaster-Carr) were cleaned using Nitric acid (pH = 1) and rinsed with deionized water several times. The Cu-sheets were subsequently heated in air at ~ 90^oC for 10 minutes to remove the moisture present on the surface. A two part low viscosity epoxy (EpoThin™, Buehler) was used. This has curing time of about 9 hours at room temperature. The cured epoxy is transparent and has ~ 78 shore D hardness. A PTFE mold was used to prepare epoxy/Cu/epoxy sandwich composites. A thin layer of Buehler Release Agent was put on copper sheet prior to bonding to epoxy in order to establish a pre-crack. Once the epoxy was cured the samples were cut using a saw to

rough dimensions and then milled to get the final dimensions. A special fixture was used to hold the sample to prevent any interfacial delamination during the machining. The final dimensions obtained were 6.5 mm x 5.4 mm x 65 mm as shown in the Figure E1. Then a 2 mm diameter hole was drilled in the center of the 6.5 mm x 65 mm face through the sample. Since the epoxy was transparent, any de-bonding at the interface can be easily observed (Figure E1(b)). All samples tested were free of any de-bonding prior to testing. A self-aligning compression fixture was used for the testing. During the compression testing of the DCDC samples, a small piece of parafilm was kept on the top and bottom of the sample in order to maintain uniform loading.

A MTS Sintech 5/G electromechanical machine along with self-aligning compression fixtures was used for the compression testing. The tests were done at a crosshead speed of 100 micrometer/seconds under displacement control in increasing steps of 25 N. Crack lengths were measured after each 25 N load increment. The crack length value along with the corresponding load value was used to calculate interfacial fracture toughness of the epoxy/Cu/epoxy samples system using Equation 1. Since there are 2 copper/epoxy interfaces and a pre-crack was established at each interface, there are 4 potential locations (left and right hand side of copper, above and below the hole) for crack growth. Out of the four locations, only two pre-cracks were generally observed to grow and in most cases these were on diagonally opposite ends (e.g. top left and bottom right with respect to the hole). This confirms uniform loading conditions and symmetry of the sample. Young's modulus of the sample was measured to be 1.75 GPa and assuming Poisson's ratio to be 0.35 From the Equation 1, $\mathcal{G}$ values depend weakly on the value of the crack length. In some tests the values of the crack lengths on either side of the hole were different and in these cases the average of the two values was used.

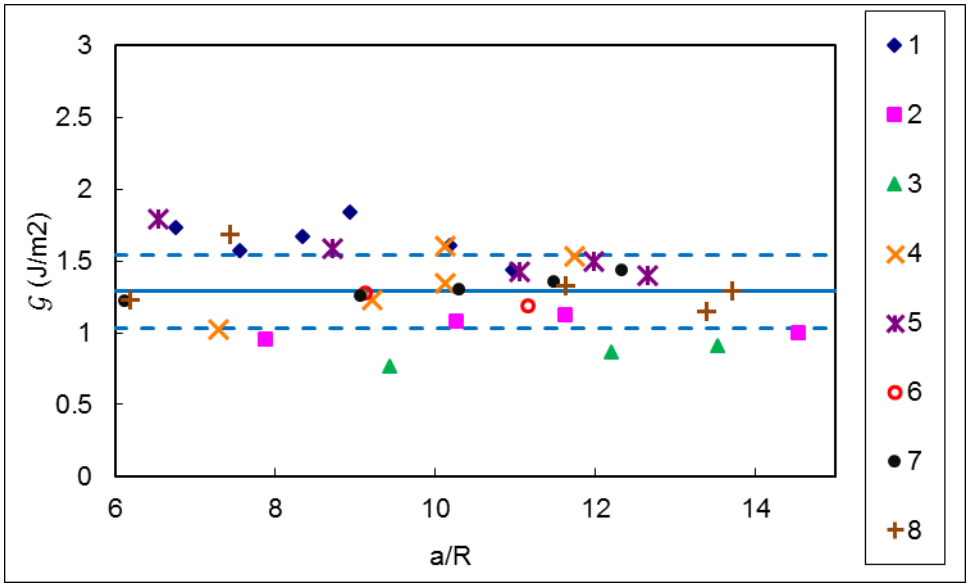

Figure E2: Interfacial fracture toughness for the epoxy resin/metal interface as a function of crack length for 8 different samples – represented in the figure by different colored lines. The solid line represents average value of $\mathcal{G}$ (= 1.29 J/m^2) whereas the dotted lines represent mean value ± standard deviation (1.29 ± 0.25 J/m^2). The crack lengths were measured using a caliper with 0.001" (25 um) accuracy. The error bars are not visible for the given scale.

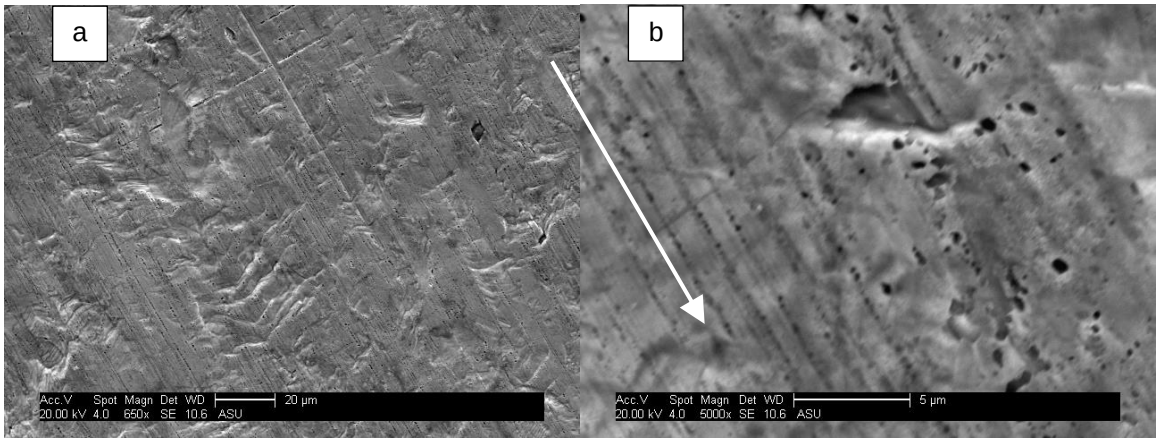

Figure E3: SEM of the fracture surface shows (a) surface roughness (b) the holes on the fracture surface indicate mechanical interlocking between the epoxy and copper. The arrow indicates fracture direction.

Figure E2 shows the interfacial fracture toughness vs crack length results for all the tests. The interfacial fracture toughness value was observed to be independent of crack length. Average value of the interfacial fracture toughness was ~ 1.29 J/m^2 with ~ 0.25 J/m^2 standard deviation. The spread in the data is likely to be connected to the defects at the interface. Figure E3 shows SEM image of the fractured copper surface. The surface roughness on the sample surface increases total contact area increasing the fracture toughness for the interface. Also the pits on the sample surface may allow mechanical

interlocking between the epoxy and copper surface. With known defect population at the interface, the variation in the fracture toughness as the crack progresses can be predicted. Use of in-situ crack length measurement system such as Krak-gage® or optical methods can facilitate the experiments and improve the accuracy with continuous data.

Here the copper used to prepare the sample was 200 um thick. Using different thickness of the sandwiched material that is nominally ductile, can affect the measured fracture toughness value during any test that involves such sandwich sample configuration. Turner and Evans [26] measured interfacial fracture toughness for Au/sapphire interface with 10 um and 25 um Au layers. The de-bond energies were 40 J/m^2 and 60 J/m^2 for 10 um and 25 um thick Au layers respectively. As the copper thickness increases, the amount of plastic energy dissipated in the copper would increase. This in turn, would increase load value corresponding to a specific crack length, increasing the measured fracture toughness value. At the same time, using very thin sandwiched material can cause rupture of the sandwiched material [27]. Hence different thickness of the ductile sandwiched material can be used to measure fracture toughness as a function of the thickness of the sandwiched material and the plot can be extrapolated to obtain fracture toughness value for the interface for near zero thickness of the sandwiched material. Lardner et al. [28] have also reported effect of adhesive layer thickness (t) on the G value. They claim that as thickness of the sandwiched material increases, measured value of the fracture toughness G_s decreases from the actual value G_0. However they don't give any explanation why this would be happening. This contradicts our prediction and experimental data shown by Turner and Evans [26].

Here we have used the DCDC specimen for the first time to measure interfacial fracture toughness of metal/epoxy interface – an important interface in the semiconductor industry. These samples are easy to prepare and can serve as another validation technique for other interfacial fracture toughness measurement methods like DCB, four-point bend test, with added advantages of stable crack growth and ease of achieving desired mode mixity.

APPENDIX E REFERENCES

[1] C. H. Lin, J. C. Chiang, C. S. Wang, "Low dielectric thermoset. I. Synthesis and properties of novel 2,6-dimethyl phenol-dicyclopentadiene epoxy," *Journal of Applied Polymer Science*, vol. 88, no. 11, pp. 2607-2613, 2003.

[2] Z. Q. Zhang, E. Beatty, C. P. Wong, "Study on the Curing Process and the Gelation of Epoxy/Anhydride System for No-Flow Underfill for Flip-Chip Applications," *Macromolecular Materials and Engineering*, vol. 288, no. 4, pp. 365-371, 2003.

[3] S. J. Park, F. L. Jin, J. H. Park, K. S. Kim, "Synthesis of a novel siloxane-containing diamine for increasing flexibility of epoxy resins," *Materials Science and Engineering: A*, vol. 399, no. 1, pp. 377-381, 2005.

[4] J. Ge, R. Tuominen, J. K. Kivilahti, "Adhesion of electrolessly-deposited copper to photosensitive epoxy," *Journal of Adhesion Science and Technology*, vol. 15, no. 10, pp. 1133-1143, 2001.

[5] Z. Ge, Z. Tao, J. Liu, L. Fan, S. Yang, "Synthesis and characterization of novel trifunctional fluorine containing epoxy resins based on 1, 1, 1-tris (2, 3-epoxypropoxyphenyl)-2, 2, 2-trifluoroethane," *Polymer journal*, vol. 39, no. 11, pp. 1135-1142, 2007.

[6] K. Kendall, "The adhesion and surface energy of elastic solids," *Journal of Physics D: Applied Physics*, vol. 4, no. 8, p. 1186, 1971.

[7] J. M. Whitney, C. E. Browning, W. Hoogsteden, "A double cantilever beam test for characterizing mode I delamination of composite materials," *Journal of Reinforced Plastics and Composites*, vol. 1, no. 4, pp. 297-313, 1982.

[8] P. G. Charalambides, J. Lund, A. G. Evans, R. M. McMeeking, "A test specimen for determining the fracture resistance of bimaterial interfaces," *Journal of applied mechanics*, vol. 56, no. 1, pp. 77-82, 1989.

[9] C. Janssen, "Specimen for fracture mechanics studies on glass," *Revue de Physique Appliquée*, vol. 12, no. 5, pp. 803-803, 1977.

[10] L. F. Kawashita, D. R. Moore, J. G. Williams, "Protocols for the measurement of adhesive fracture toughness by peel tests," *The Journal of Adhesion*, vol. 82, no. 10, pp. 973-995, 2006.

[11] W. K. Szeto, M. Y. Xie, J. K. Kim, M. M. F. Yuen, P. Tong, S. Yi, "Interface failure criterion of button shear test as a means of interface adhesion measurement in plastic packages," in *International symposium on electronic materials & packaging*, Hong Kong, 2000.

[12] V. Gupta, A. S. Argon, D. M. Parks, J. A. Cornie, "Measurement of interface strength by a laser spallation technique," *Journal of the Mechanics and Physics of Solids*, vol. 40, no. 1, pp. 141-180, 1992.

[13] P. A. Steinmann, Y. Tardy, H. E. Hintermann, "Adhesion testing by the scratch test method: the influence of intrinsic and extrinsic parameters on the critical load," *Thin Solid Films*, vol. 154, no. 1, pp. 333-349, 1987.

[14] F. Xiao, C. Y. Hui, E. J. Kramer, "Analysis of a mixed mode fracture specimen: the asymmetric double cantilever beam," *Journal of Materials Science*, vol. 28, no. 20, pp. 5620-5629, 1993.

[15] A. A. Volinsky, N.R. Moody, W.W. Gerberich, “Interfacial toughness measurements for thin films on substrates”, *Acta Materialia,* vol. 50, pp. 441-466, 2002.

[16] Z. Chen, K. Zhou, X. Lu, Y. C. Lam, “A review on the mechanical methods for evaluating coating adhesion”, *Acta Mechanica,* vol. 225, no. 2, pp. 431-452, 2014.

[17] W. S. Kim, I. H. Yun, J. J. Lee, H. T. Jung, "Evaluation of mechanical interlock effect on adhesion strength of polymer–metal interfaces using micro-patterned surface topography," *International journal of adhesion and adhesives*, vol. 30, no. 6, pp. 408-417, 2010.

[18] S. Y. Kook, R. H. Dauskardt, "Moisture-assisted subcritical debonding of a polymer/metal interface," *Journal of Applied Physics*, vol. 91, no. 3, pp. 1293-1303, 2002.

[19] H. K. Yun, K. Cho, J. H. An, C. E. Park, "Adhesion improvement of copper/epoxy joints," *Journal of Materials Science*, vol. 27, no. 21, pp. 5811-5817, 1992.

[20] C. Janssen, "Specimen For Fracture Mechanics Studies on Glass," in Proceedings of 10th International Congress On Glass, Kyoto, Japan, 1974.

[21] M. Y. He, M. R. Turner, A. G. Evans, "Analysis of the double cleavage drilled compression specimen for interface fracture energy measurements over a range of mode mixities," *Acta metallurgica et materialia,* vol. 43, no. 9, pp. 3453-3458, 1995.

[22] J. W. Hutchinson, Z. Suo, "Mixed Mode Cracking in Layered Materials," *Advances in applied mechanics*, vol. 29, pp. 63-191, 1992.

[23] M. R. Turner, B. J. Dalgleish, M. Y. He, A. G. Evans, "A fracture resistance measurement method for bimaterial interfaces having large debond energy," *Acta metallurgica et materialia*, vol. 43, no. 9, pp. 3459-3465, 1995.

[24] F. G. Gaudette, S. Suresh, A. G. Evans, "Effects of sulfur on the fatigue and fracture resistance of interfaces between γ-Ni (Cr) and α-Al2O3," *Metallurgical and Materials Transactions A* , vol. 31, no. 8, pp. 1977-1983, 2000.

[25] J. D. Kiely, D. A. Bonnell, "Metal ceramic interface toughness I: Plasticity on multiple length scales," *Journal of materials research*, vol. 13, no. 10, pp. 2871-2880, 1998.

[26] M. R. Turner, A. G. Evans, "An experimental study of the mechanisms of crack extension along an oxide/metal interface," *Acta materialia*, vol. 44, no. 3, pp. 863-871, 1996.

[27] M. Hasegawa, S. J. Zhu, Y. Kagawa, A. G. Evans, "Effect of metal layer thickness on the decohesion of high purity copper–sapphire interfaces," *Acta materialia*, vol. 51, no. 17, pp. 5113-5121, 2003.

[28] T. J. Lardner, S. Chakravarthy, J. D. Quinn, J. E. Ritter, "Further analysis of the DCDC specimen with an offset hole," *International journal of fracture*, vol. 109, no. 2, pp. 227-237, 2001.